



UNIVERSITÀ  
DEGLI STUDI  
DI PADOVA

Head Office: Università degli Studi di Padova

Department of Industrial Engineering

Ph.D. COURSE IN: Industrial Engineering

CURRICULUM: Materials Engineering

SERIES: 35<sup>th</sup>

## **Hybrid and multi-material additive manufacturing technologies for ceramics**

**Coordinator:** Prof. Paolo Sgarbossa

**Supervisor:** Prof. Giorgia Franchin

**Co-Supervisor:** Prof. Paolo Colombo

**Ph.D. Student :** Anna De Marzi



# Acknowledgments

Above all, I am addicted to changes: evolution of ideas, knowledge and points of views have been the main driving forces of my life. This thriving made me lost inside and out myself, endlessly making me feel like I am on the run, alone. Probably more now, as I am about to deliver my Ph.D. thesis, I have some time to slow down, look back and see what a rollercoaster this journey has been. The truth is that, while I still have to still figure out a lot of things, I know that where I arrived and what I have accomplished would not been the same without the people that accompany me in these years and made it feel like I was in the safest and most comfort places to be.

First and foremost, I thank my supervisor, Prof. Giorgia Franchin: you have definitely been the mentor I did not deserve but the one that I needed. It is safe to say that we don't resemble the traditional supervisor/student couple: all our misunderstandings and infinite meetings made us clash as much as it made us laugh standing up on lab desks and having revolutionary ideas after 7pm. Above that, thank you for your patience and hints during these years together; your – somehow – unconditioned positivity and creativity have shaped and changed the way I work and look towards research.

With her I thank Prof. Paolo Colombo, my co-supervisor. You have been one of the rare certainties in my academic life: as for my Bachelor and Master theses, thank for your endless support. Your experience and knowledge have been a true inspiration for me; I feel grateful for all of your advices given in the hallway, the pure joy when seeing crack-free samples and, most of all, the kindness you have shown towards me.

Furthermore, I would like to thank the people that contributed to the work presented here. Sarah Diener (Kyocera Fineceramics GmbH, Selb), for the help and support for the silicon nitride research work, the furniture and modification of the powder, the thermal treatments on the samples and their mechanical testing. Giovanna Zaramella (University of Padova), for the data collection regarding the multicomponent glass work; Michele Vibrante (University of Padova), for the development of the GUI and assistance on the optimization of the robot-assisted hybrid UV-DIW. Dr. Andrea Zocca, my supervisor during my period abroad: thank you for welcoming me at the Division 5.4 of Bundesanstalt für Materialforschung und -prüfung (BAM) in Berlin;

for the rheological measurements of the graphite and tungsten inks and the  $\mu$ -CT measurements. More than that, thank you for sharing your skills, competences and insights on the LSD technique, which have been a precious support for my experimental work.

Next, I would like to thank all my colleagues at the CerAMglass research group and at the labs of DII in Padova. Particularly, thanks to Lorenzo Lattanzi, Margherita Sardo and Alice Zanini, my most recent office mates: you had to live with me in one of the most challenging periods of my life. Your help, laughs and gossips cherished and calmed me more than what could have been possible. Thanks to Renata Botti, Useche Inchauspe and Alessandro Longato for your frankness – your strength and charisma have been the angel/devil combination that fueled most of my work. Thanks to Elena Colusso, Alessandro Gandin, and Filippo Gobbin: you were, are and will be the models I have been (and will) look up to during and after my Ph.D. – thank you for your friendship and support, and for have been the perfect mix between seriousness and lightness. A special thanks goes to Giulio Giometti for a bit of all the reasons I have listed above: a big chunk of the research work presented here would have not been the same without your support, methodology and humor.

With them, thanks also to Padova, the city that adopted me, and to the other people that I met here. Especially, thanks to Clelia, my favorite *frega* from Umbria. Thanks for your caring and kindness: your chaotic enthusiasm and genuine openness to life have definitely left a mark on my solitary soul. Berlin, thanks to you too: your extremes and dualisms have shaken and toughened me as well as made me feel free to just be. Special thanks go to Lilou, your naturalness and humor have lightened up my days at BAM – and to Matteo: your hospitality and jokes were essential for soundly ride out the Berlin winter and making it feels a bit like home. To all my friends back in Arzignano: thanks for your company, calmness and support; you have been a true anchor throughout – at this time – half of my life.

At last, I thank my family. Francesca, our complicity is a treasure that I will never let go; thanks for your creativity, sincerity and caring. To my parents: you are the principle of everything I am today. Mami, thanks for transmitting me your sense of organization and independence which fueled my stubbornness and curiosity to the world. Papo, your work dedication and attitude as well as your humor, endless jokes, and laughs, kept alive my naiveness, my feet on the ground and my mind focused. Above all, thanks to all of you for your unconditioned love.



# Abstract

The parallel development and optimization of industrial manufacturing techniques have set new standards and increased the demand for highly performing, complex and cost-effective components. Novel techniques like those of additive manufacturing have lost their rapid prototyping reputation and have been more and more employed for the fabrication of functional components made of high-end materials. Nonetheless, the specific printing process requirements and their layer-by-layer construction approach have been limiting their unique advantages in terms of design freedom and especially of the achievable optical, mechanical and electrical properties of the final component.

The aim of this research project has been the development of hybrid and multi-material additive manufacturing technologies for the fabrication of ceramic and ceramic-metal components. Specifically, three-dimensional parts with complex geometries have been fabricated using two different hybrid techniques, a UV-assisted Direct Ink Writing and a Layerwise Slurry Deposition coupled with Direct Ink Writing. The fundamental steps in the research project have regarded the development and optimization of the hybrid processes and feedstocks.

Silica-based and silicon nitride-based inks were prepared and used to produce support-less structures, ultimately verifying the UV-DIW system ability to print ceramic particles that absorb the incident light. Particle surface properties and liquid-particle interaction forces were found to be the most critical parameters to control the ink particle loading and flow behavior. Adequate density and fracture strength were achieved for lattice-like structures of silicon nitride. Transparent silica glass components were obtained thanks to the optimization of the heating schedule and the introduction of a silicon alkoxide.

The development of the hybrid technique evidenced the limitations induced by the 3-axis setup. Hence, the UV-DIW process was coupled with a 6-axis robotic arm: layer-less lattices were fabricated thanks to the use of a custom graphical user interface and control over the printing head orientation. A highly reactive resin was employed as the ink and loaded with silica particles in order to tailor its rheological properties. A good resemblance between the printed components and the digital model was achieved, while their mechanical properties were superior to the ones of the traditionally additive manufactured octets.

The capabilities of the LSD-DIW approach were instead demonstrated by fabricating proofs-of-concept for micro-reactors and heating elements. An alumina water-based slurry was optimized as the ceramic matrix; hydroxy-methyl cellulose was identified as the best candidate to balance the water evaporation and absorption forces thanks to its gel-like behavior. Tungsten and graphite inks were employed to create electrically conductive paths and hollow channels, respectively.







# Table of Contents

<b>Index of Figures</b> .....	<b>xiii</b>
<b>Index of Tables</b> .....	<b>xxi</b>
<b>1 Introduction</b> .....	<b>24</b>
1.1 Additive manufacturing of ceramics .....	24
1.1.1 Direct Ink Writing .....	26
1.1.2 Digital Light Processing .....	27
1.1.3 Layer-wise Slurry Deposition .....	28
1.2 Hybrid additive manufacturing of ceramics .....	30
1.2.1 UV-assisted Direct Ink Writing .....	32
1.2.2 Additive manufacturing technologies for multi-material components	34
<b>2 Hybrid UV-DIW technology</b> .....	<b>40</b>
2.1 Hybrid setup and printing process .....	41
2.2 Ink design and preparation .....	42
2.3 Silica ink .....	45
2.3.1 Printing and freeform ability .....	51
2.3.2 Heating treatments .....	57
2.3.3 Multicomponent silica-based ink.....	63
2.4 Silicon nitride ink.....	67
2.4.1 Printing and freeform ability .....	74
2.4.2 Lattice structures characterization .....	80
2.5 Hybrid UV-DIW on a robot arm.....	87
2.5.1 Printing and freeform ability .....	91
2.5.2 Fabrication of lattice structures.....	95
2.5.3 Effect of the manufacturing method on the mechanical properties ..	98
Appendix A – Robot calibration for UV-DIW .....	105
<b>3 Multi-material LSD-DIW technology</b> .....	<b>109</b>

3.1	Hybrid setup and printing process .....	112
3.2	Alumina slurry optimization .....	114
3.3	Inks characterization.....	119
3.3.1	Graphite ink .....	120
3.3.2	Tungsten ink .....	122
3.4	Parts fabrication and characterization.....	124
3.5	Heating treatments .....	130
	Appendix B – Grasshopper script for LSD-DIW .....	136
	Appendix C – Alumina water-based compositions .....	141
	<b>Conclusions .....</b>	<b>143</b>
	<b>References .....</b>	<b>148</b>



# Index of Figures

<b>Figure 1.1.</b> Schematic representations of the (a) Direct Ink Writing (DIW) and (b) Digital Light Processing (DLP) techniques. ....	27
<b>Figure 1.2.</b> Schematic representation of the Layer-wise Slurry Deposition technology.....	29
<b>Figure 1.3.</b> Graphical map representation of the subdivision of manufacturing, hybrid and multi-material manufacturing processes .....	31
<b>Figure 1.4.</b> Schematic representation of the UV-assisted Direct Ink Writing technique. ....	33
<b>Figure 1.5.</b> Nanocomposite coil fabrication published by Lebel et al. [65]: (a) virtual image showing the programmed UV-DIW fabrication of the coil; (b) optical microscope image of the actual deposited coil. (c) optical images of self-supporting structures having microporous filaments published by Maeng et al. [67]. ....	34
<b>Figure 1.6.</b> Koopmann et al. [81]: (a) tri-layer sandwich structure featuring a 10-mm base and a height of approximately 7 mm, and (b) SEM image of its cross section with upper and lower steel layers embedding the ceramic layer (dark gray) in the middle. Wang et al. [88]: (c) process chain of ceramic HAM technology for functional LTCC slurry preparation and (f) schematic sketch of the circuit board, sintered substrate and working condition. Raynaud et al. [89]: (e) assembly for the production of bi-material objects combining robocasting and stereolithography processes; (f) micrograph of green parts showing (left to right) uncovered tracks, embedded tracks with vias and armored vias; (g) SEM images of HTCC components showing (left to right) uncovered tracks and embedded track connected to surface by vias. ....	36
<b>Figure 2.1.</b> Hybrid UV-DIW equipment printed in PLA (left) and mounted over the head of a delta printer (right). ....	41
<b>Figure 2.2.</b> Silica-based inks with variable TEGDA/HEMA ratio at fixed silica content. ....	48
<b>Figure 2.3.</b> Silica-based inks with variable silica content at fixed TEGDA/HEMA ratio. ....	49
<b>Figure 2.4.</b> Effect of the amount of fumed silica and TEOS on the viscosity profile of LS, HS and HST inks; the grey area represents the printing range of shear rates. ....	50
<b>Figure 2.5.</b> (left) Curing depth of the HST ink as a function of exposure energy density (logarithmic scale); (right) transmittance spectra of the HST ink.....	52

<b>Figure 2.6.</b> Three intervals thixotropy test (3ITT) on the HST ink with different UV exposure times. ....	53
<b>Figure 2.7.</b> Comparison between the coil (a) digital model, (b) printed (green state). ....	55
<b>Figure 2.8.</b> Comparison between the honeycomb (a) digital model, (b) printed (green state). ....	56
<b>Figure 2.9.</b> TGA profiles of LS, HS and HST samples. ....	57
<b>Figure 2.10.</b> Optimized debinding and sintering schedule. ....	58
<b>Figure 2.11.</b> Effect of the sintering time on the appearance of the sintered sample. ....	59
<b>Figure 2.12.</b> XRD spectra of the HST sample sintered at 1400 °C for 10 min with slow cooling. ....	59
<b>Figure 2.13.</b> From left to right: sintered LS, HST and HS components. ....	60
<b>Figure 2.14.</b> SEM image of the section of a HST sintered filament. ....	61
<b>Figure 2.15.</b> XRD spectrum of the HST sample. ....	61
<b>Figure 2.16.</b> Transmittance spectrum of an HST component. ....	62
<b>Figure 2.17.</b> Sintered coil and honeycomb samples; the scale bar refers to both. ....	62
<b>Figure 2.18.</b> Ce ink, different sintering temperatures and holding times. ....	64
<b>Figure 2.19.</b> Sintered cuboid at 1400 °C for 5 min; from left to right Ce-based composition 1 to 4. ....	65
<b>Figure 2.20.</b> Viscosity profile of the Ce-based ink. ....	65
<b>Figure 2.21.</b> Three intervals thixotropy test (3ITT) on the Ce-based ink with (2 s) and without UV exposure times. ....	65
<b>Figure 2.22.</b> Comparison between (a) digital model, (b) printed (green state) and (c) sintered thin wall shape sample. ....	66
<b>Figure 2.23.</b> Emission spectrum of the glass doped with Ce <sup>3+</sup> ions under excitation at 276 nm. ....	67

<b>Figure 2.24.</b> Viscosity profile of the silicon nitride ink with spray drying powders.....	71
<b>Figure 2.25.</b> Fitting of the Bolomey equation over the particles size range analyzed. ....	72
<b>Figure 2.26.</b> (a) effect of the Si <sub>3</sub> N <sub>4</sub> surface modification and particles size distribution optimization on the viscosity profile of the ink; (b) effect of the silicon nitride content on the viscosity profile. ....	73
<b>Figure 2.27.</b> Schematic of the modified hybrid setup with UV diodes (left) and mounted over the delta printer head (right) .....	75
<b>Figure 2.28.</b> Curing depth of the silicon nitride ink as a function of (a) exposure energy density (logarithmic scale) and (b) UV light intensity; 1 s (orange line) and 5 s (purple line). ....	76
<b>Figure 2.29.</b> Three intervals thixotropy test (3ITT) on the Si <sub>3</sub> N <sub>4</sub> -based ink with different UV exposure intensities. ....	77
<b>Figure 2.30.</b> (a) coil structure printed with the silicon nitride-based ink and (b) a cross-section of the extruded and cured filament.....	78
<b>Figure 2.31.</b> Honeycomb structure printed (green state) with the silicon nitride-based ink. ..	78
<b>Figure 2.32.</b> Comparison between the truss-made beam (a) digital model, (b) printed (green state). ....	79
<b>Figure 2.33.</b> Thermogravimetric curve (TGA) and 1 <sup>st</sup> derivative curve of TGA of the silicon nitride ink. ....	80
<b>Figure 2.34.</b> Truss-made beam structure after sintering (up); magnification of the cracks in 3 different points (bottom). ....	81
<b>Figure 2.35.</b> SEM image of the cross-section of a sintered filament, embedded in resin. ....	82
<b>Figure 2.36.</b> XRD profile of sintered silicon nitride sample. ....	83
<b>Figure 2.37.</b> SEM images of the surface of a sintered filament at 15'000 X (left) and 72'500 X (right).....	84
<b>Figure 2.38.</b> Truss-made beam structure: green state (a) and after sintering (b). ....	85
<b>Figure 2.39.</b> Magnification of a partially collapsed truss inside of the beam structure. ....	85

<b>Figure 2.40.</b> (a) lattice beam specimen on 4-point bending test, and (b) Weibull graph from bending test performed on 11 lattice beams samples. ....	87
<b>Figure 2.41.</b> Schematic of the printing head and path direction during the printing of a semi-hexagon shape. ....	88
<b>Figure 2.42.</b> Schematic of the robot hybrid UV-DIW setup. ....	89
<b>Figure 2.43.</b> Flow chart of the part production process using the GUI. ....	90
<b>Figure 2.44.</b> Scheme of the vision system viewed from the top. ....	90
<b>Figure 2.45.</b> Effect of the amount of silica on the (a) viscosity and (b) shear stress profile; (c) curing depth of the ink as a function of exposure energy density (logarithmic scale); (d) comparison of the three intervals thixotropy test (3ITT) on the 10wt% ink. ....	93
<b>Figure 2.46.</b> Video frame of the honeycomb structure being printed with the robot assisted hybrid UV-DIW setup. Note that in the early stages of setup development, no photo-absorber was present in the ink (hence the transparent color of the structure). ....	94
<b>Figure 2.47.</b> Different truss-based components are printed with the hybrid UV-DIW robot-assisted AM technology. Interlocked cube and triangular pyramid (a); dodecahedron cell (b); fullerene cell (c). ....	95
<b>Figure 2.48.</b> Render image of the CAD model of an octet cell. ....	96
<b>Figure 2.49.</b> Production part phases. ....	97
<b>Figure 2.50.</b> Printed octet lattices; (a) via hybrid UV-DIW; (b) via DLP. ....	98
<b>Figure 2.51.</b> Load vs. displacement curves for the octet cells printed with hybrid UV-DIW setup (a) and DLP machine (b). ....	99
<b>Figure 2.52.</b> Comparison of the failure mechanism of octet fabricated using a DLP printer and the hybrid UV-DIW setup by means of video frames and their corresponding moment in the compressive curves. ....	100
<b>Figure 2.53.</b> Close-up of one node of an octet printed with the hybrid UV-DIW technique. ....	101
<b>Figure 2.54.</b> (a) $\mu$ -CT of octets fabricated using the hybrid UV-DIW (a) and DLP (b) techniques with colormap representing their deviation with respect to the CAD model; (b) normalized surface (%) as a function of the absolute deviation. <i>Courtesy of N. Bonato and S. Carmignato, University of Padova.</i> ....	101



<b>Figure 2.55.</b> Render image of the CAD model of the modified octet with additional material in the node zones (a) and load vs. displacement curves for the structures printed via DLP (b).	102
<b>Figure 2.57.</b> (a) truss of a DLP-octet broken during the compression test; (b) magnification and (c) SEM image of the fracture profile.	104
<b>Figure 3.1.</b> Process schematic of the LSD-DIW process.	111
<b>Figure 3.2.</b> Graphical representation of the forces driving the drying phase of the LSD technique.	112
<b>Figure 3.3.</b> Schematic of the hybrid LSD-DIW setup.	113
<b>Figure 3.4.</b> Schematic of the vat blocking system (front view) and its functioning (side view).	114
<b>Figure 3.5.</b> Effect of the amount of PVA on the viscosity profile of alumina slurries.	117
<b>Figure 3.6.</b> Top view of the defects and cracks of dried layer of alumina based slurries with 0.2 wt% (left) and 1 wt% (right) of PVA.	118
<b>Figure 3.7.</b> Viscosity and shear stress profile as a function of shear rate with interpolation by the power law model.	119
<b>Figure 3.8.</b> Top view of a deposited and dried layer of the HEC based slurry.	119
<b>Figure 3.9.</b> $\mu$ -CT of a sintered sample with failed connection of piled channels (to form a single one with dimensions $1.8 \times 0.9 \text{ mm}^2$ (h x w)).	121
<b>Figure 3.10.</b> (a) viscosity and shear stress evolution of the graphite based ink as a function of shear rate with interpolation by the Herschel-Bulkley model; (b) storage and loss moduli as a function of the oscillation stress at 1 Hz.	122
<b>Figure 3.11.</b> (a) viscosity and shear stress evolution of the tungsten-based ink as a function of shear rate with interpolation by the Herschel-Bulkley model; (b) storage and loss moduli as a function of the oscillation stress at 1 Hz.	123
<b>Figure 3.12.</b> Ink width as a function of the printing speed at fixed extruder speed (a; graphite ink) and applied pressure (b; tungsten ink).	124
<b>Figure 3.13.</b> (a) graphical representation of a micro-reactor design and (b) its result after machining. Results of $\mu$ -CT scan of the sintered part containing the micro-reactor geometry: (c) perpendicular and (d) longitudinal section; (f) overall projection of the hollow channel.	125

<b>Figure 3.14.</b> Schematic of the three channels composing the micro-reactor design. ....	126
<b>Figure 3.15.</b> upper inlet (a) after machining, exposing the outlet layer underneath; (b) after filling with the graphite ink. ....	127
<b>Figure 3.16.</b> Z mapping of the drilling tool with respect to the XY plane. ....	128
<b>Figure 3.17.</b> Volumetric view of a micro-reactor geometry with one inlet and one outlet misaligned in the Z direction and two different sections: inlets (a) and outlet (b). ....	129
<b>Figure 3.18.</b> Graphical representation of the heating element design (a), after being machined (b), after being filled with the tungsten paste (c), and after deposition of a fresh layer of alumina slurry. ....	130
<b>Figure 3.19.</b> Relative variation of the cross-sectional area of an alumina sample during heating in a hot stage microscope. ....	131
<b>Figure 3.20.</b> Bulky alumina component fabricated via LSD-DIW: after printing (a) and after sintering (b). ....	131
<b>Figure 3.21.</b> SEM image of the cross-section of an alumina sintered sample. ....	131
<b>Figure 3.22.</b> Thermogravimetric curve (TGA) and 1 <sup>st</sup> derivative curve of TGA of the graphite based ink. ....	132
<b>Figure 3.23.</b> tungsten/alumina part example after printing (left) and after thermal treatment under vacuum (right). ....	133
<b>Figure 3.24.</b> Optical (a) and SEM (b) image of the interface between alumina (dark, upper left) and tungsten (light, bottom right). ....	134
<b>Figure 3.25.</b> Test of the connectivity of the tungsten path after sintering in vacuum atmosphere: the LED is off when the circuit is open (a) and lights up when the circuit is closed (b). ....	134
<b>Figure A 1.</b> Displacement of the nozzle tip with respect to the reference position during the rotation around the three axes of the reference frame: $\alpha$ (a), $\beta$ (b), $\gamma$ (c). Valid robot configurations with the nozzle inclined of +60° (right) and -60° (left) with respect to the vertical axis. The overall valid workspace is the intersection of the two volumes (pink) (d). ....	106
<b>Figure B 1.</b> Examples of .POS and .MBA files. ....	137

**Figure B 2.** Schematic of the Grasshopper algorithm. .... 137

**Figure B 3.** Top view of the LSD-DIW setup highlighting the available printing region. Note that the deposited layer is partially covered by the X axis of the vat containing the alumina slurry..... 138



# Index of Tables

<b>Table 2.1.</b> List of commonly used ceramics, solvents and acrylates with their refractive indexes (at $\lambda=500$ nm).....	43
<b>Table 2.2.</b> HST ink composition.....	51
<b>Table 2.3.</b> Ce-based ink formulations.....	64
<b>Table 2.4.</b> Silicon nitride-based ink formulation using spray drying powders.....	71
<b>Table 2.5.</b> Optimal wt% for each of the three sieving range. ....	73
<b>Table 2.6.</b> Silicon nitride based ink composition using modified and size distribution optimized particles. ....	74
<b>Table 2.7.</b> Density, porosity, mass loss, and shrinkage of sintered silicon nitride components. ....	82
<b>Table 3.1.</b> List of alumina water-based compositions prepared. ....	116
<b>Table C 1.</b> List of alumina water-based compositions prepared referring to the final wt% of reagents.....	141
<b>Table C 2.</b> List of alumina water-based compositions prepared referring to the final vol% of reagents.....	141





# 1 Introduction

Additive manufacturing technologies have the potential to fabricate complex objects in a material-, energy- and ultimately cost-efficient way. Different than traditional subtractive (i.e., machining, cutting) and forming (i.e., casting, molding) techniques, additive manufacturing processes rely on the selective deposition and consolidation of material, reducing material waste and tool usage; on the other hand, both structure complexity and customization degree are increased.

Each additive manufacturing technique has been proven to be best suited for specific ceramic feedstocks, dimensional scales and component designs, thus defining their limitations. In this sense, the development and optimization of hybrid and multi-material manufacturing approaches is set to further increase part performance, complexity and functionality.

Hence, in the present Chapter, a brief description of the additive manufacturing technologies, as well as their advantages and limits in the fabrication of ceramics will be presented. Later, the basic principles of hybrid and multi-material technologies is also given, with particular focus on the ones employed in the research work of this Thesis.

## 1.1 Additive manufacturing of ceramics

Following the definition proposed by the standard ISO/ASTM 52900:2015(E) [1], an additive manufacturing (AM) technology can be described as “the process of joining materials to make parts from 3D model data, usually layer upon layer, as opposed to subtractive manufacturing and formative manufacturing methodologies”. Indeed, these latter techniques represent the most conventional way to shape a material. Specifically, subtractive methods comprehend all controlled machining processes that are able to shape a solid block of material by removing parts of it through grinding, cutting or drilling [2]. On the other hand, formative techniques



include all those processes which are based on the application of a mechanical stress (i.e., compression, tension or shear) able to cause the deformation of the material into the desired shape (i.e., casting, molding) [2]. Thanks to their well-established procedures, subtractive and formative techniques have been widely employed for the shaping of different materials (i.e., polymers, ceramics, metals) with relative low costs and large production volumes [3]. Yet, the fabrication of complex shapes, fine features and/or intricate geometries is restricted by the technologies themselves: tools employed by the subtractive techniques are limited in the allowed movements and tool wear, while a lot of material is being wasted in the process; formative ones requires for the precise optimization of the molds design and their filling [3], [4].

In this sense, the rapid development of AM technologies has opened new ways, allowing not only a fast and cost-efficient structure prototyping, due to their ability to selectively deposit material where it is needed, but especially an increase of the printable structure complexity and customization [5]. Indeed, contrary to subtractive and formative methods, AM technologies are based on the fabrication of the desired object by the layer-wise addition of the selected material without need of molds or tools. While the first ever paper on an AM technology is dated 1981 [6], a wide variety of technologies and materials have been developed and optimized in the past decades. In particular, the fabrication of ceramics components using AM techniques is nowadays of particular interest, not only from a research point of view but especially from an industrial one. Ceramics are materials known and used in several applications thanks to their hardness, high temperature resistance, electrical and optical properties [7], [8]. Therefore, ceramic components fabricated through AM not only maintain the aforementioned characteristics, but they also acquire complex and/or custom geometries suited for a particular application or behavior [9], [10].

It is possible to categorize AM technologies into direct and indirect ones [11]. The first family refers to all those methods where the material is being directly deposited onto the previous layers, specifically adding material only where it is required by the CAD model. On the contrary, in an indirect process, first the material is deposited all over the printing area and, after, it is being selectively consolidated following the slices of the CAD model; in this sense, the final object is obtained only upon removal of the excess, not solidified material. It should be noted however, that in the ceramic processing through AM, hardly any technique allows for the fabrication of a ready-to-use part, as it might be for certain AM technologies used for the

fabrication of metals and polymers. Apart from very few examples, the starting material of AM of ceramics always require for the addition of organic solvents, additives and/or binders which must be removed from the green part through thermal treatments, being either a drying stages at low temperatures (i.e.,  $< 200\text{ }^{\circ}\text{C}$ ) or debinding (i.e.,  $< 600\text{ }^{\circ}\text{C}$ ) and sintering (i.e.,  $> 1000\text{ }^{\circ}\text{C}$ ) profiles.

Considering the work that will be later presented, the principles of these three different AM techniques are hereafter described, highlighting their potentials and drawbacks in the fabrication of ceramic components. [11]. Particularly, An example of a direct printing method is the Direct Ink Writing (DIW) technique, while both slurry- and powder-based technologies, including Digital Light Processing (DLP), Layer-wise Slurry Deposition (LSD), are part of the indirect AM family.

### 1.1.1 Direct Ink Writing

Direct ink writing (DIW) is a direct extrusion-based AM technique, in which a shear-thinning ink is formulated from a ceramic powder suspension and extruded from a nozzle in a filament fashion producing a 3D object [12], [13]. A graphical representation of its functioning is shown in **Figure 1.1** (a). While its fairly minimalistic setup requirements make DIW one of the most widely employed technique in the fabrication of ceramic parts, several drawbacks have been limited its applicability. One is certainly represented by the mechanism controlling the shape retention of the extruded filament via DIW. Indeed, the ink should be formulated in order to behave like a viscous gel, thus able to break down its network as the extrusion forces are applied and easily flow out of the nozzle [14]. Once deposited, its shape retention is guaranteed by the quick increase of the viscosity of the ink, which avoid the deformation of the filament. In order to obtain such viscoelastic character, several mechanism can be activated, such as a change in pH, in the ionic strength of the solvent, or addition of polyelectrolytes to induce particle flocculation, as well as addition of gelling agents [15]–[17]. Specifically, the solid loading and the interaction between the ceramic particles and the organic phase should be optimized in order to tailor the ink storage modulus ( $G'$ ) and yield stress ( $\tau$ ) and, therefore, the self-supporting ability of the deposited structure [18]–[20]. Additionally, the absence of support limits the complexity

of printable designs of DIW: severe overhangs might be printed only after a precise tailoring of the part orientation and/or by addition of a sacrificial material that should be later removed [21], [22].

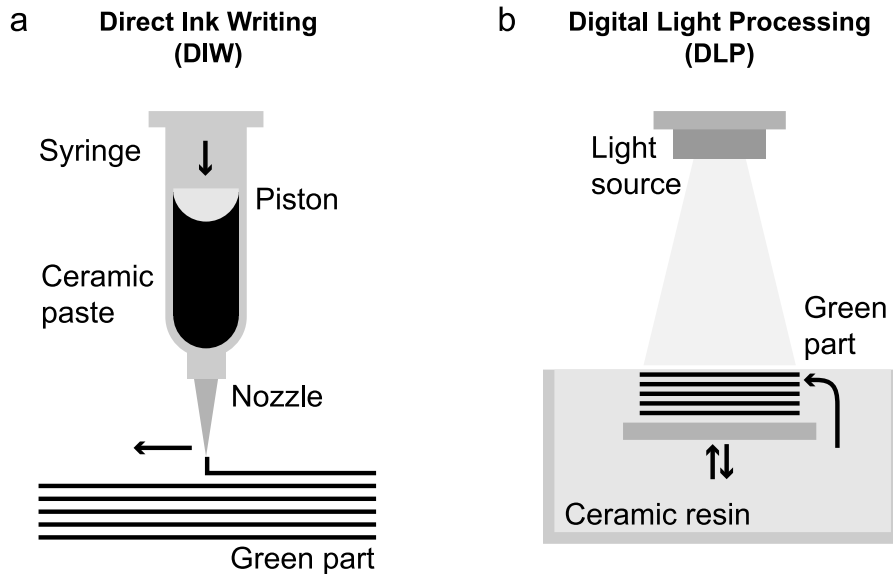


**Figure 1.1.** Schematic representations of the (a) Direct Ink Writing (DIW) and (b) Digital Light Processing (DLP) techniques.

### 1.1.2 Digital Light Processing

DLP is instead an example of indirect AM technique and, together with stereolithography (SLA), it forms the vat photopolymerization family [1]. DLP relies on the reactivity of photo-sensitive resins containing dispersed ceramic particles that are selectively cured forming a 3D component [23], [24]. Contrary to DIW, suitable slurries for DLP must possess a water-like viscosity, thus being able to flow on and off the building plate; there, thin layers of material are selectively cured, one on top of the other (**Figure 1.1** (b)). Being an indirect technique, DLP requires for the preparation of more material than that which will constitute the final object [25]. The liquid surrounding the cured part can only partially act as support, limiting the fabrication of too severe spanning features and tiny, suspended filigrees without the introduction of additional supports [26]. The formulation of a high reactive ink is ideal for the DLP technique; typical slurry compositions should include a monomer mixture, initiator and additives for the

dispersion of the ceramic powders [27]. Specifically from this latter perspective, the fabrication of ceramics via DLP has been limited due to the interaction between the suspended particles and the incident light, which is scattered and/or absorbed [28], thus resulting in defected objects or longer process times (i.e., longer exposure times needed and/or smaller layer thickness). A fine matching of the refractive indexes (RI) is required in order to increase the curing depth, the resolution and the rigidity of the printed component [29], [30] (see later, §2.2).

### 1.1.3 Layer-wise Slurry Deposition

The LSD technology is a recently patented process [31] that combines elements of tape and slip casting. Specifically, tape casting is a forming technique which enables the fabrication of thin tapes and sheets of ceramic by casting (by means of a doctor blade) and drying of a low viscous slurry into a flat plane [32]. Additives and binders influence the mechanical properties of the final tape, as they can prevent the crack and curl of the tape. Typical applications of this process are in the electronic industry, as tape casting can also be used in the fabrication of multilayer capacitors [33], [34]. Nonetheless, the average thickness of the tapes is limited to about 50-100  $\mu\text{m}$  because of the drying stage, which is usually conducted by leaving the casted films for 12-24 h at room temperature. Slip casting, on the other hand, is based on the deposition of a ceramic slurry inside of a porous mold: due to the capillary forces, the slip dries up and large, hollow shapes with modest wall thicknesses are therefore fabricated [35]–[37]. Slips require higher viscosities with respect to the tape casting slurries; they should easily be poured inside of the mold and fill out all the present cavities, but also avoid the development of an inhomogeneous wall thickness. Note that while both rheological requirements and specific formulations of tape and slip casting differ, they both rely on the optimization of a stable dispersion of ceramic powders into a liquid medium. Along the present work and specifically in Chapter 3, the terms *slip*, *slurry* and *suspension* will be used as synonyms.

The LSD technique can be schematized as in **Figure 1.2**. A first thin, flat layer of a ceramic slurry is deposited over a heated and porous building plate, which promotes drying through evaporation and capillary absorption; as additional layers of slurry are spread one on top of the others, the previously dried layers will continue to act as a porous mold. The LSD technique is

a deposition procedure that can be combined with the working principle of powder-bed based AM techniques, such as Binder Jetting (BJ) or Powder Bed Fusion [38], [39].

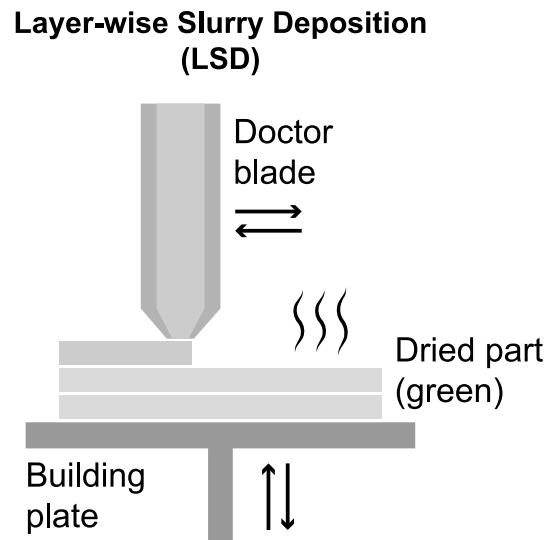


**Figure 1.2.** Schematic representation of the Layer-wise Slurry Deposition technology.

In BJ, the deposition and spreading of layers of ceramic powders is followed by the inscription of the final shape by selective ejection of a binder. Powder-bed fusion technologies such as Selective Laser Sintering (SLS) inscribe the final shape by locally heating and sintering the ceramic particles using a laser; given the high temperatures required for ceramic sintering, these processes are far less common. In both cases, the presence of a solid-filled layer overcomes the need of sacrificial materials or scaffolding structures previously reported for DIW and DLP: the fabrication of steep overhangs is guaranteed by the support given by the surrounding material. As a result, different parts can be stacked within the same bed, thus increasing the productivity and decreasing material waste usually associated to indirect techniques [11]. Thanks to the subsequent extraction/washing step, the cured parts can be extracted from the bed and thermally processed in order to obtain dense ceramic components. In conventional, powder-bed processes, the printing accuracy relies upon the fine optimization of the binder/powder (or laser/powder) interaction and of the wettability and flowability of the powder feedstock, which in turn are affected by the appropriate selection of the particles size distribution and shape. Indeed, while spherical and larger particles are ideal for their spread-ability and binder diffusion, they result in poorly packed systems, thus limiting the density of the green parts to ~ 50% [40], [41].

From this perspective, the evaporation and absorption forces associated with solvent removal in a LSD deposited layer bring the particles closer to each other, resulting in an increased green density (with values comparable to slip casting) [31], [38], [42]. A denser, stronger green body allows for the LSD process to be more easily combined with subtractive techniques and opens the door for process hybridization, such as with the LSD-DIW hybrid technology: in this case, machining and ink extrusion steps are alternated with the deposition of fresh layers of slurry. This way, it is possible to embed a secondary material inside of the ceramic matrix [43], thus allowing for the fabrication of multi-material parts. Complete description of this technique will be given in Chapter 3, while some of the basic principles of multi-material AM are reported in § 1.2.2.

## 1.2 Hybrid additive manufacturing of ceramics

The rapid development and optimization of AM techniques have changed the way that advanced ceramics are fabricated and increased their printable complexity. As a result, precise requirements for a successful printing process for each AM technique can be defined, and thus their limitations [44], [45].

As reported above, a common drawback associated to most AM approaches rises from the layer-by-layer construction: printing of complex geometries characterized by overhangs or small features requires the addition of support structures, excess or sacrificial material, or longer printing times in order to avoid structural collapse [46]–[48]. Moreover, it should be highlighted that the piling up of layers results in the presence of multiple interlayer interfaces and in a stair-stepping effect on the surface of the part, which lead to a reduced strength and mechanical response of the printed parts [49], [50]. Several strategies can be adopted to limit such phenomena, including the optimization of the part orientation and/or the use of a variable layer thickness [51]–[53]. Nonetheless, the process remains still based on a planar construction: the stair-stepping effect is reduced but not removed, and the interlayer interfaces remain [54].

The combination of multiple manufacturing techniques into a unique hybrid system could represent a novel solution to overcome the aforementioned limitations. Following CIRP Annals

definition published in 2014 [55], a hybrid manufacturing process is described as the result of “simultaneous and controlled interaction of mechanisms and/or energy sources having a significant effect on the process performance”. Indeed, the goal of a hybrid manufacturing technique is to exploit the advantages of the singular methods combined unlocking novel capabilities, thus validating the so called “1+1=3” effect [56].

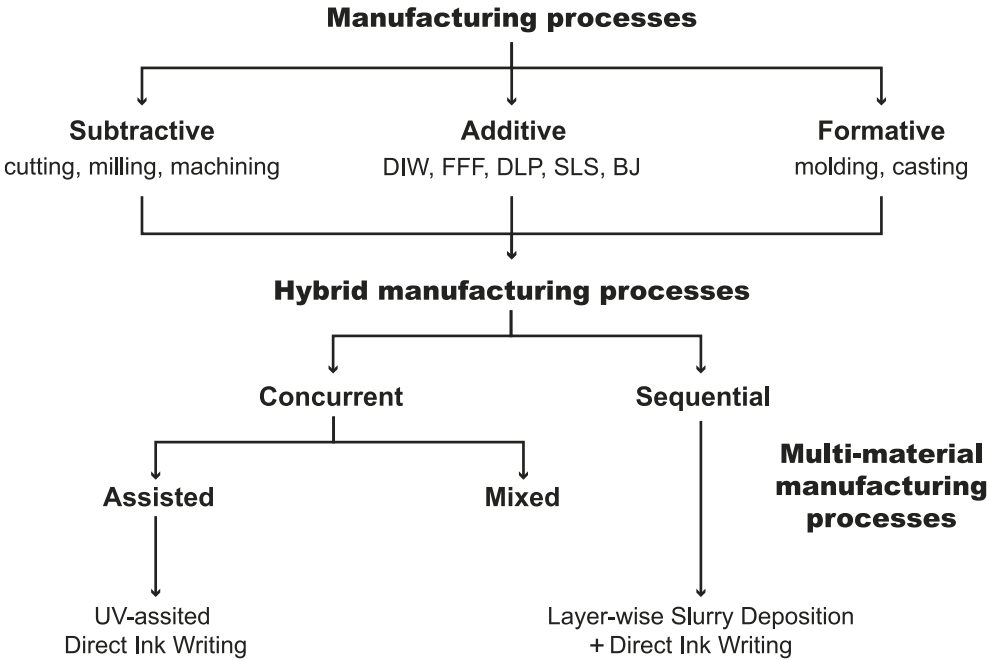


**Figure 1.3.** Graphical map representation of the subdivision of manufacturing, hybrid and multi-material manufacturing processes

As showed in **Figure 1.3** and following what proposed by Lauwers et al. [55], the hybrid manufacturing techniques can be divided into two groups, consisting of (i) concurrent processes which synergistically act in the same processing zone and at the same time, and (ii) sequential techniques which advantageous effect is given by the separate action of different processes on the same zone. A further classification of the concurrent technologies can be made by differentiating between assisted and combined processes: in the first case, a main (primary) manufacturing method is coupled with a secondary energy source, whereas in the second case, the merged processes are all primary shaping techniques.

Furthermore, it should be noted that hybrid techniques can be the result of the combination of processes deriving from either the same manufacturing macro category (i.e., subtractive, formative or additive) or from different ones. In the first case, the aim is to enhance the process

capabilities; different subtractive methods can be coupled together, for example, in order to increase the surface quality and/or reduce tool wear [57]. On the other hand, the goal of hybrid processes deriving from different manufacturing macro categories is to further extend the application area of such techniques, not only in terms of materials but also of geometrical complexity.

### 1.2.1 UV-assisted Direct Ink Writing

UV-assisted Direct Ink Writing (UV-DIW) is a concurrent, assisted hybrid process where a photocurable suspension is extruded through a nozzle and consequently cured by an external UV source. A schematic of the UV-DIW technique is displayed in **Figure 1.4**. Such combination is particularly interesting as it is set to overcome most of the limits of DIW and DLP. Specifically, light scattering and/or absorption phenomena, arising from the light-particle interaction, do not have an effect on the process resolution, which instead is dictated by the diameter of the extrusion nozzle; the curing depth also becomes less relevant, as consolidation of the outer shell is sufficient to guarantee shape retention. The consolidation of the ink relies on the photocuring process, which generally proceeds faster and develops higher viscosity and stiffness compared to gel reconstruction; this way, the shape retention of the filament is achieved without extensive optimization of the ink rheology.



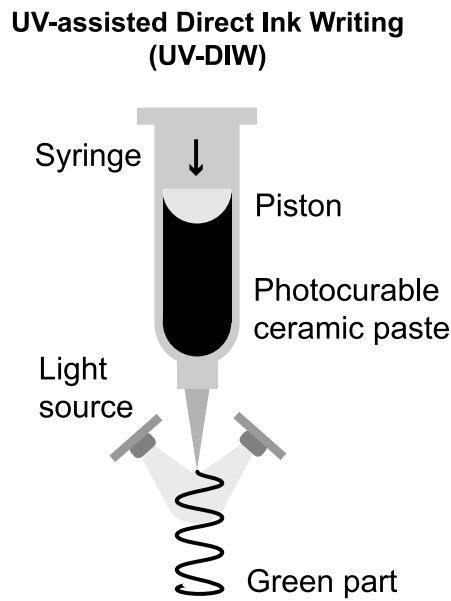


**Figure 1.4.** Schematic representation of the UV-assisted Direct Ink Writing technique.

Few examples of conventional layered structures produced via UV-assisted DIW with ceramic suspensions have been reported in literature, which primarily focused on generating structures with increased shape stability and more severe overhangs [58]–[62]. However, the real benefit of the hybrid process resides in the opportunity to overcome the traditional stacking of 2D layers; in fact, the fast solidification rate coupled with the unconstrained mobility of the nozzle, enables the direct extrusion of overhangs and undercuts, and the production of self-supporting, filigree patterned parts, a process referred to as freeform fabrication. Its capabilities can be further enhanced by robotic additive manufacturing (RAM) [63], [64]. Lebel et. al [65] and Farahani et al. [66], for example, were able to fabricate carbon nanotube nanocomposite microcoils thanks to the rapid exothermic reaction provided by the polyurethane based matrix (**Figure 1.5 (a-b)**); specific combinations of printing speed and extrusion pressure enabled the fabrication of support-less and freeform structures. Similar results, reported by Maeng et al. [67], represent one of the rare examples of freeform ceramic structures fabricated via UV-DIW: porous biphasic calcium phosphate components with unsupported features were successfully printed thanks to the precise selection and tuning of the conversion rate of the photocurable phase (**Figure 1.5 (c)**). Specific printing parameters and requirements of this hybrid technology will be described in Chapter 2, with particular focus on the fabrication of silica and silicon nitride-based parts.

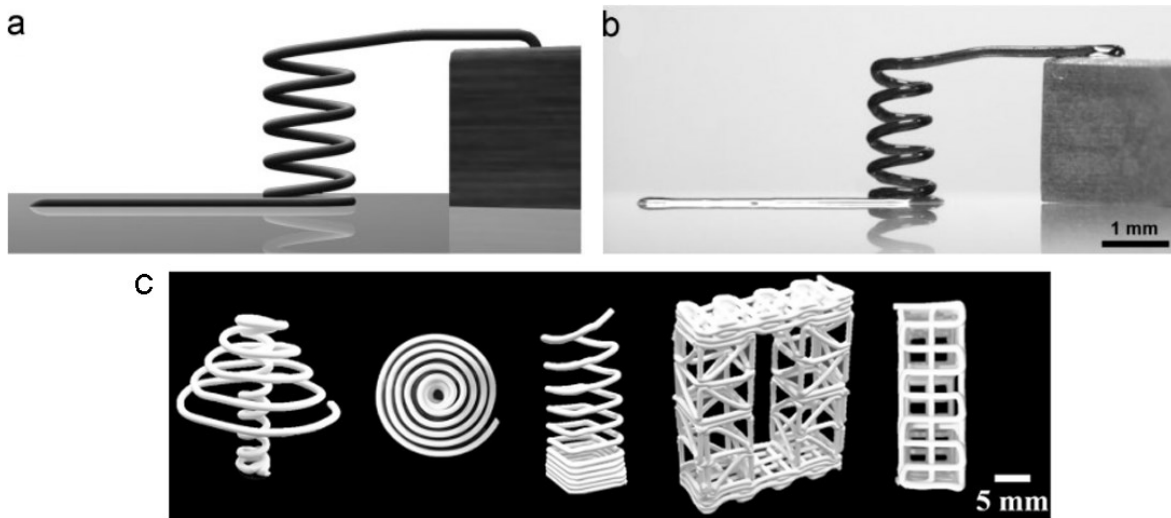


**Figure 1.5.** Nanocomposite coil fabrication published by Lebel et al. [65]: (a) virtual image showing the programmed UV-DIW fabrication of the coil; (b) optical microscope image of the actual deposited coil. (c) optical images of self-supporting structures having microporous filaments published by Maeng et al. [67].

## 1.2.2 Additive manufacturing technologies for multi-material components

As previously described, the continuous development and optimization of AM techniques have been proven able to overcome the drawbacks related to conventional manufacturing methods. While current AM techniques might be limited by their process requirements, the combination of different processes within a hybrid technique allows to increase part performance, complexity and functionality. Similarly, the development of multi-material AM methods is set to further enhance the final properties of the components thanks to a continuous or discrete variation of the material composition within and across layers [68].

Following the review reported by Vaezi et al. [69], those techniques, in which the secondary material is being added by infiltration and/or as coating, are not considered here, as well as processes where raw materials are mixed or composited before the effective fabrication of the part. Most of the existing examples of multi-material AM report parts fabricated with different materials from the same family (polymers, metals or ceramics) [70]–[74], while only few of them successfully joined dissimilar materials [75], [76]. Such scarcity results from their differences in consolidation mechanisms (i.e., sintering, polymerization, melting/solidification) and

physical properties (i.e., thermal expansion, melting temperature, chemical reactivity); other issues are related to the development of suitable technologies. Indeed, in order to deposit different materials within the same component, the AM system should allow for their selective dispensing on the building plate. Direct, material extrusion technologies, such as DIW and FFF, can be easily integrated with multiple nozzles and thus allow the adjacent deposition of different materials [77]–[80]; however, such techniques are limited in terms of printing resolution and green density. On the other hand, indirect AM approaches (i.e., DLP, SLS, and BJ, including LSD) are better suited for across layer material variation and anyway require complex material-changeover systems and cleaning stations [81]–[85] (**Figure 1.6** (a-b)).

For these reasons, the most interesting results on the joining of different materials have been reached by employing hybrid, sequential AM technologies. In fact, the most suitable technology for each material and geometry can be selected independently.

A field that could benefit from the development of such multi-material technologies is the electronic and information industry. The recent and rapid development of small and complex devices has increased the demand of components with minimum weight and size and tailored performance. The fabrication of sensors or embedded circuits, for example, has so far been limited to conventional processes, such as tape casting of glass-ceramic sheets and screen printing of metallic paths; the different parts are then pressed together in order to fabricate bulk devices. Complex assembly steps are required in order to properly connect the metallic features and avoid short-circuits, while only relatively simple shapes can be obtained.

Multi-material parts with embedded circuits have been fabricated via AM approaches. Voxel8 Inc., a start-up company founded by Dr. Lewis [86], produced PLA-based components containing conductive silver paths, thanks to the combination of FFF and DIW. Similarly, Li et al. [87], integrated DLP and DIW to obtain a polymer matrix with embedded light emitting diode (LED) blinking circuitry. Nonetheless, the use of a polymer matrix hinders the applicability of such devices in extreme atmospheric and/or environmental conditions and in fields requiring high thermal and/or chemical stability and mechanical properties (i.e., radars, micro-reactors). In this sense, the development of hybrid AM techniques able to fabricate ceramic-metal components is needed. Recently, Wang et al. [88] combined DIW with a selectively laser-activated plating process to produce a 3D LTCC-based circuit board with an internal cooling channel for a high-

power LED. Highly complex and precise devices could be obtained, but the process actually consists in the separated fabrication and thermal treatment of the ceramic matrix and of the metal features (**Figure 1.6** (c-d)). A more integrated system is proposed by Raynaud et al. [89]: here, layers of a photocurable HTCC ceramic slurry are cured via SLA leaving open paths, which are then selectively filled with a tungsten-based ink deposited via DIW; co-sintering of the ceramic and metal allows to produce dense ceramic components with various complex embedded circuits (**Figure 1.6** (e-g)). Another recent example of hybrid AM approach potentially able to manufacture ceramic-metal parts is the LSD-DIW technique developed at the Bundesanstalt für Materialforschung und-prüfung (BAM) in Berlin, Germany. At the current stage of development, de Melo Bernardino et al. [43] have showed subsequent slurry deposition, drying, machining and extrusion of a sacrificial ink, and the fabrication of dense porcelain components with embedded hollow 3D channels.

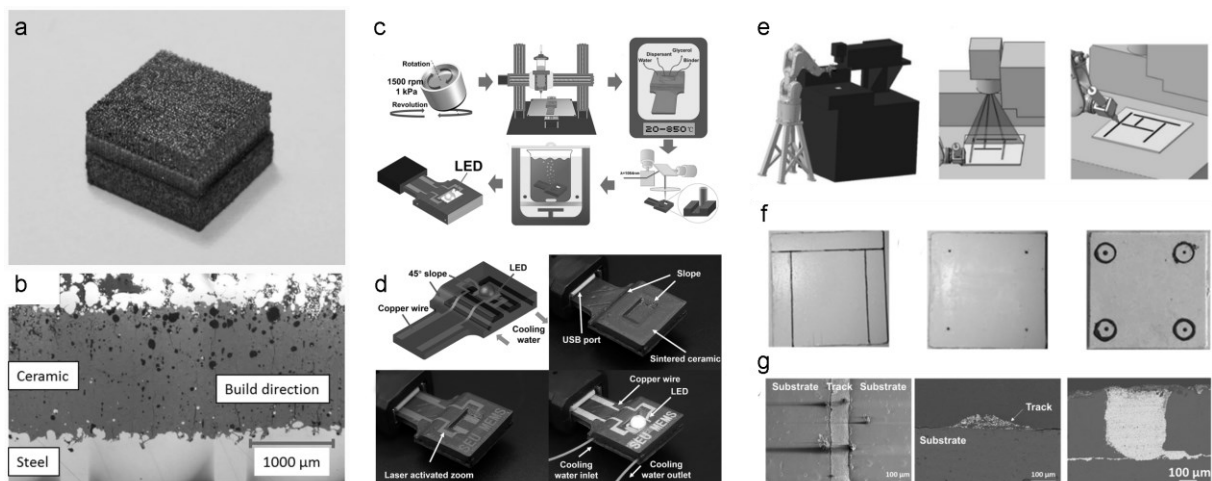


**Figure 1.6.** Koopmann et al. [81]: (a) tri-layer sandwich structure featuring a 10-mm base and a height of approximately 7 mm, and (b) SEM image of its cross section with upper and lower steel layers embedding the ceramic layer (dark gray) in the middle. Wang et al. [88]: (c) process chain of ceramic HAM technology for functional LTCC slurry preparation and (f) schematic sketch of the circuit board, sintered substrate and working condition. Raynaud et al. [89]: (e) assembly for the production of bi-material objects combining robocasting and stereolithography processes; (f) micrograph of green parts showing (left to right) uncovered tracks, embedded tracks with vias and armored vias; (g) SEM images of HTCC components showing (left to right) uncovered tracks and embedded track connected to surface by vias.

The present research fits in with this scenario, focusing on the fabrication of ceramics and ceramic-metal components through the development and optimization of hybrid UV-DIW and LSD-DIW technologies. Such manufacturing methods have been proven able to exploit the capabilities offered by conventional AM techniques, specifically increasing the geometrical complexity of the printable structures and broadening the range of application and functionality of the final part. In this sense,

the present research should be considered as further optimization and advancement of both hybrid technologies. Analysis of their manufacturing limitations and capabilities allows to investigate novel and unexplored combinations between designs, materials and processes. Particularly from the UV-DIW perspective, its layer-less construction allows to avoid surface roughness and interlaminar interfaces, thus representing a new possible way to fabricate ceramics known for their well-defined optical (i.e., silica glass) and mechanical properties (i.e., silicon nitride). Contextually, such characteristics can be further exploited by increasing control over the printing parameters and orientation, ultimately maximizing the design freedom of the UV-DIW method. On the other side, research related to the production of multi-material devices is a trending, yet not trivial topic; the newly developed LSD-DIW technique has the potential to overcome the limits of other conventional or hybrid AM technologies. The high green density provided by the LSD technique combined with milling and DIW, represent a unique way to introduce multiple metal inks into a ceramic-based matrix using a fully integrated step-wise manufacturing technique.





## 2 Hybrid UV-DIW technology

Additive manufacturing of ceramic and glass materials has been developed extensively over the past years, revealing the strengths and limitations of the various technologies. In the present Chapter, a hybrid extrusion-photopolymerization process (UV-DIW) is developed; the aim is to exploit the benefits of the additive manufacturing technologies being coupled and further expand their range of applications.

The key attribute of the UV-DIW technology is its freeform ability which ultimately relies on the combination of an optimized design of the hybrid setup with an adequate curing speed of the ink. From this latter perspective, silica and silicon nitride were identified as suitable ceramics to verify the limits of the freeform ability of the setup caused by light-particle interactions. Specifically, the penetration of the light in a polymerizable medium loaded with solid particles is governed by their relative difference in terms of refractive index; in this sense, due to the similar value compared to acrylates, silica allow for higher curing depths compared to silicon nitride. From such perspectives, the goal was to obtain suspensions not only having an adequate solid loading and particles dispersion, but especially being able to cure rapidly.

In particular, the specific mix designs and curing rates suitable for printing were defined for both silica and silicon-nitride based inks. Particle surface properties and liquid-particle interaction forces were found to be the most critical parameters to control the maximum particle loading and flow behavior of the inks. Silicon nitride particles were modified by introducing a silane agent, thus increasing the particles dispersion, while the H bonding capability of the liquid phase in the silica slurry was tailored to avoid a shear thickening behavior. Modifications of the silica-based formulation were made to enhance the final glass properties. A cerium/silica based ink was optimized in order to obtain transparent multicomponent glass components possessing photoluminescence characteristics.

The fabrication of support-less components using the UV-DIW technology evidenced the limits of the 3-axis setup: the locked vertical direction of the printing head results in a discontinuous



interaction between the UV light and the filament, decreasing the printing accuracy; moreover, there is a risk of collision between the printing head and the printed component. Therefore, a custom UV LEDs setup was designed and then mounted as the end-effector of a 6-axes robot arm. Regular lattices were printed using a commercially available resin, thus allowing the calibration of the printing parameters (i.e., light intensity, printing and extrusion speed).

## 2.1 Hybrid setup and printing process

The hybrid equipment consisted of a set of UV-LED chips (395–400 nm, 10–15 lumen) distributed in a circular array around a UV block dispensing system – syringe and nozzle tip (Vieweg GmbH, Germany) mounted on a delta printer (Delta 2040 Turbo 2, WASP, Italy) and controlled by an air pressure digital dispenser (DC 307, Vieweg GmbH, Germany). Pictures of the equipment are shown in **Figure 2.1**.

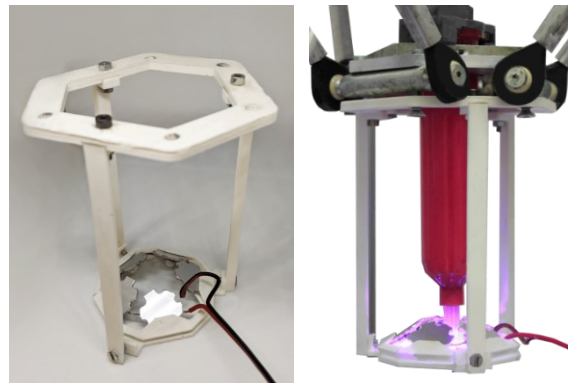


**Figure 2.1.** Hybrid UV-DIW equipment printed in PLA (left) and mounted over the head of a delta printer (right).

The LEDs were oriented so that their radiation is focused just below the nozzle tip, enabling fast photopolymerization in air right after the ink extrusion. The relative positioning and orientation of the UV-LEDs arrays around the nozzle was determined by considering the inverse proportion existing between light intensity and distance ( $I \propto d^2$ ). Five LED chips were placed in series, forming a ring, at a distance of  $\sim 20$  mm from the nozzle tip and an angle of  $30^\circ$  with respect to the ground plane. The UV-LEDs array was powered with a 24 V – 10 A power supply

unit and their intensity, measured with a UV power meter (Light Checker C9386, Hamamatsu Photonics K. K., Japan), was  $6 \text{ mW cm}^{-2}$  at the point of extrusion.

## 2.2 Ink design and preparation

As described, the printing process of the UV-DIW technique is based on the extrusion of a photocurable ink. Specifically for this work, ideal feedstocks are represented by well dispersed ceramic suspensions possessing a shear thinning behavior, even at high particle loading, thus ensuring a stable flow through the nozzle at moderate shear rates during printing; at the same time, they react rapidly upon irradiation and retains the extruded shape. Such consolidation process depends on the photopolymerization of the polymer network, usually consisting in a mixture of acrylate monomers and/or oligomers with photoinitiators.

While two different photopolymerization mechanisms exists, namely radical and cationic, it is the first one which is commonly employed in the AM fabrication thanks to its faster cure rates compared to the cationic mechanism [90]. The radical process consists in three phases being (i) photoinitiation, (ii) propagation and (iii) termination. While in the first step, radicals are being generated upon irradiation at specific wavelength and intensity, dictated by the photoinitiator structure, propagation and termination steps strictly depends on the acrylates characteristics of the acrylates and, particularly, on the number of functional groups. Specifically, due to their ability to create stable radicals, methacrylates reactivity is lower compared to that of acrylates. In addition to that, single functional groups do not allow to create a proper network upon curing, as the propagation phase is readily interrupted once two molecules react together; for these reasons, diacrylates and triacrylates are usually employed [91]. A list of the most commonly used acrylates is shown in **Table 2.1**.

**Table 2.1.** List of commonly used ceramics, solvents and acrylates with their refractive indexes (at  $\lambda=500$  nm).

<b>Acrylates</b>	<b>Refractive index</b>
Trimethylolpropane triacrylate, TMPTA	1.474
Polyethylene glycol 200 diacrylate, PEGDA	1.464
Tetra(ethylene glycol) diacrylate, TEGDA	1.459
Hydroxyethyl methacrylate, HEMA	1.452
Hydroxyethyl acrylate, HEA	1.445
<b>Solvents</b>	
2-Phenoxyethanol (POE)	1.534
2-Propanol (IPA)	1.375
<b>Ceramics</b>	
Silicon carbide, SiC	2.684
Barium titanate, BaTiO <sub>3</sub>	2.495
Silicon nitride, Si <sub>3</sub> N <sub>4</sub>	2.034
Alumina, Al <sub>2</sub> O <sub>3</sub>	1.760
Silica, SiO <sub>2</sub>	1.458

The curing speed of the photocurable part can be quantified with the critical light energy dose required to start the polymerization, which directly influences the curing depth of the ink. Such effect can be described considering the relationship proposed by Griffith and Halloran based on the Beer-Lambert law [92]:

$$C_d \propto \frac{d}{\phi Q} \ln \left( \frac{E_0}{E_c} \right) \quad (1)$$

Where the curing depth ( $C_d$ ) of a loaded photocurable suspension is proportional to the average particles size ( $d$ ) and the exposure energy dose ( $E_0$ ), while it is inversely proportional to the volume fraction of the ceramic particles ( $\phi$ ), the critical energy ( $E_c$ ) and the scattering ability of the suspension ( $Q$ ). Specifically, the latter represents the refractive index (RI) difference between the ceramic particles and the photocurable phase ( $Q \propto \Delta n^2 = (n_{\text{ceramic}} - n_{\text{solution}})^2$ ). By following (1), since adequate solid loadings are necessary to readily sinter dense ceramics, higher penetration depths can be achieved only by fine matching the RI of the reagents. In addition to that, a limited mismatch of the RI is associated to a good dispersion of the ceramic

particles. This is particularly true considering the Van der Waals forces which governs the attraction between two identical particles [93] expressed as:

$$F_{vdw} = \frac{-Aa}{6\pi h}, \text{ with } A = f(\varepsilon^2, \Delta n^2) \text{ and } \varepsilon = f(n) \quad (2)$$

Where  $\varepsilon$  is the dielectric constant and  $n$  the refractive index; in this sense, when particles and medium matches their refractive indexes, both terms of  $A$  become negligible, thus minimizing the Van der Waals attraction forces. Hence, as a minimum in free energy at the equilibrium thickness is reached, particles agglomeration is avoided and thus the dramatic increase in the ink viscosity [94], [95].

However, such tuning of the RI is not trivial due to the wide range of values possessed by ceramics (1.460 ÷ 2.680), compared to the ones of the acrylates usually employed in DLP processes (1.445 ÷ 1.474), as displayed in **Table 2.1**. From such perspectives, silica ( $\text{SiO}_2$ ) and silicon nitride ( $\text{Si}_3\text{N}_4$ ) powders were identified as the best candidates to verify the limits of the freeform ability of the setup. Specifically, the refractive index of  $\text{SiO}_2$  matches the one of the acrylates, thus theoretically allowing greater curing depths. On the other side, the mismatch between the RI of  $\text{Si}_3\text{N}_4$  and the acrylates should impose a limit not only in the penetration of the UV light but also in the efficient dispersion of the particles.

It is worth noting that the acrylate mixture represents the main solvent in which the ceramic particles are suspended; the surface properties of both  $\text{SiO}_2$  and  $\text{Si}_3\text{N}_4$  and their interaction with the acrylates will need to be considered in order to avoid agglomeration. Therefore, different ink design strategies were set up for the formulation of the two inks.

The general approach employed for the preparation of both inks which consisted in, (i) addition of the liquids, such as solvent and acrylates, to a mixing container, (ii) addition of decreasing fractions – from 5 wt% to 0.5 wt% – of the requested ceramic content in a stepwise process, each of which step followed by a mixing step of 2 min at 2000 rpm using a planetary mixer (ARE-250, THINKY, Japan) and a cooling step (4 °C) for 1 min. After that, the photoinitiator was added to the mixture. Due to the wavelength of the UV LEDs and its radicals forming

efficiency, bis (2, 4, 6-trimethyl benzoyl)-phenyl phosphine oxide (Omnirad 819, IGM Resins, Netherlands) was used as the photoinitiator [96].

The obtained suspensions were then stored in dark conditions and later loaded into a syringe. A defoaming step at 1200 rpm for 2 min was performed before printing in order to release the air entrapped during the loading procedure.

## 2.3 Silica ink

The following section has been partially published in: De Marzi, A., Giometti, G., Erler, J., Colombo, P., Franchin, G., "**Hybrid additive manufacturing for the fabrication of freeform transparent silica glass components.**" Additive Manufacturing, vol. 54, 2022, p. 102727, and in the patent application: Colombo, P., Franchin, G., Giometti, G., Schmidt, J., De Marzi, A., "**Production of Glass Bodies from Polymerisable Solutions**", WO2020/245427

Thanks to its exceptional optical transparency, thermal stability and chemical inertness, silica-based glass finds application not only in the everyday products (i.e., smartphone screens, kitchenware) but also in the chemical and pharmaceutical industry (i.e., vials, micro-fluidics channels), as well as in electronic devices (i.e., as sealing [97]), optical sensors and fibers [98], [99]. Conventional fabrication of glass components relies on blowing, lamination and molding processes, all of which require for the preparation of a glass melt which is either blown or pressed into a mold, cast on a molten tin vat or flattened through rollers, ultimately restricting the structural complexity to containers and laminas. Moreover, glass melting and cooling is associated with high temperatures, small working windows and the development of thermal stresses that might induce cracking, defects or crystallization [100].

In this framework, different AM techniques have been demonstrated for the manufacturing of transparent glass components, as the combination of process and material provides for extraordinary advantages. Melt extrusion, for example, is a direct technology similar to DIW: Klein et

al. [101], showed how a glass melt could be poured inside of a heated printer head, which, by moving inside of an annealing chamber, allows for the fabrication of transparent and geometrically complex shapes. Nevertheless, such technology still relies upon the preparation of a glass melt; a fine control over the glass viscosity and temperature distribution between the printer head, nozzle and annealing chamber is necessary in order to select proper printing rate and avoid crack formation. It is worth noting that such a process is relying entirely on gravity as driving force for the material flow. In this sense, a filament extrusion process – commonly referred to as Fused Filament Fabrication (FFF) – would allow for the application of an external force to drive the material deposition. The filament feedstock, consisting is fed to a heated printer head, where it gets molten and extruded into shape [102]. The use of borosilicate glass filaments has been proposed, yet it also requires specific machines able to reach higher temperatures at the nozzle tip as well as into the building chamber [103]. A different approach would be to load a thermoplastic filament with silica particles [104]; the great advantage here resides in the commercially available setup: FFF printers are not only easy to use, but especially fast and cost-effective [105]. Similar considerations can be made for the fabrication of glass parts through DIW: silica nano-powders have been successfully dispersed in a polydimethylsiloxane and tetraglyme mixture and then deposited forming thin-walled and spanning features [106]. Nonetheless, as previously described for direct techniques, the complexity of the printable structures is limited by both the nozzle diameter and the freestanding ability of the ink upon extrusion.

Higher printing resolutions could be achieved using vat photopolymerization techniques, including DLP, two-photon polymerization (2PP) and volumetric additive manufacturing [107]–[113]. In these examples, silica nanoparticles are mixed into a photo-curable medium; silica glass components having small features (i.e., even below 200 nm, as recently published by Wen et al. [114]) were successfully fabricated. Yet, highly transparent suspensions are required to allow for the penetration of the light and initiation of the photopolymerization process, thus limiting the amount of silica particles and requiring for the fine RI matching [94], [115]. In this sense, another proposed approach is the sol-gel route [116]: both extrusion and vat photopolymerization techniques have been proven able to fabricate transparent glass parts. Nevertheless, the hydrolysis process reduces the working window and slow drying stages are usually needed to prevent crack-formation [117].

Overall, different strategies have been proven successful for the fabrication of transparent silica glass components [94], [110], [118], [119]. Nonetheless, only few silica sources in powder form could be sintered to transparency; among these the most commonly used is a nanometric hydrophilic fumed silica powder, Evonik Aerosil OX 50 [107]. In addition to its sinter ability, provided by the small particle size (i.e., 40 nm [120]), Aerosil OX 50 is also widely employed in the development of colloidal suspensions: thanks to its low specific area (i.e., 50 m<sup>2</sup> g<sup>-1</sup> [121]), lower amount of solvent is required to disperse the particles [122]. For such reasons, Aerosil OX 50 was selected as main silica source for the present research work.

Even though such strategy allows for a high silica loading inside the ink, the particles still increase overall viscosity of the system. Accordingly, the resulting suspension does not flow homogeneously under the applied shear stress, thus affecting its printability. In this sense, several approaches have proven to be able to formulate highly loaded silica suspensions thanks to the optimal tailoring of the interactions between silica particle and its environment. Liu et al. [115], for example, based on the findings of Raghavan et al. [123] and Wozniak et al. [94], demonstrated how well-dispersed and highly loaded silica inks (53 wt%) can be obtained thanks to the presence of strongly H-bonding solvents (i.e., methacrylates and alcohols). Specifically, hydrogen bonding between the surface silanol groups of silica (Si-OH) and the hydroxyl groups of the liquid phase promotes the formation of a solvated layer around the silica particles, which increases the dispersion while maintaining a low viscosity. For this reason, different acrylates were considered with a focus on their functional groups. Crossing this information with an appropriate refractive index matching led to the choice of tetra (ethylene glycol) diacrylate (TEGDA) and hydroxyethyl methacrylate (HEMA) were chosen as photosensitive components. While both their refractive index is close to that of silica, thereby avoiding scattering effects, they differ in the number and kind of functional groups (**Table 2.1**). With only one vinyl group, HEMA cures slower than TEGDA, which has two reactive groups (curing time is 45 s and 1 s respectively, with a 395 nm UV light and 6 mW cm<sup>-2</sup> intensity). On the other hand, HEMA hydroxyl groups are more prone to form a solvation layer around the fumed silica particles surface [123], [124]. Hence, the greater the amount of TEGDA, the lesser the number of hydroxyl groups and the lower the interaction between the particles and the surrounding liquid; more particle-particle interactions result in higher viscosity of the ink, therefore a high amount of TEGDA also limits the amount of fumed silica admissible.

Therefore, to control the rheological behavior of the ink, it was necessary to investigate the effect of such acrylate mixture. As shown in **Figure 2.2**, the viscosity profiles of the suspension with a fixed amount of colloidal silica, and a variable TEGDA/HEMA ratio, were analyzed.

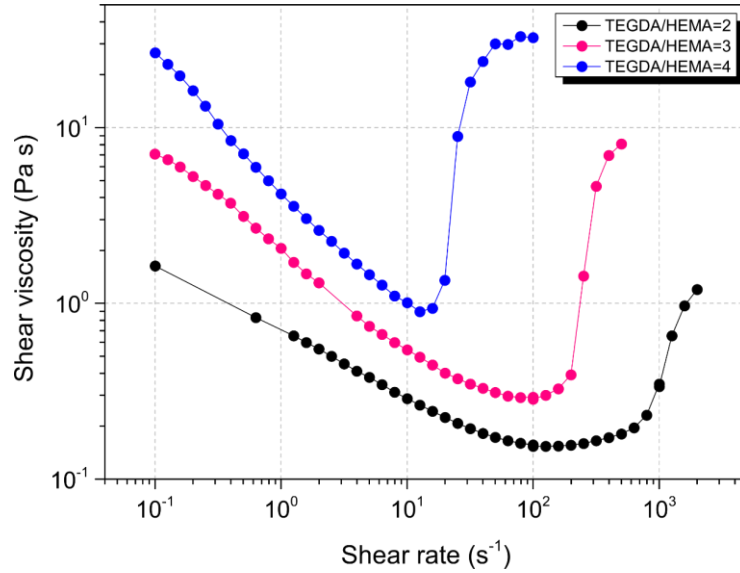


**Figure 2.2.** Silica-based inks with variable TEGDA/HEMA ratio at fixed silica content.

First, as expected with increasing TEGDA/HEMA ratio, the viscosity profile shifts to higher values. In addition, it can be noted that all inks have a shear thinning behavior at lower shear rates up to a critical point ( $\gamma_c$ ), after which they show a sudden increase in viscosity and become shear thickening. This behavior is linked to the solvation layer formed by HEMA, which reduces the affinity among particles and inhibits the formation of a 3D network. However, the particles can still form aggregates (hydroclusters) at high shear because of the loss of balance between particle-particle interactions and hydrodynamic forces [125]. This shift in rheological behavior represents an issue for the printing process, as the viscosity rapidly reaches high values and can be strongly affected even by small oscillations in the shear rate.

The behavior of a non-Newtonian fluid can be described by a power law model:

$$\sigma = K\gamma^n \quad (3)$$

where  $\sigma$  and  $\gamma$  represent the shear stress and shear rate, while  $K$  and  $n$  are respectively the consistency index and the power law index of the fluid equation [126]. Therefore, the maximum



shear rate at the nozzle walls can be derived from the equation for Newtonian fluids, adjusted by the Rabinowitsch correction, as follows:

$$\gamma_{wall} = \left(\frac{4Q}{\pi r^3}\right) \left(\frac{3n+1}{4n}\right) \quad (4)$$

where  $Q$ , and  $r$  represent respectively the flow rate and the radius of the nozzle end. With typical values of  $3-9 \text{ mm}^3 \text{ s}^{-1}$  for  $Q$ ,  $0.42 \text{ mm}$  for  $r$  and  $0.27$  for  $n$ , the printing shear rate can be estimated to be between  $75 \text{ s}^{-1}$  and  $125 \text{ s}^{-1}$ , in which all inks already show shear thickening behavior. Additionally, an even more dramatic rheological behavior inversion verifies at increasing silica contents. As displayed in **Figure 2.3**, a difference of 8 vol% in the silica content shifts the thickening effect from  $80 \text{ s}^{-1}$  to  $3 \text{ s}^{-1}$ .

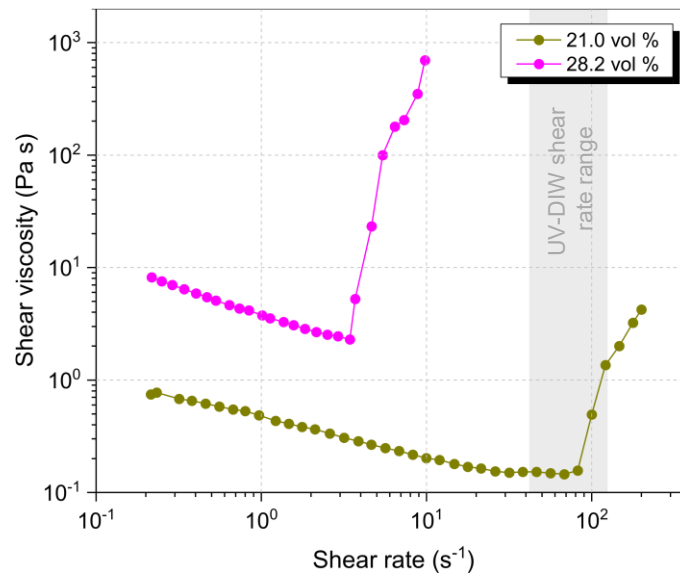


**Figure 2.3.** Silica-based inks with variable silica content at fixed TEGDA/HEMA ratio.

Indeed, concentrated colloidal dispersions – as the one represented by Aerosil OX 50 containing inks – were demonstrated to show a reversible shear thickening behavior [127]. Nonetheless, such phenomenon in the ink flow can be tailored. Arita et al. [113], for instance, functionalized the silica particles by addition of polyethylenimine complexed with oleic acid: the created steric effect allowed to prepare a highly loaded and shear-thinning mixture. However, preparation of such inks requires time-consuming extra steps for the addition and functionalization of particles. Moreover, the molecules introduced are all organic and have to be completely removed from the sample in order to obtain a fully sintered glass component, with high risk of component

damage upon debinding. In order to avoid this, a secondary liquid silica source (TEOS) was instead selected in the present formulation: not only it stabilizes the interactions between the silica particles, it also does not need to be fully removed and it contributes to the final ceramic yield. **Figure 2.4** shows the viscosity profiles of inks prepared with and without TEOS. As it can be seen, the chosen alkoxide have a double impact on the rheology. First, there is a difference of 2 to 3 order of magnitude on the viscosity between the two conditions: TEOS, unlike the other solvents discussed above, does not have any hydroxyl group and, consequently, it does not contribute to the creation of the solvation layer around the silica particles. In addition to that, due to the large molecule dimensions, TEOS acts as a steric agent; by remaining confined between the silica particles, it restrains the silica-silica interactions, thus competing against the shear-thickening effect arising at high shear rates.

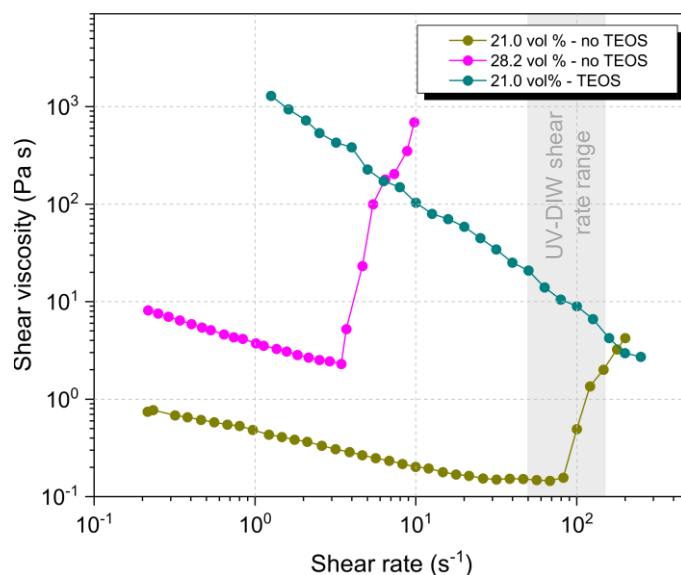


**Figure 2.4.** Effect of the amount of fumed silica and TEOS on the viscosity profile of LS, HS and HST inks; the grey area represents the printing range of shear rates.

2-Phenoxyethanol (POE) was chosen as an additional solvent for the silica particles: it lowers the viscosity of the ink and acts as a solvation agent thanks to its hydroxyl group. In addition to that, POE has a high boiling point, which helps maintain the ink stable at room temperature. However, due to the different refractive index with respect to the other reagents (**Table 2.1**), its amount should be limited in order not to compromise the ink dispersion and increase scattering. Here, a HEMA/POE weight ratio of 2.6 was employed.

For simpler reference in the next paragraph, the inks tested will be thereafter referred as:

- LS (Low Silica, no TEOS), containing the same percentage of fumed silica present in HST (21.0 vol%), but no TEOS;
- HS (High Silica, no TEOS), yielding the same amount of total silica in the sintered components than HST, but without the addition of TEOS;
- HST (High Silica, TEOS); the final ink composition, displayed in **Table 2.2**.

**Table 2.2.** HST ink composition.

	vol%
TEOS	34.4
HEMA	11.6
POE	4.3
TEGDA	28.1
Fumed silica	21.0
Omnirad 819	0.6

### 2.3.1 Printing and freeform ability

The critical energy dose required to start the polymerization process can be calculated using the Jacobs equation [128]:

$$C_d = D_p \ln \left( \frac{E}{E_c} \right) \quad (5)$$

where  $C_d$  (mm) is the curing depth at given exposure time,  $E$  is the energy density at the filament surface,  $E_c$  is the critical energy dose and  $D_p$  (mm) is the penetration depth of the ink. **Figure 2.5** (left) reports the curing depth of the HST ink as a function of the energy density; fitting with **(5)** returns the characteristic parameters of the ink:  $D_p = 0.79 \pm 0.07$  mm and  $E_c = 1.4 \pm 0.3$  mJ cm<sup>-2</sup> ( $R^2 = 0.97$ ). It should be noted that the value for  $E_c$  is fairly low compared

to other silica-based inks [113], [129], and confirms the high reactivity of the HST composition. Based on these values, curing of a filament extruded through a 0.84 mm nozzle and exposed radially ( $C_d = 0.42$  mm) would require only 0.4 s to be completed ( $E = 2.4 \text{ mJ cm}^{-2}$  with  $I = 6 \text{ mW cm}^{-2}$ ).

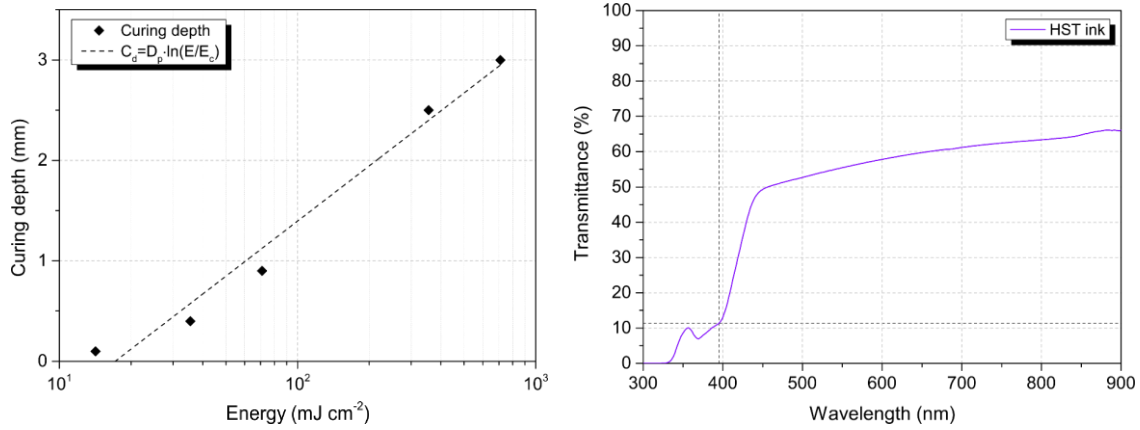


**Figure 2.5.** (left) Curing depth of the HST ink as a function of exposure energy density (logarithmic scale); (right) transmittance spectra of the HST ink.

**Figure 2.5** (right) reports the transmittance spectrum of the HST ink. As shown, in the range of the UV-LED chips emission wavelength (395–400 nm), the ink transmittance is around 12%, while it increases moving to the visible range, reaching a transmittance of 60% at 800 nm. While the trend agrees with the Omnirad 819 absorption spectrum, the transmittance is fairly lower compared to other transmission spectra of uncured fumed silica-based slurries [94], [107], [130], [131]. However, as mentioned before, the presented hybrid technology does not need highly transparent inks in order to fabricate freeform components, since the photopolymerization of the filament outer shell is enough for it to retain its shape.

In order to assess the effective curing of the HST ink upon irradiation, its photorheology behavior was analyzed by testing the shear viscosity evolution over time during a three intervals thixotropy test (3ITT) divided in: (i) 0.5% strain for 30 s at 1 Hz; (ii)  $100 \text{ s}^{-1}$  of shear rate for 30 s; (iii) 0.5% strain for 5 min at 1 Hz. Such analysis can be considered as a simulation of the actual printing process. The first interval represents the ink at rest inside the syringe, before extrusion. The second phase simulates the high shear conditions occurring during the ink extrusion through the nozzle. Finally, in the third interval, the no-shear condition is restored, resembling the ink state after extrusion. **Figure 2.6** shows the 3ITT curves obtained in two

different scenarios, being (i) a standard DIW printing process with no UV light present after extrusion (magenta line), and (ii) the hybrid printing process, with UV light switched on during the third interval for 1 s, 5 s and 10 s irradiation time (red, purple and cyan line, respectively) using a  $40 \text{ mW cm}^{-2}$  UV lamp. There is a substantial difference between the two conditions: if no UV light is present after extrusion, the ink does not regain its initial viscosity even after a long time ( $> 40 \text{ s}$ ). Note that the initial peak in viscosity registered by the test apparatus is a measurement artifact (it rises from the inertial response of the ink to the sudden change in the strain conditions). On the other hand, when the ink is UV-cured, there is a rapid increase of viscosity, reaching a value of  $\sim 10^5 \text{ Pa}\cdot\text{s}$  (3 orders of magnitude higher than its initial state) with only 1 s irradiation time. With increasing irradiation time, the viscosity further increases slightly reaching  $2 \cdot 10^5 \text{ Pa}\cdot\text{s}$  with 10 s. During the printing process, the deposited filament remains subject to UV irradiation as the print progresses, therefore additional curing can be assumed. In conclusion, the photopolymerization process allows the formation of a rigid cured part with very rapid shape retention, thus validating the freeform ability of the hybrid technique.

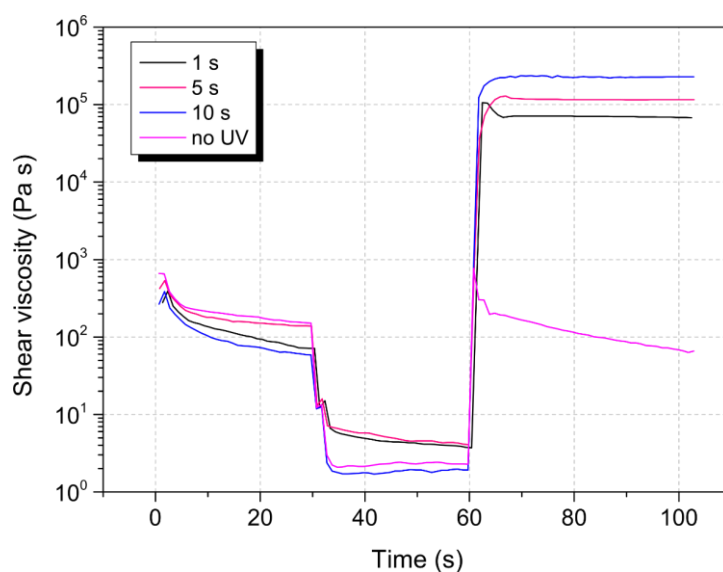


**Figure 2.6.** Three intervals thixotropy test (3ITT) on the HST ink with different UV exposure times.

From such perspective, the UV-DIW printing process parameters have to be tailored considering both the extrusion and the consolidation mechanisms. In particular, the first depend on the rheological characteristics of the ink: the feed rate, i.e., the moving speed of the print head, must match the flow rate of the ink through the nozzle; if the head moves slower, over-extrusion and slumping occur; if it moves too fast, under-extrusion results in stretching or breakage of

the extruded filament. On the other side, an adequate curing and shape retention of the filament is expected when the UV LEDs provides sufficient energy. As discussed, the curing energy is the product of light intensity and time of exposure, which in turn depends on the moving speed of the print head; this poses a theoretical upper limit for the moving speed to allow for the filament to be cured and retain its shape. On the other hand, a too low moving speed results in rapid curing of the material near the nozzle tip and, consequently, to its clogging [66]. In addition to that, both Farahani et al. [132] and Lebel et al. [65], fully described how the orientation of the extruded filament represents a critical aspect for the UV-DIW process, influencing the choice of printing parameters such as flow rate, moving speed and UV light intensity. Hence, the system capabilities and limitations were investigated by designing two structures of different type, i.e., being a support-less and a freeform one. Specifically for this work, the first kind of geometry refers to such structures that are self-supportive in a manufacturing process without introducing additional supports [66]. On the other side, freeform structures are represented by support-less geometries in which all space coordinates are varied independently, resulting in filaments with different orientation with respect to the printing head along the object [133].

First, a support-less coil geometry was designed: as a less, complex structure compared to freeform ones, it served to verify the limitations and capabilities of the UV-DIW setup and ink design. The coil had a nominal diameter of 8 mm and a variable pitch gradually increasing from the bottom (0.7) to the top (3.2). **Figure 2.7** shows a coil printed at  $5 \text{ mm s}^{-1}$  with a nozzle of 0.84 mm; the extruded filament was measured to have a thickness of  $0.89 \pm 0.07 \text{ mm}$ , thus demonstrating that a suitable pressure was selected. As it can be noticed, some differences exist between the designed pitch and the one measured in the printed coil which could be attributed to sagging of the truss. Indeed, almost 80 vol% of the HST ink is composed of liquid phase, of which only 1/3 is being cured (HEMA, TEGDA); the rest of the ink is inert during the printing process (TEOS, POE, Aerosil OX50). Consequently, only a small fraction of the cured extruded filament is prone to form a polymerized network, which is not able to completely withstand its own weight.

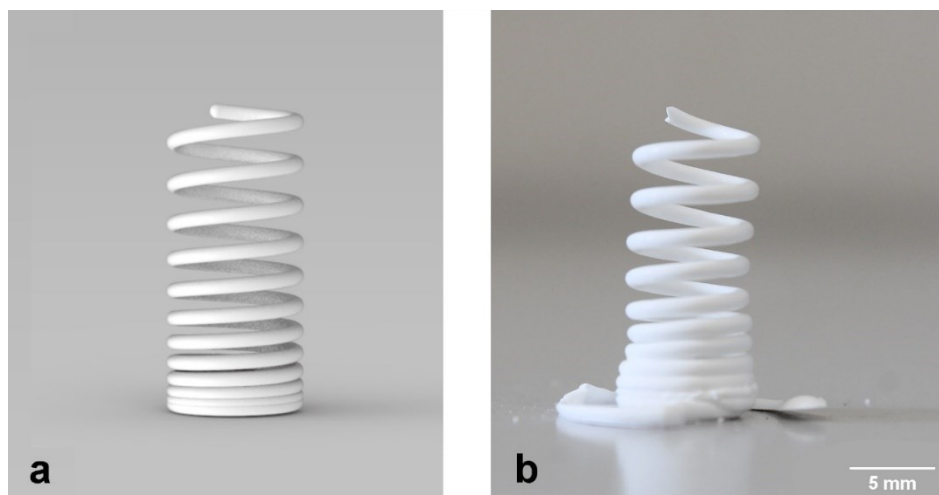


**Figure 2.7.** Comparison between the coil (a) digital model, (b) printed (green state).

To further demonstrate the UV-DIW technique capabilities in printing complex shapes, a freeform 3D honeycomb-like structure **Figure 2.8** (a), resulting from the stacking, in the vertical direction, of semi-hexagonal and linear patterns, has been designed. Specifically, it embodies a wide range of angles in the XZ and YZ planes, going from  $0^\circ$  (parallel to XY plane) to  $90^\circ$  (where the semi-hexagonal and linear patterns connect). Such shape could not be produced using DIW alone; in fact, the process is based on in-plane deposition and subsequent stacking of XY layers in the Z direction. Overhangs and non-planar constructs could only be attained with the aid of sacrificial supports or by embedding the printed filament into a viscoelastic gel (embedded direct ink writing, EDIW) [21], [134]–[136]. Both strategies require the use of a secondary material that has to be tailored to specific rheological requirements in order to sustain the object suspended features; moreover, it has to be later removed from the printed object with challenging cleaning, chemical or thermal decomposition steps. Furthermore, in EDIW the adhesion between adjacent printed layers can be hindered by the presence of the viscous gel at the contact point.

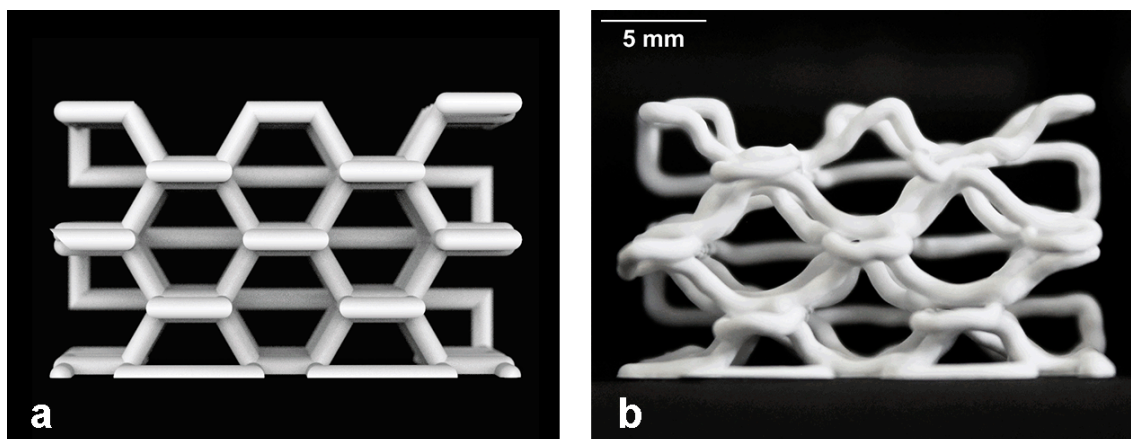


**Figure 2.8.** Comparison between the honeycomb (a) digital model, (b) printed (green state).

The honeycomb shown in here (**Figure 2.8** (b), green state) was printed at  $10 \text{ mm s}^{-1}$ ; it shows a regular structure with good resemblance with the 3D model. The struts have a thickness of  $0.87 \pm 0.06 \text{ mm}$  ( $0.84 \text{ mm}$  in the model); the hexagonal struts, in the front view, form an angle of  $58 \pm 5^\circ$  with the XY plane ( $60^\circ$  in the model). This demonstrates the rapid retention of the filament shape during and after printing. As the flow rate is manually adjusted by changing the extrusion pressure, a perfect matching of the moving speed is not guaranteed; small discrepancies of the printed component from the predetermined 3D model can therefore be detected. More systematic errors in the structure are to be attributed to the directionality of the process. Indeed, the angle between the nozzle and the extrusion direction varies significantly during the print, affecting the interaction between the light and the material to be cured. When the nozzle is moving upwards the semi-hexagon cell, the UV light immediately reaches the filament as it is extruded; the strut quickly cures forming an angle of  $60 \pm 2^\circ$ . On the other hand, when the nozzle moves down to complete the cell, it shadows the extruded filament retarding its curing and causing its partial collapse, resulting in an angle of  $55 \pm 2^\circ$ . The orientation of the extruded filament has been already identified as a critical aspect for the UV-DIW process, influencing the choice of printing parameters such as flow rate, moving speed and UV light intensity [66]. The phenomenon could be attenuated by locally decreasing the moving speed and flow rate, thus increasing the exposure time; however, this is not possible in our current setup. The issue will be later solved (§2.5) by unlocking additional axes, i.e., by coupling hybrid extrusion with robotic AM; this way, the angle between the nozzle and the extrusion direction can be kept constant, resulting in equal irradiation of the filament through the entire print.



### 2.3.2 Heating treatments

As pointed out in other published works on transparent glass components fabricated from photocurable solutions, the slowest, most critical step of the thermal treatment procedure is the debinding stage [107], [110]. Heating rates and holding temperatures must be well tailored in order to favor the complete yet gradual removal of the organics, leaving behind a porous silica skeleton suitable for the densification process.

Specifically for samples containing only small fraction of particles, debinding with slower heating rates are usually preferred over faster ones in order to avoid the dramatic buildup of the pressure inside of the sample, as well as too large temperature gradients [137]. Here, the TGA curve of a HST sample (reported in **Figure 2.9**) served as a basis for the design of the heating profile (**Figure 2.10**).

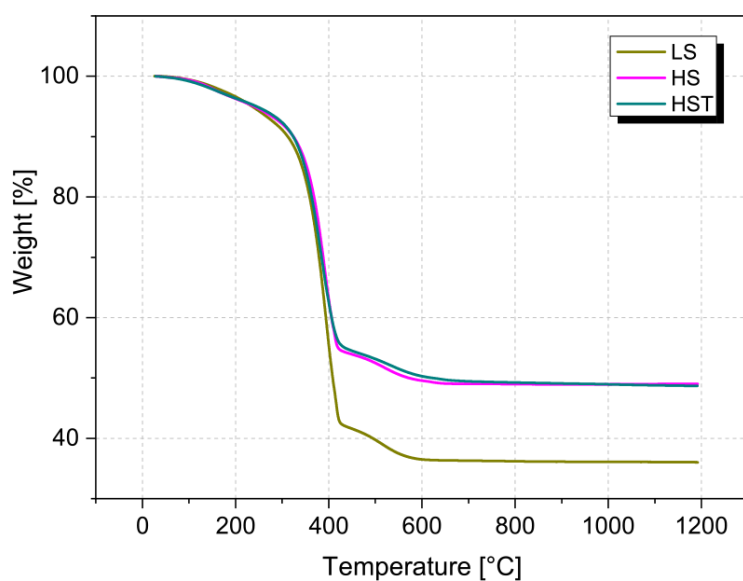


**Figure 2.9.** TGA profiles of LS, HS and HST samples.

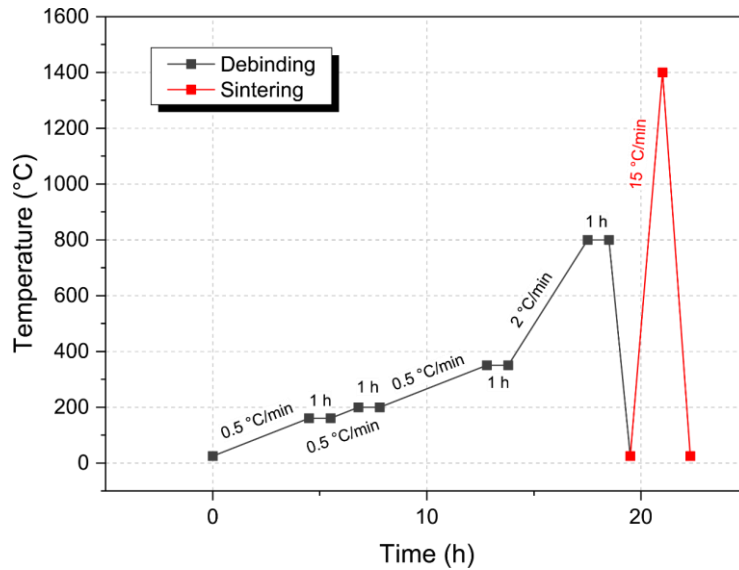


**Figure 2.10.** Optimized debinding and sintering schedule.

The different holding steps account for the condensation of TEOS (160 °C), the decomposition of the acrylates (with maximum mass loss rates at 200 °C and 350 °C) as well as for the removal of -OH groups from the silica particles surface (800 °C) [138]. Debinded samples were further fired up to achieve full densification. In this regard, different works have been demonstrated how nano-silica powders require sintering temperatures of at least 1250 °C to obtain full densification and transparency [112], [118], [139], [140]. On the other hand, temperatures higher than 1450 °C could lead to crystallization to a size that starts to interact with the visible light [112], [141]. The holding time of the sintering schedule also plays a critical role on the final appearance of the glass component: long holding times help on reducing the pore size but could lead to an increase of the crystal size, resulting in translucent or opaque components [142]. A similar crystallization behavior can be achieved by cooling the sintered sample at very slow rate due to the stabilization of the cristobalite phase [143]. Hence, sintering tests were performed by heating HST disc samples at 1400 °C with varying sintering holding times and cooling rates. Specifically, a bottom loading furnace (LHT 01/17 LB Speed, Nabertherm GmbH, Germany) was employed due to the fast opening and descending option of the furnace platform. As it can be seen in **Figure 2.11**, by moving from slower heating schedules to faster ones, crystallization phenomena leading to white cristobalite samples (**Figure 2.12**) can be avoided, thus resulting in an amorphous silica disc (see after).

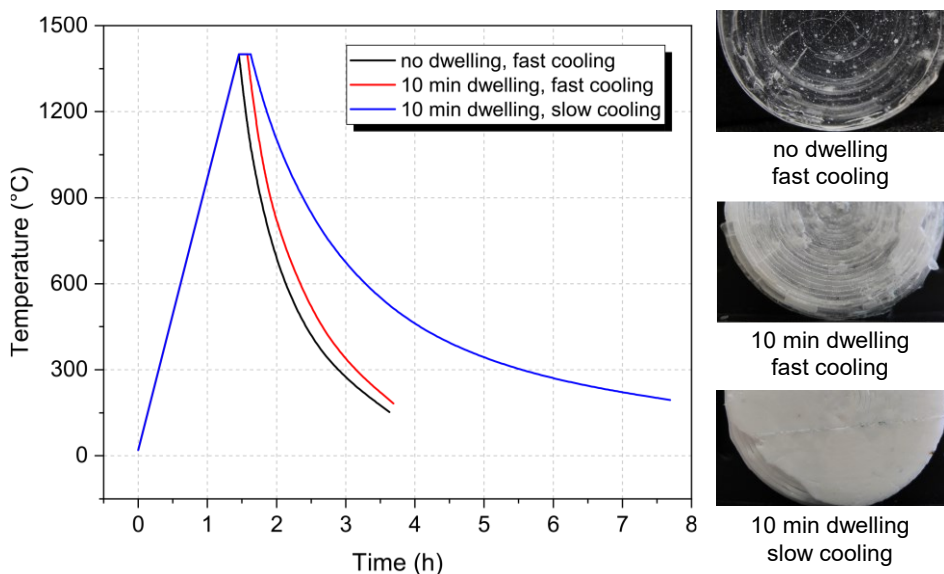


**Figure 2.11.** Effect of the sintering time on the appearance of the sintered sample.

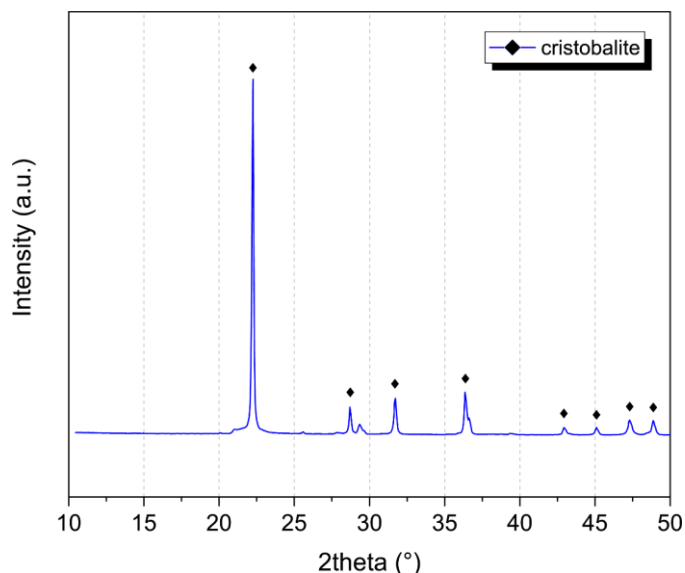


**Figure 2.12.** XRD spectra of the HST sample sintered at 1400 °C for 10 min with slow cooling.

Combining the described debinding and sintering schedules, the resulting time-optimized treatment lasts less than a day, which is remarkably faster (about 180%) than previously published procedures [107], [110]. Only few recent works could employ similar fast heating schedules, which were possible thanks to a much higher particle loading in the starting inks (above 50 wt%) [113], [115], [139]. In turn, preparation of such inks requires time-consuming extra steps for the addition and functionalization of particles, which were not necessary here. In fact, the introduction of TEOS in the HST ink not only allows for a better rheological behavior of

the ink but it also represents a liquid additional source of silica that contributes to the final ceramic yield after sintering, without increasing the particle loading of the ink. Metal alkoxides, including a silicon alkoxide, have been shown to undergo thermally induced condensation before the pyrolysis of the photocurable acrylates, forming a continuous network that remains in the structure after the treatment [108]. Here, TEOS contribution is highlighted by comparing TGA curves performed on LS, HS and HST printed parts (**Figure 2.9**): with 21.0 vol% of particle loading, HST reaches the same ceramic yield of HS, containing 28.2 vol% of particles. The low amount of fumed silica present in the sample alone would not allow to obtain dense, transparent samples with the proposed thermal treatment, as it can clearly be seen from LS sample in **Figure 2.13**; the fast debinding step resulted in extensive cracking of the component. Thermal treatment of the HS sample also did not result in a dense, transparent component, despite the same ceramic yield of HST. This difference can be attributed to the lower temperature required for the sintering of a silica gel from TEOS compared to that of fused silica particles [116]; the presence of residual hydroxyl groups in sol-gel derived silica [144]–[146] could lead to a decrease in the glass viscosity through the depolymerization of its three-dimensional network [147], [148], thereby favoring viscous sintering. For the same reason, TEOS is often employed as sintering aid in the production of transparent Nd:YAG ceramics, promoting densification, elimination of pores and grain growth [149].

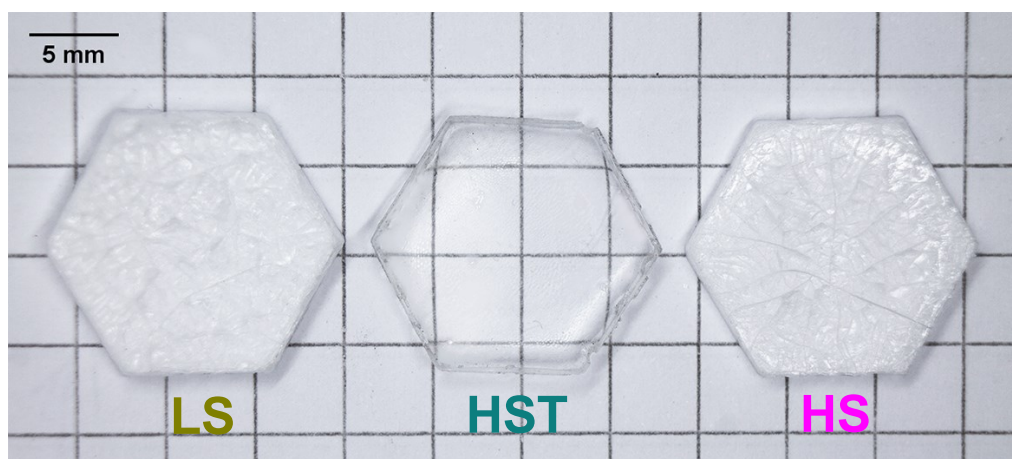


**Figure 2.13.** From left to right: sintered LS, HST and HS components.

The overall linear shrinkage was 28%; the measured bulk density and Vickers hardness were  $2.20 \pm 0.02 \text{ g cm}^{-3}$  and  $488 \pm 9 \text{ HV}$ , respectively, both typical values for dense silica glass (i.e.,  $2.20 \text{ g cm}^{-3}$  and 468–537 HV) [150], [151]. No difference between bulk and apparent density

was measured, indicating that no porosity is present; SEM observation of the fracture surface of a sintered filament (**Figure 2.14**) also shows a dense, homogeneous sample and no residual micro-porosity can be detected. The XRD profile reported in **Figure 2.15** confirms that the material is fully amorphous, and that no crystallization occurs during the thermal treatment.

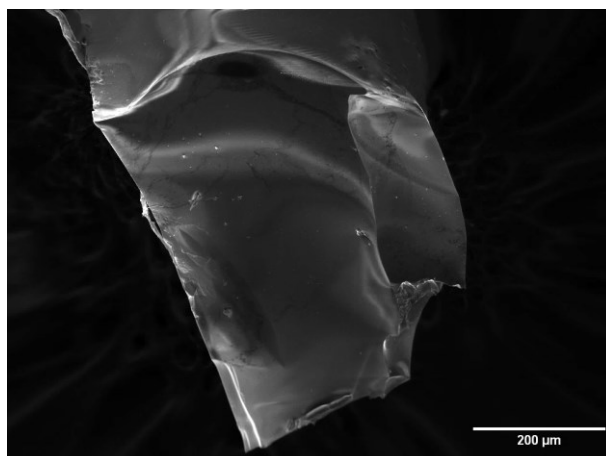


**Figure 2.14.** SEM image of the section of a HST sintered filament.

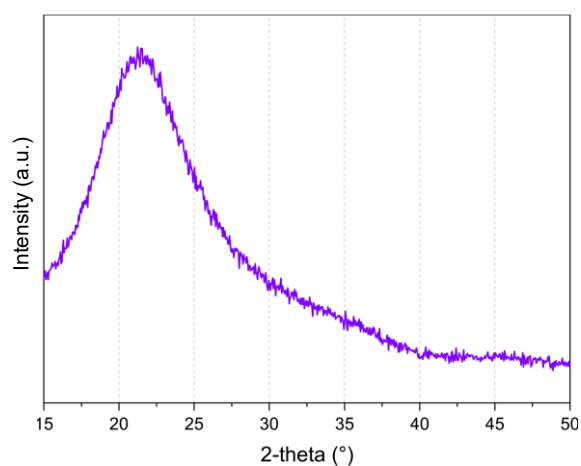


**Figure 2.15.** XRD spectrum of the HST sample.

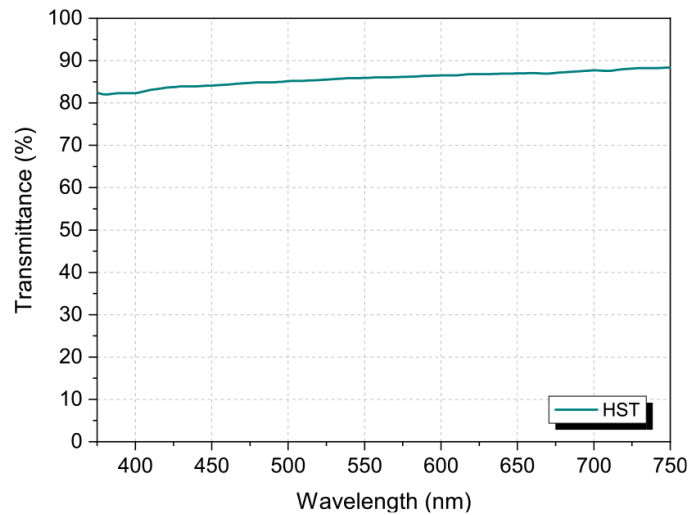


**Figure 2.16.** Transmittance spectrum of an HST component.

The transparency and refractive index of the sintered material was assessed on samples with thickness similar to that of the filaments; the transmittance spectrum in **Figure 2.16** shows a high transparency, with a transmittance of 82–88% in range of the visible light (375–750 nm). These values are comparable with the previously cited literature on the fabrication of glass components from colloidal silica solutions. The measured refractive index at 589 nm was 1.459, corresponding to the theoretic value for silica glass [152].

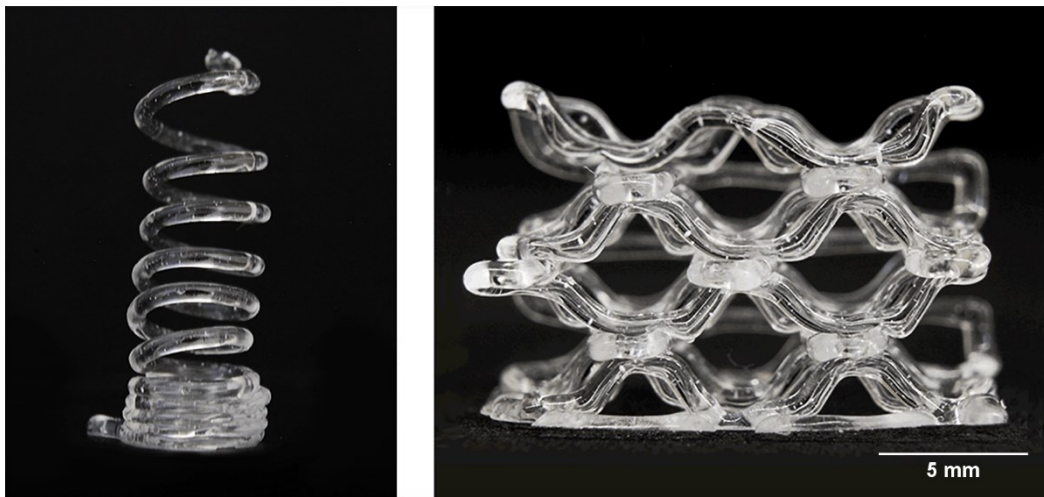


**Figure 2.17.** Sintered coil and honeycomb samples; the scale bar refers to both.

**Figure 2.17** shows the coil and honeycomb components after debinding and sintering. No significant deformation could be detected in the final objects: the struts retained their shape and did not sag even in correspondence of the support-less connections.

### 2.3.3 Multicomponent silica-based ink

The hybrid UV-DIW technology has the potential to produce exciting developments in several fields such as optics, sensors and micro-fluidics. Hence, as a further validation of the system capabilities, the silica-based formulation was modified in order to introduce specific optical properties of the glass component. Indeed, rare-earth oxides have been frequently used to dope and tune the optical and photonic properties of silica glasses [153].

Specifically for this work, a cerium precursor (Ce (III) nitrate hexahydrate (Sigma Aldrich, Germany)) was selected to obtain a multicomponent glass having photoluminescence characteristics. Indeed, Ce-doped glasses are being widely used in photonics for their capacity to tune light signals: thanks to the  $5d \rightarrow 4f$  transitions of  $Ce^{3+}$  ions, when irradiated with UV light, cerium converts it into the visible range ( $\lambda=350$  nm), thus emitting a blue light [115].

The preparation of the multicomponent ink followed the same procedure already described in §2.2. Nonetheless, the introduction of such rare-earth precursor is not trivial: not only it has a different particles size than the silica; its solubility is also limited in non-aqueous systems such as the acrylates. Hence, starting from the optimized HST formulation, different compositions were prepared by dissolving the precursor into POE first, and by adding the rest of the reagents after (**Table 2.3**). However, during the ink formulation, it was evidenced how the introduction of the selected precursor provoked a dramatic decrease of the ink viscosity. In this sense, silica and TEOS percentages were modified with respect to the HST quantity, thus favoring the increase of the ink viscosity and the steric effect around the particles. The TEGDA/HEMA ratio was kept equal to 2.5 in order to guarantee an adequate reactivity of the ink. A final glass composition of  $SiO_2/Ce_2O_3=99.8/0.2$  (in weight) was selected, enough to appreciate photoluminescence [154].

**Table 2.3.** Ce-based ink formulations.

vol%	1	2	3	4
<b>TEOS</b>	34.4	33.9	34.0	33.9
<b>HEMA</b>	11.6	11.4	11.6	11.4
<b>POE</b>	4.4	4.4	4.4	4.4
<b>TEGDA</b>	28.0	28.3	28.1	27.6
<b>Aerosil OX50</b>	21.0	20.8	21.3	22.1
<b>Ce precursor</b>	0.1	0.7	0.1	0.1
<b>Omnirad 819</b>	0.6	0.5	0.6	0.5

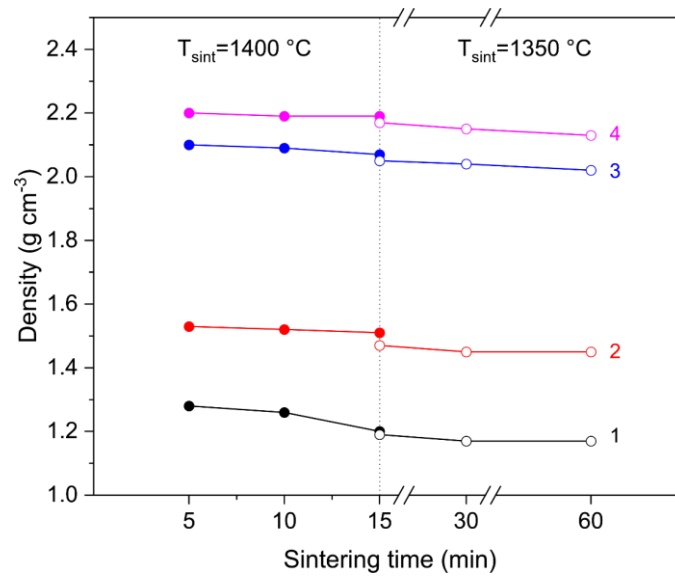


**Figure 2.18.** Ce ink, different sintering temperatures and holding times.

Preliminary tests of sintering schedules were performed on casted and cured samples in the shape of cuboids (10 mm x 10 mm x 2 mm) in order to select the formulation and heating parameters to obtain transparent components. The same debinding schedule reported in §2.3.2 was instead performed on the cured samples; for all sintering schedules, a heating rate of 15 °C min<sup>-1</sup> and a fast cooling rate were used. **Figure 2.18** show the effect holding time on the density of the sintered samples at 1350 °C and 1400 °C.

As it can be noted, both the sintering conditions and the relative quantities of silica and TEOS have an effect on the final density. Specifically, a higher value of density (2.20 g cm<sup>-3</sup> at 1400 °C for 5 min) is reached for inks containing the highest amount of silica particles and the lowest



fraction of TEOS (i.e., composition 4). On the other side, no big variations are reported for different holding times or sintering temperatures at fixed ink composition. This is probably related to the debinding schedule: the higher organic content of composition 1 with respect to composition 4 left bigger pores in its brown state, thus making it more difficult to fully densify the sample. **Figure 2.19** shows the sintered cuboids for the cerium based inks sintered at 1400 °C for 5 min. As it can be noted, the heating schedule parameters leading to the denser sample were optimal also to obtain a transparent, uncracked sample.

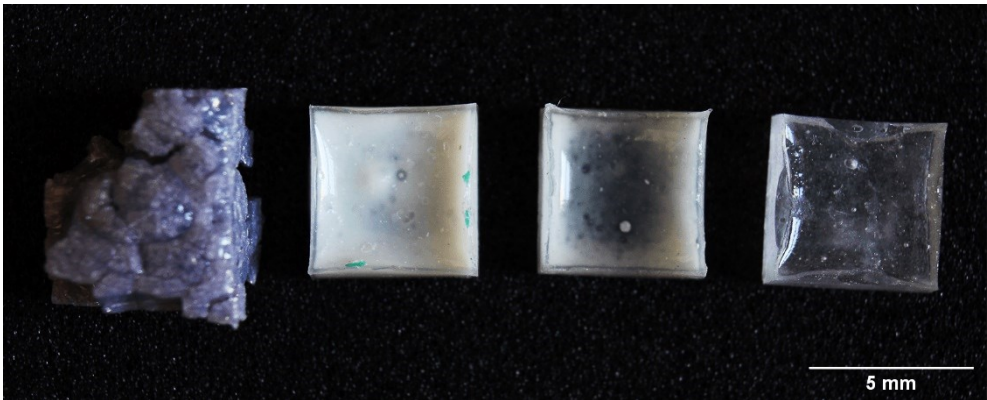


**Figure 2.19.** Sintered cuboid at 1400 °C for 5 min; from left to right Ce-based composition 1 to 4.

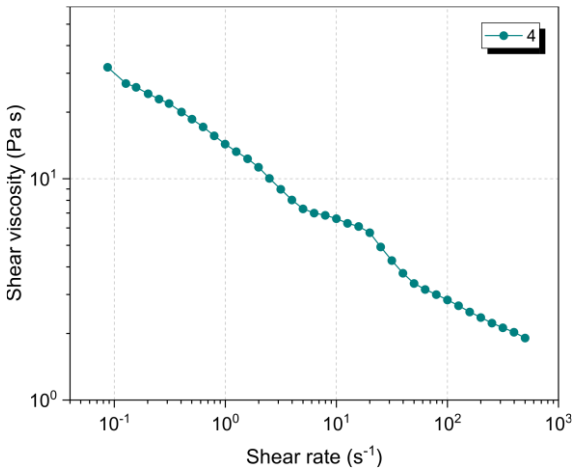


**Figure 2.20.** Viscosity profile of the Ce-based ink.

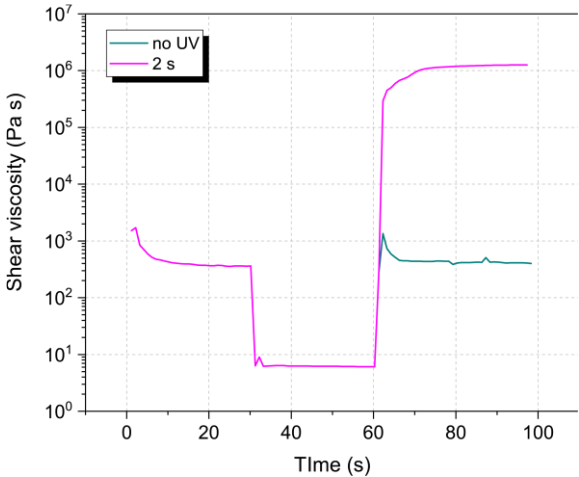


**Figure 2.21.** Three intervals thixotropy test (3ITT) on the Ce-based ink with (2 s) and without UV exposure times.

Compositions 4 of the Ce-based ink was ultimately selected as the optimal one to be further printed with the UV-DIW hybrid setup. Hence, the ink was further tested in order to analyze its

rheological and curing behavior. **Figure 2.20** shows the viscosity profile obtained. As it can be seen, the cerium based formulation possesses a shear-thinning behavior, thus suggesting its printability with the technology (§2.3.1). Indeed, the viscosity profile is similar to the trend previously reported for the mono-component silica-based ink and no thinning-to-thickening switch is displayed. For what concerns the freeform ability of the ink, the three-interval thixotropy test displayed in **Figure 2.21** shows that, even when UV light is not switched on, the ink can rapidly return to its initial viscosity ( $\sim 5 \cdot 10^2$  Pa s): it can be stressed and extruded out of the nozzle and retain its shape when deposited. Nevertheless, if UV light is turned on, it is possible to notice that the ink viscosity increases considerably compared to the first phase ( $\sim 10^6$  Pa s). This means that, by turning on the UV light during printing, the filament solidifies much faster allowing to print self-supporting features. As a proof-of-concept of the combination between the cerium based ink and the technology, a simple, single (thin) wall shape was printed (**Figure 2.22 (a)**). The printed sample (**Figure 2.22 (b)**) shows a good resemblance with the CAD model, thus confirming the high reactivity of the ink.



**Figure 2.22.** Comparison between (a) digital model, (b) printed (green state) and (c) sintered thin wall shape sample.

Sintered samples (1400 °C for 5 min) (**Figure 2.22 (c)**) were tested to analyze their photoluminescence properties. The emission spectra of the doped glass samples were collected using a spectrophotometer (V-570, Jasco, United States). **Figure 2.23** shows a photoluminescence spectrum obtained after excitation at  $\lambda=276$  nm of a  $\text{Ce}^{3+}$  doped glass component. The associated emission profile is centered at  $\lambda=390$  nm, consistent with values previously reported in literature and associated to the emission of a violet-blue light [155], [156].

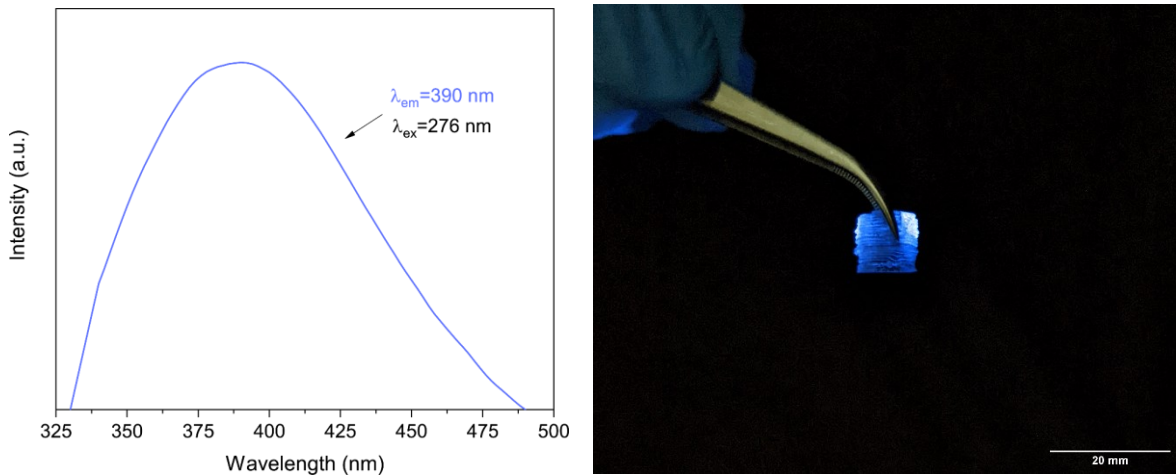


**Figure 2.23.** Emission spectrum of the glass doped with  $\text{Ce}^{3+}$  ions under excitation at 276 nm.

## 2.4 Silicon nitride ink

This work was a continuation of the activity previously started in the framework of the H2020-MSCA-RISE-2016 AMITIE (Additive Manufacturing Initiative and Transnational Innovation in Europe) project. Such research was carried out in collaboration with Kyocera Fin ceramics Precision GmbH (Germany), one of the leading companies in the field of high-performance ceramics, including silicon nitride. Specifically, the shared goal was the development of a photo-curable ink loaded with  $\text{Si}_3\text{N}_4$  particles and the fabrication of components using the UV-DIW technique.

Silicon nitride is a high-performance non-oxide ceramic material of particular interest for structural applications. It has excellent hardness, strength, and thermomechanical properties, as well as chemical inertness, wear resistance and insulation properties [157], [158]; moreover, compared of other advanced ceramics like alumina and zirconia, it possess a lower density and a lower thermal expansion coefficient. Therefore, it is particularly used in machining and bearing applications, automotive engines parts, aerospace components and medical devices [159]–[161]. Nonetheless, such qualities can only be attained if silicon nitride is fully densified: a liquid sintering process is required in order to allow for  $\text{Si}_3\text{N}_4$  to transform its crystal structure from the  $\alpha$  to  $\beta$  phase [162]. Indeed, as reported by Hampshire et al. [163], the fine acicular-

like grain structure of  $\beta$ - $\text{Si}_3\text{N}_4$  possesses a higher flexural strength and crack propagation resistance compared to the  $\alpha$ - $\text{Si}_3\text{N}_4$  one.

This improvement in fracture strength is linked to the relatively high fracture toughness of  $\text{Si}_3\text{N}_4$  which results from the crack deflection and crack bridging mechanisms activating at the interface between the  $\beta$ - $\text{Si}_3\text{N}_4$  acicular grains and the glassy phase resulting from the reaction between the silicon on the surface of  $\text{Si}_3\text{N}_4$  and sintering aids, such as yttria and alumina, which ultimately act as a reinforcement of the matrix. While such liquid phase formation promotes densification at lower sintering temperatures, the application of external pressure is still suggested in order to overcome the low self-diffusivity of  $\text{Si}_3\text{N}_4$  and produce parts with high density. Processes like Hot-Isostatic Pressing (HIP) and Gas Pressure Sintering (GPS) [164], [165], are often employed. It is clear, however, that such techniques cannot provide for silicon nitride parts characterized by high structural complexity: as they require for the homogeneous application of pressure, they are limited to fairly simple geometrical shapes. Although more elaborated components could be obtained by secondary machining steps, frequent tool changing would be needed due to the high hardness of  $\text{Si}_3\text{N}_4$ . Near-net-shape processes like injection molding [166] or gelcasting [167] would need to be coupled with a pressureless sintering step, and would still be constrained to the geometrical complexity of the mold.

In order to overcome the lack of geometrical variety, several AM techniques have been developed for the fabrication of silicon nitride components [168], including SLS, FFF, DIW and DLP. As mentioned previously, SLS relies on the interaction between a powder bed and a laser beam; however, silicon nitride shows a poor absorption of the laser beam energy. Its sintering is quite challenging and often requires post-processing: Qi et al. [169], for example, coupled SLS with Cold-Isostatic Pressing (CIP), whereas Yu et al. [170] showed as a possible solution the infiltration of a  $\text{Si}_3\text{N}_4$ -SiC/ $\text{SiO}_2$  part printed through SLS. Denser and near-net shape  $\text{Si}_3\text{N}_4$  parts can instead be obtained through FFF, as successfully reported by Rangarajan et al. [171]; yet the anisotropic mechanical response of the components could only be attenuated by doping of the FFF filaments with  $\beta$ - $\text{Si}_3\text{N}_4$  seed particles. A similar approach has been also proposed by Jin et al. [172], which took advantage of the shear stresses generated during the DIW process in order to orient the  $\beta$ - $\text{Si}_3\text{N}_4$  grains added into a  $\text{Si}_3\text{N}_4$  based paste, ultimately allowing for the fabrication of fairly isotropic components. Nonetheless, as previously reported, extrusion

techniques like DIW have to stand under strict rheological requirements, thus limiting the complexity of printable shapes.

DLP has also been explored, due to the already stated benefits in terms of printing resolution and building times. However, the light-particle interaction plays a major role here, hindering light penetration and activation of the photocurable moieties [173]. Wang et al. [174] alternatively proposed the fabrication of  $\text{Si}_3\text{N}_4$  complex shapes from the curing and pyrolysis of a preceramic polymer mixture (i.e., polysilazanes). Low mechanical properties could however be achieved due to the poor density of the samples after thermal treatment. Hence, research focused on the formulation of highly dispersed powder-based photocurable slurries and on the increase of the curing depth. Li et al. [175], for example, showed that by oxidizing the surface of  $\text{Si}_3\text{N}_4$  particles, it is possible to decrease the absorbance of the light and, consequently, increase the penetration depth of the slurry. This effect is to be attributed to the formation of  $\text{SiO}_2$  onto the powders surface which lowers the refractive index mismatch with the surrounding photocurable medium. Indeed, a similar approach was presented by Liu et al. [176], which instead modified the silicon nitride particles surface by introducing a silane agent. Nevertheless, up to now, reported maximum curing depths are in the range of 30 to 50  $\mu\text{m}$ , while long exposure times are still required (i.e., 15 s), ultimately limiting the fabrication of  $\text{Si}_3\text{N}_4$  parts using DLP.

Starting from such literature, and following a similar approach to the one described for the silica based ink, different silicon nitride sources have been explored in the present research in order to identify the best way to not only obtain a homogenous and well-dispersed ink, but especially reach high solid loadings (i.e., 50 vol%) [23]. Such feature is highly desirable and yet hard to achieve: the high density and weak Coulomb repulsion forces characterizing the  $\text{Si}_3\text{N}_4$  powders limit its introduction both in water and non-water based suspensions [173], [177]. On the other hand, an inadequate solid loading results in a poorly densified sample after the debinding and sintering schedules required to remove the organic phases and obtain a ceramic component.

In this sense, the research work firstly focused on the investigation of the effect of the manufacturing method on the morphology and distribution of the  $\text{Si}_3\text{N}_4$  particles. For this reason, two different powders were tested, in which the same composition was maintained; the first one was obtained from grinding-and-sieving of a dried suspension, while the second was produced via spray drying process. Both powders were supplied by Kyocera and consisted in  $\text{Si}_3\text{N}_4$  with

$\text{Al}_2\text{O}_3$  and  $\text{Y}_2\text{O}_3$  as sintering aids; exact quality and amounts were not disclosed by the company. Results showed that, while grinding produces a large dimensional distribution of irregular shaped particles, spray drying allows to obtain a narrower distribution of spherical particles [178]. Aiming to increase the reproducibility of the ink, spray dried particles ( $\phi \sim 50 \mu\text{m}$ ) were firstly used.

In order to promote and facilitate the creation of a strong polymer network in the ink upon curing, trimethylolpropane triacrylate (TMPTA) was selected: due to its higher number of vinyl groups with respect to HEMA and TEGDA, the curing mechanism should more easily compete against the absorption of the light by the dark  $\text{Si}_3\text{N}_4$  particles [124], [179]. In addition to that, POE was chosen as further solvent of the system. As previously described in §2.2, it is not possible to match exactly the refractive index of  $\text{Si}_3\text{N}_4$  with the one of acrylates.

**Table 2.4** shows the final ink with spray drying silicon nitride particles which was mixed using the procedure explained in §2.2. As shown in **Figure 2.24**, the viscosity profile of the ink obtained displays a shear-thinning behavior in the observed shear rate range ( $0.1\text{-}200 \text{ s}^{-1}$ ), making it theoretically suitable for printing with the UV-DIW technology. Nonetheless, the printing test failed: frequent nozzle clogging and adaptation of the printing parameters (i.e., pressure and printing speed) were experienced. Indeed, such phenomena were attributed to the absence of either electro-chemical or steric interaction between the particles and the liquid phase, leading to a poor dispersion of the particles inside of the ink and, consequently, to their agglomeration at the nozzle end. Moreover, the mono-dimensional distribution of the spray drying particles lowers their packing inside of the ink, thus decreasing the amount of silicon nitride that can be added and consequently the density of the printed component after the heating schedules. This effect is accentuated by the presence of “cup-like” hollow spheres within the powder (visible with SEM analysis), that subtract solvent from the system by absorbing it into their cavities.

**Table 2.4.** Silicon nitride-based ink formulation using spray drying powders.

	wt%	vol%
Si <sub>3</sub> N <sub>4</sub> spray drying powder	69.8	44.5
TMPTA	21.2	39.0
POE	9.0	16.5

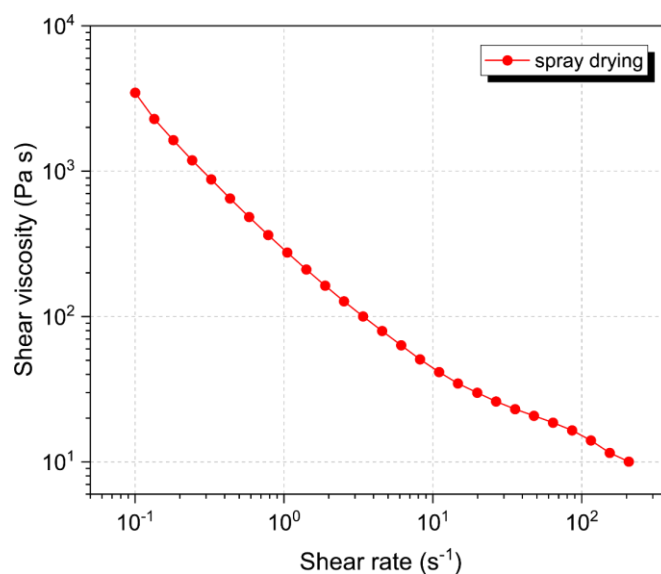


**Figure 2.24.** Viscosity profile of the silicon nitride ink with spray drying powders.

Therefore, in order to optimize the dispersion of the particles inside the ink, maximize the solid loading and obtain a continuous flow of the ink out of the nozzle during the printing process, the ink design strategy was modified. First of all, the spray drying particles were discarded and the ones obtained from the grinding-and-sieving method were instead employed. A silane coupling agent was also introduced in the starting suspension, which is adsorbed on the surface of silicon nitride particles and keeps them separate through steric hindrance. Indeed, Liu et al. [176], demonstrated that 3-glycidyloxypropyl trimethoxy silane (GLYMO) decreases the overall viscosity of the Si<sub>3</sub>N<sub>4</sub> based ink by increasing the particles dispersion thanks to the chemical adsorption of GLYMO onto the particle surfaces. Following their experimental procedure, 1 wt% of silane (with respect to the powder) was mixed together with silicon nitride particles by ball milling at 350 rpm for 6 h, using ethanol as the milling medium. Once dried, the powder was grinded again, this time without solvent, in order to further reduce the particle size and break down any agglomerate that might have formed; finally, the obtained surface-modified silicon nitride particles were sieved. As previously pointed out, a wider dimensional

distribution is preferred in order to optimize the packing of the system and, consequently, to maximize the solid loading of the ink. For this reason, three different ranges of particle diameters were isolated through sieving (36-63  $\mu\text{m}$ , 63-75  $\mu\text{m}$ , 75-90  $\mu\text{m}$ ), and then mixed following the Bolomey equation [180] used in the concrete design:

$$P_d = \frac{A - B + (100 - A)\sqrt{\frac{d}{D}}}{100 - B} \cdot 100 \quad (6)$$

where  $P_d$  is the percentage of particles passing through the  $d$ -sieve opening,  $D$  is the maximum particle size (i.e., the biggest sieve opening),  $B$  is the percentage of colloidal particles and  $A$  is the empirical coefficient depending on the slump of the concrete and type of aggregates. Specifically, typical values of  $A$  ranges from 8 (low slump) to 14 (high slump) [180]; in the present work,  $A$  was set equal to 10, considering the crushed nature of the silicon nitride powder as well as its coating with GLYMO that promotes a higher slump;  $B$  was set equal to 0 due to the absence of colloidal particles. **Figure 2.25** reports the  $P$  values obtained by fitting (6) in the particles size range 36-90  $\mu\text{m}$ .  $P_{63}$ ,  $P_{75}$  and  $P_{90}$  are also highlighted: their relative difference gives the optimal wt% for each of the three sieving range, as reported in **Table 2.5**.

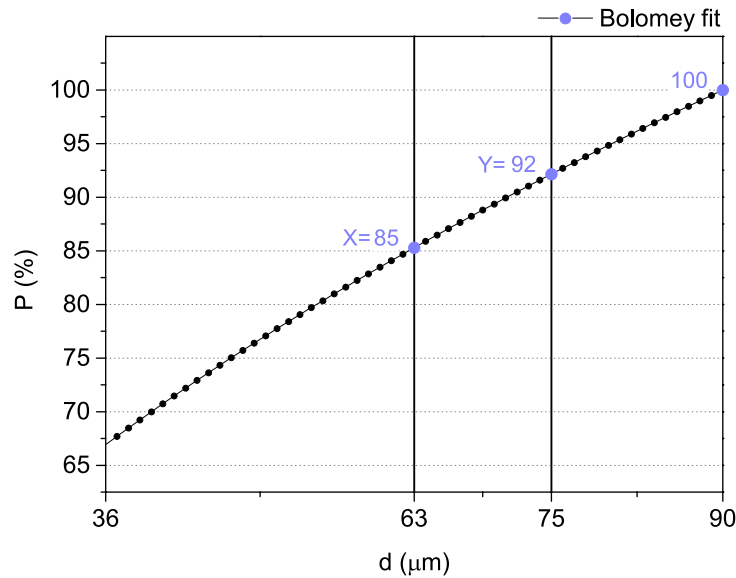


**Figure 2.25.** Fitting of the Bolomey equation over the particles size range analyzed.



**Table 2.5.** Optimal wt% for each of the three sieving range.

Particles range	36-63 $\mu\text{m}$	63-75 $\mu\text{m}$	75-90 $\mu\text{m}$
wt%	85	7	8

**Figure 2.26** (a) shows the viscosity profile of the optimized ink compared to the one using spray drying particles, both characterized by the same final composition (reported in **Table 2.4**). As it can be noticed, the new ink design strategy helped on decreasing the viscosity particularly in the lower shear rates region, while promoting a shear-thinning behavior of the ink. At higher shear rates corresponding to the typical shear rates range of the UV-DIW printing process (reported in §2.3), the optimized ink showed a slightly lower viscosity yet similar trend compared to the spray drying one. When the silicon nitride content increases up to 50 vol% (**Figure 2.26** (b)), the same shear-thinning behavior is observed; the modification of the  $\text{Si}_3\text{N}_4$  particles surface and the optimization of the particles size distribution therefore allow to prepare a high loaded yet low viscous mixture, where particles collision and agglomeration are effectively avoided. This result was confirmed by the printing tests: no clogging was experienced and a continuous and homogenous flow of the ink out of the nozzle could be maintained. The final ink composition used for the freeform printing is reported in **Table 2.6**.

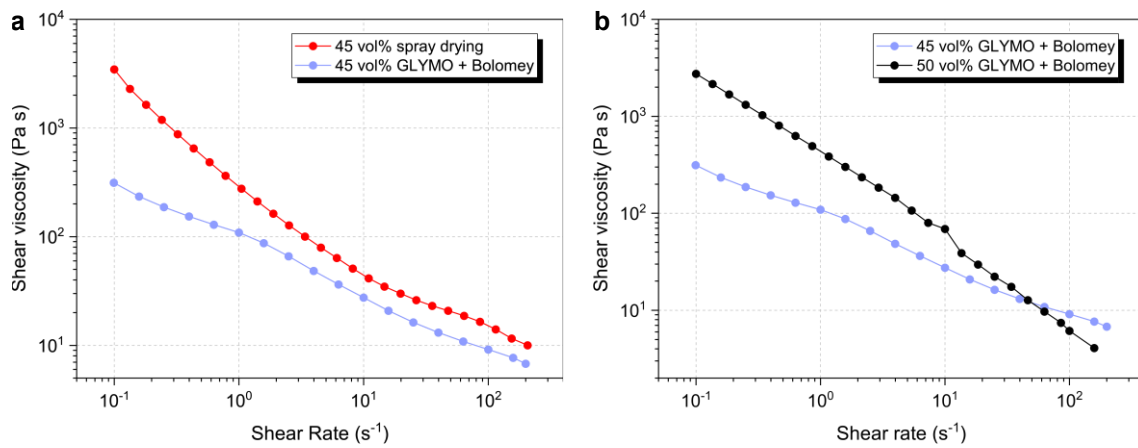


**Figure 2.26.** (a) effect of the  $\text{Si}_3\text{N}_4$  surface modification and particles size distribution optimization on the viscosity profile of the ink; (b) effect of the silicon nitride content on the viscosity profile.

**Table 2.6.** Silicon nitride based ink composition using modified and size distribution optimized particles.

	<b>wt%</b>	<b>vol%</b>
Si <sub>3</sub> N <sub>4</sub> – GLYMO (Bolomey)	74.2	50.0
TMPTA	18.5	35.9
POE	7.3	14.1

### 2.4.1 Printing and freeform ability

The development of a silicon nitride ink suitable for the UV-DIW technology is set to further validate the hypotheses set for the process. In fact, most of the literature on the DLP of Si<sub>3</sub>N<sub>4</sub> components reports really poor curing depth caused by the RI mismatch [173], [174], [179]. Indeed, the freeform ability of the hybrid system has so far been demonstrated only for the silica ink which, thanks to the RI matching between SiO<sub>2</sub> and the acrylates, can easily be cured and allows for a fast shape retention. In addition to that, it should be considered that due to their grey color, silicon nitride particles have a larger absorbance value compared to lighter particles (i.e., silica), thus negatively affecting the curing behavior [181].

Therefore, the hybrid setup was modified: as shown in **Figure 2.27**, it was updated with an array of 15 UV diodes (UV5TZ-400-15, Bivar Inc., USA) attached to a custom printed circuit board (PCB), powered with a 24 V – 10 A power supply unit and with an intensity of 70 mW cm<sup>-2</sup> at the point of extrusion. It should be also pointed out that the new add-on was optimized in term of its incumbrance, thus designed to have a more compact housing for the LEDs and connected directly to the syringe. Indeed, it came clear along the research work that the previous design (**Figure 2.1**) did not allow for the fabrication of large and/or porous structures having long spanning features without the collision with the LEDs array.

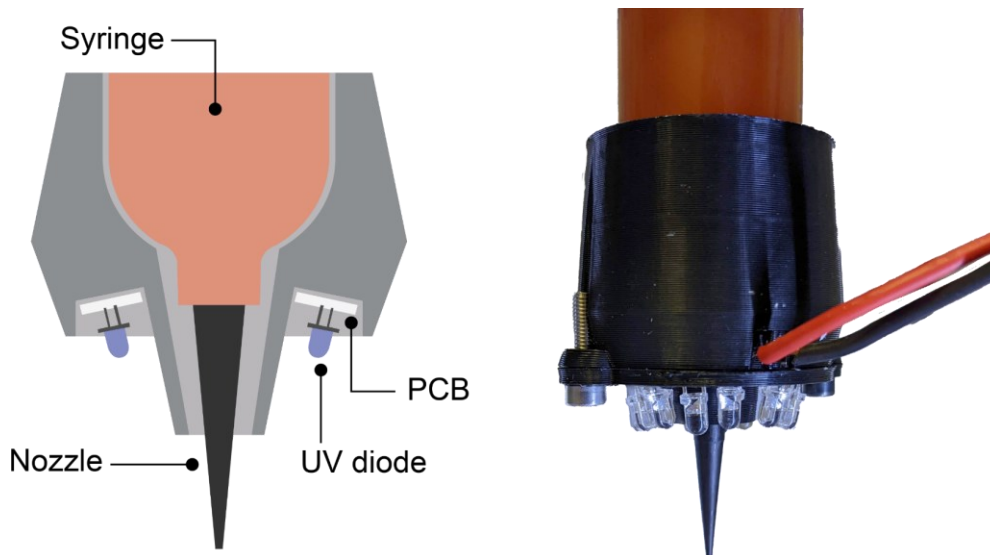


**Figure 2.27.** Schematic of the modified hybrid setup with UV diodes (left) and mounted over the delta printer head (right) .

In order to verify the influence such RI mismatch on the freeform ability of the UV-DIW technology, the curing depth of the silicon nitride ink was firstly measured. **Figure 2.28 (a)** reports the experimental values of curing depth as function of exposure time using a light intensity of  $I=70 \text{ mW cm}^{-2}$ . The first thing to notice is that all reported curing depth values are fairly higher when compared to the one reported in literature for similar  $\text{Si}_3\text{N}_4$  volume concentrations [62], [173], [182]. Indeed, this can be attributed to the introduction of GLYMO: while on one end the polymer chain is adsorbed on the particle surface, on the other chain end the epoxy group reacts with the acrylate, creating a bridge that lowers the  $Q$  parameter in **(1)**, consequently increasing the curing depth [176]. Moreover, as expected, increased curing times result in increased cured thicknesses, yet two distinct plateaus in the curing depth –  $60 \mu\text{m}$  for  $t < 1 \text{ s}$  and  $100 \mu\text{m}$  for  $t > 5 \text{ s}$  – can be seen, suggesting a non-linear correlation and limiting the use of the Jacobs equation (**(5)** in §2.3.1) for predicting the characteristic curing values for the ink. Similar considerations were reported by Shen et al. [183], Li et al. [184] and Chartier et al. [185], which attributed such plateaus to a secondary monomer-to-polymer conversion process promoted by the light scattering. Specifically, they suggest that even if UV light does not penetrate below a certain depth, a further exposure of the cured layer can lead to a decaying of the light which extends the polymerization to the un-cured part of the ink [186]. The phenomenon depends not only on the amount of un-reacted monomers present underneath the polymerized layer, but especially on the energy dose. This was indeed verified by measuring the evolution

of the curing depth as a function of the light intensity for two different exposure times. As shown in **Figure 2.28** (b), a higher curing depth (150  $\mu\text{m}$ ) compared to the ones previously reported could be reached only after 5 s of exposure at 270  $\text{mW cm}^{-2}$ .

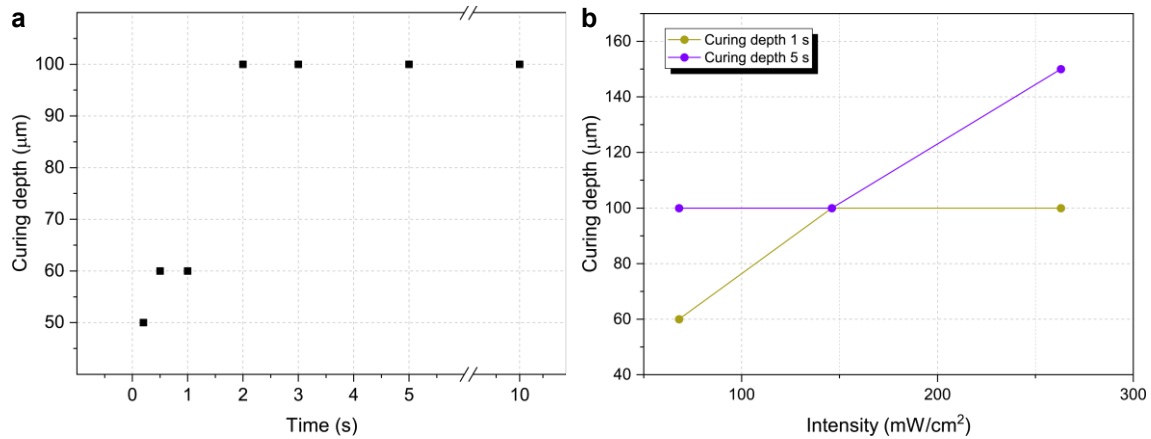


**Figure 2.28.** Curing depth of the silicon nitride ink as a function of (a) exposure energy density (logarithmic scale) and (b) UV light intensity; 1 s (orange line) and 5 s (purple line).

As shown before for low transmittance, a low curing depth of the ink does not influence the free-standing ability of the process (§2.3.1). Indeed, the hybrid UV-DIW technique does not require for a full cure of the extruded filament in order to guarantee its shape retention; the polymerization of the outer skin does suffice. In order to assess the effect of the exposure intensity on the viscosity behavior of the  $\text{Si}_3\text{N}_4$  ink when cured, the 3ITT test was performed using the same parameters reported in §2.3.1, while the UV lamp was switched on for 1 s and set at 70  $\text{mW cm}^{-2}$ , 150  $\text{mW cm}^{-2}$  and 270  $\text{mW cm}^{-2}$ . As shown in **Figure 2.29**, if the UV light is not switched on during the third interval, the ink shows a strong thixotropic tendency by slowly recovering its initial viscosity value ( $\sim 10^3$  Pa s) only after 40 s. Contrary to the silica ink, this behavior is more consistent with the one conventionally reported for DIW inks [187] and it is probably linked to the higher particles dimensions and liquid-particle interactions. When the UV light is switched on, the viscosity profile gradually increases as the light intensity increases: since the exposure time was kept constant, the higher the UV intensity, the quicker the energy dose overcomes the critical energy required for the polymerization [186]. Nonetheless, the initial viscosity of the ink is reached and exceeded almost instantly for all tested UV intensities, thus suggesting that a UV LEDs array with an intensity of 70  $\text{mW cm}^{-2}$  could be enough to ensure the freeform ability of the system.

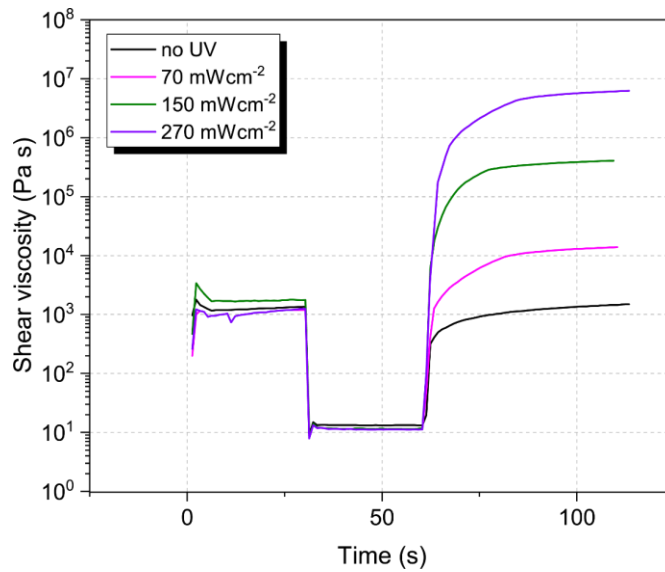


**Figure 2.29.** Three intervals thixotropy test (3ITT) on the  $\text{Si}_3\text{N}_4$ -based ink with different UV exposure intensities.

The new setup allowed for the printing of the support-less and freeform geometries shown in **Figure 2.30** and following. **Figure 2.30** (a) shows the coil design – previously printed with the silica based ink and reported in **Figure 2.7** (a) – printed at  $5 \text{ mm s}^{-1}$  with a nozzle of  $0.58 \text{ mm}$  and at a pressure of  $1 \text{ bar}$ . There is a better correspondence to the model than that achieved with the silica ink: less sagging, a more controlled helical structure and pitches of similar length to the ones designed. The measured thickness of the extruded filament was  $0.58 \pm 0.04 \text{ mm}$ , thus confirming an optimal combination of printing speed with extrusion pressure. Indeed, the freeform ability of the ink is therefore validated.

The cross-section of the extruded and cured filament reported in **Figure 2.30** (b) reveals the presence of an outer skin with a thickness that corresponds to the measured curing depth. Its non-uniform thickness is to be correlated to the printing direction and especially to the position of the UV light. Particularly, this depends on the top-down projection of the UV light emitted by the diodes: while the upper part of the filament is constantly irradiated through the printing path, the bottom surface can only cure thanks to the scattered and/or reflected light. Hence, the curing depth on the bottom of the filament will be lower than the one on the top, as also recently pointed out by Clarkson et al. [62]. This indeed demonstrates that the curing depth is not a limiting factor for the UV-DIW technique, while it is the rapid reaction to UV light exposure to represent the critical parameter.

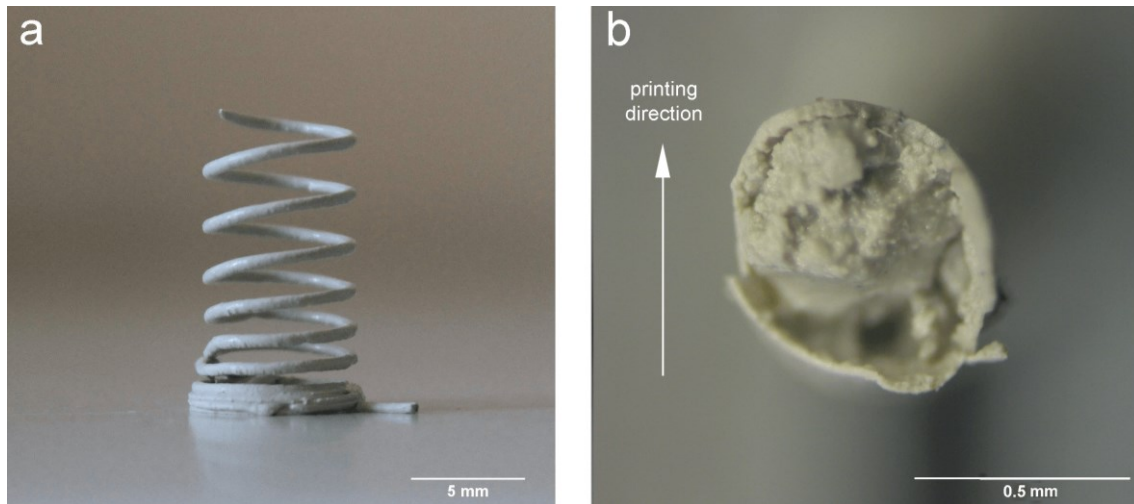


**Figure 2.30.** (a) coil structure printed with the silicon nitride-based ink and (b) a cross-section of the extruded and cured filament.

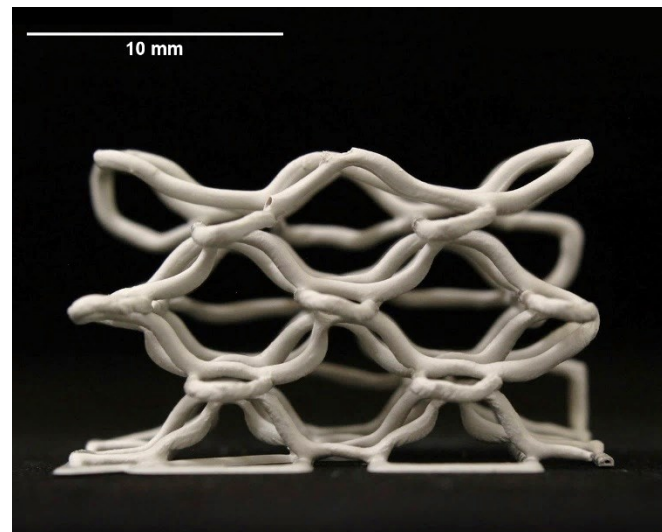


**Figure 2.31.** Honeycomb structure printed (green state) with the silicon nitride-based ink.

The honeycomb-like structure was again selected to verify the freeform ability of the ink. **Figure 2.31** shows the obtained component (printed at  $5 \text{ mm s}^{-1}$ ); considering the CAD model in **Figure 2.7 (a)**, geometrical discrepancies similar to those described in §2.3.1 can be detected. Specifically, the designed  $60^\circ$  angle of the semi-hexagon shape gradually decreases from the bottom to the top of the structure, varying from  $60 \pm 1^\circ$  to  $44 \pm 1^\circ$ . This wide range of values can be attributed to the non-homogenous curing of the cross-section which leads to increased sagging of the filament on the bottom due to the progressive movement in the Z direction. Additionally, the unavoidable directionality of the printing process due to the locked position

of the printing head with respect to the printing path can be detected (§2.3.1): inclined trusses being printed while the nozzle moves up or down present different angles (i.e.,  $60 \pm 1^\circ$  and  $40 \pm 1^\circ$ , respectively, in the bottom of the honeycomb).

While in the next section (§2.5) an advancement of the hybrid technology will be described specifically aiming to overcome the limited freedom of the printing head, it is clear that the combination between the  $\text{Si}_3\text{N}_4$  ink and the UV-DIW process shows great potential. Complex and mechanically efficient lattices, like octahedron, tetrahedron or pyramidal structures could be fabricated, which maximize the strength-to-weight ratio (see §2.5.2). Indeed, the mechanical properties of silicon nitride could be coupled together with the enhanced mechanical response and energy absorption property of the structure itself [188]. As a proof-of-concept, a lattice-beam structure has been designed (**Figure 2.32** (a)) having dimensions  $30 \times 10 \times 10 \text{ mm}^3$  ( $l \times 2h \times w$ ), a total porosity of 95%, and resulting from the repetition and stacking of a pyramidal unit cell ( $h \times l$ ) with a strut thickness of 0.84 mm. The component shown in here (**Figure 2.32** (b)) was printed at  $15 \text{ mm s}^{-1}$  with an extrusion pressure of 1 bar; as it can be noted, there is a good resemblance with the CAD model. The thickness of the filament is of  $0.86 \pm 0.06 \text{ mm}$  while the angle formed by the inclined trusses is of  $44 \pm 1^\circ$  ( $45^\circ$  in the model) independently to the relative movement of the nozzle during its extrusion. Such improvement on the shape retention of the truss could be attributed to the lower overhanging angle compared to the one of the honeycomb structures, thus favoring its freeform ability. Moreover, no distortions can be noted in both the horizontal trusses and the vertical one added to connect the up-sided pyramids.

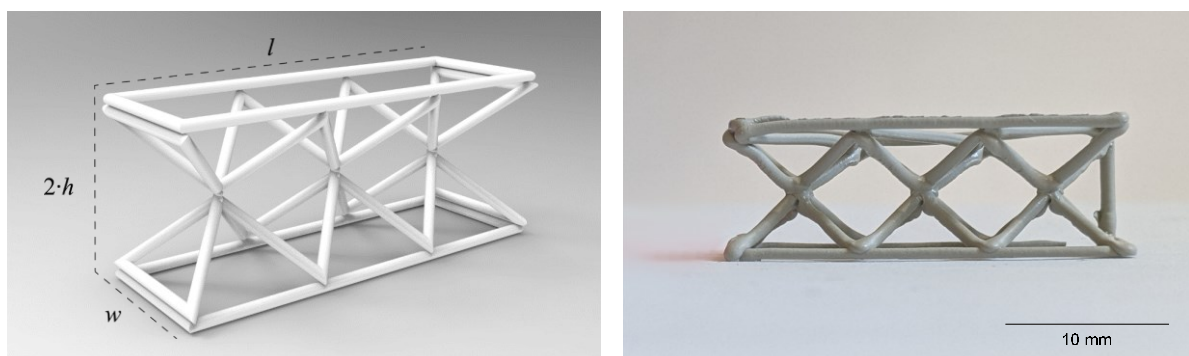


**Figure 2.32.** Comparison between the truss-made beam (a) digital model, (b) printed (green state).

## 2.4.2 Lattice structures characterization

After printing, debinding and sintering treatments were performed to remove the organic phase (TMPTA, POE) and reach complete densification. As stated above, the post treatment of green samples is the most critical step in the fabrication of ceramic components starting from photocurable suspensions [189], [190]. In order to optimize the heating profile, the TGA curve of the silicon nitride ink was taken as reference (**Figure 2.33**). As confirmed by the peaks in the derivative curve, the total weight loss (25.8 %) of the sample can be divided in three steps. Specifically, the first peak at 160 °C corresponds to the evaporation of POE, while the further loss in weight (~ 16%) starting at 350 °C can be attributed to the removal of TMPTA [191].

Therefore, the heating treatment was scheduled as follows: an initial pyrolysis step was performed in air and consisted in 1 h at 120 °C with a heating rate of 1 °C min<sup>-1</sup> up to 120 °C, 1 h at 400 °C with a heating rate of 0.15 °C min<sup>-1</sup> up to 400 °C and 1 h at 560 °C with a heating rate of 0.05 °C min<sup>-1</sup> up to 560 °C. After pyrolysis, brown samples were sintered at a temperature of 1780 °C with a holding time of 2.5 h in nitrogen atmosphere.

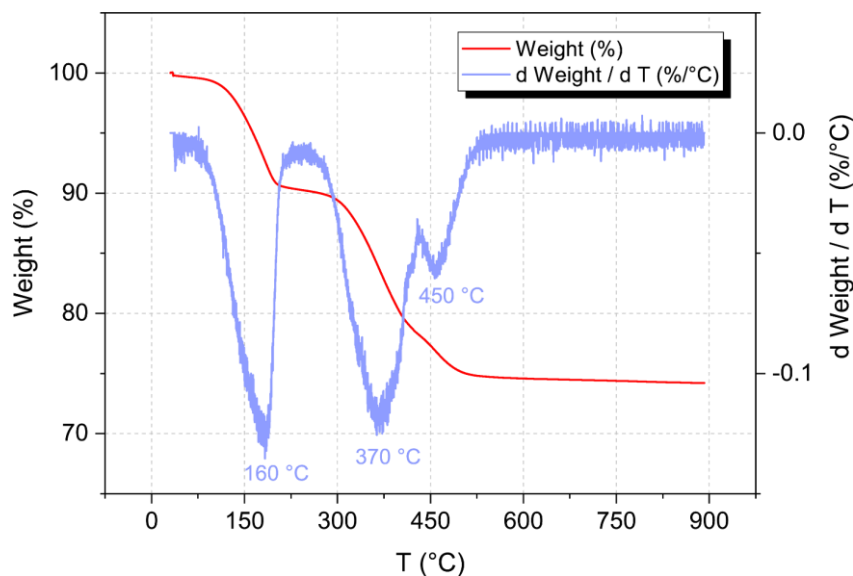


**Figure 2.33.** Thermogravimetric curve (TGA) and 1<sup>st</sup> derivative curve of TGA of the silicon nitride ink.

**Figure 2.34** shows the beam structure after sintering, evidencing no sagging or deformation of the trusses. Density and open porosity of the component were calculated according to the Archimedes principle. The values (reported in **Table 2.7**) were obtained from measuring 6



different samples weight in dry, suspended, and soaked conditions [192]. The measured apparent density is of  $2.90 \pm 0.04 \text{ g cm}^{-3}$ , which correspond to a relative density of 91% with respect to typical values for silicon nitride (i.e.,  $3.2 \text{ g cm}^{-3}$ ). This can be attributed to the limited curing depth of the silicon nitride ink: as showed in **Figure 2.30** (b), only a small fraction of filament cross-section actually cures during the printing process, thus leaving the core part of the truss still with un-reacted monomers. During the debinding schedule the residual photoinitiator can act as a thermal initiator, thus leading to polymerization of the residual monomers in the core part of the truss [190]. In this way, additional heat is generated (the reaction is exothermic), causing a local increase in the temperature and the subsequent higher decomposition rate of the inner part with respect to the outer shell. As a result, the gasses from the degradation of the monomers remain blocked inside of the cured skin, thus leading to enclosed porosities which cannot be later closed during sintering. This was further confirmed by analyzing the cross-section of a sintered filament through SEM analysis: as reported in **Figure 2.35**, a discrete gradient of porosity is visible by moving from the (dense) skin of the filament to the (more porous) center, thus proving the inhibited gas release in the un-cured part.

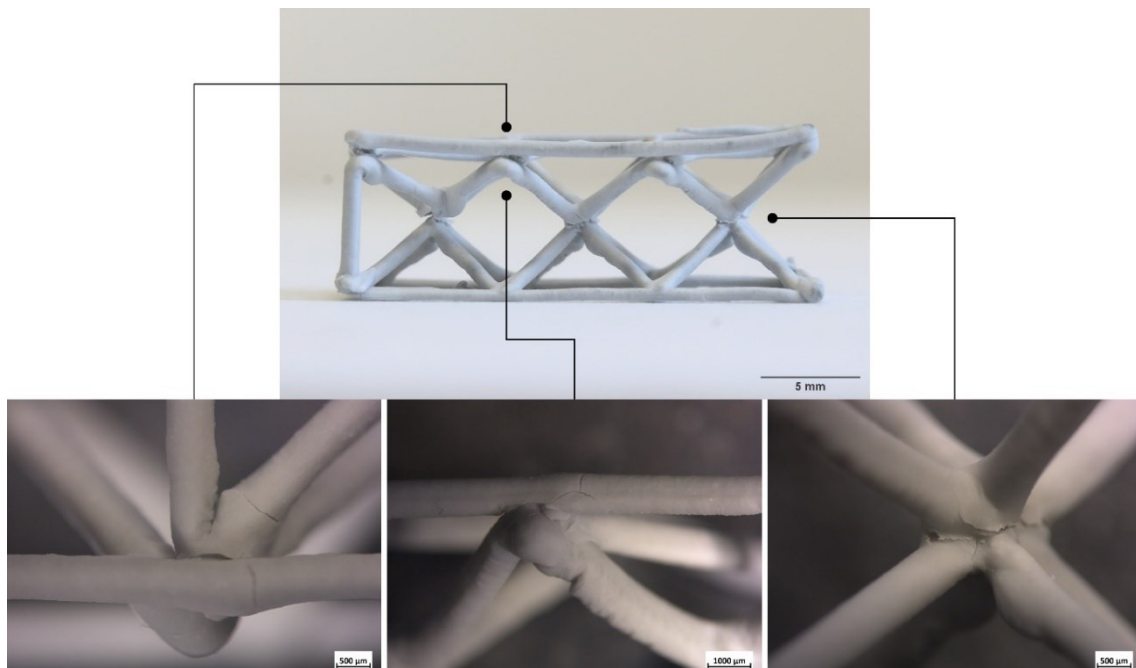


**Figure 2.34.** Truss-made beam structure after sintering (up); magnification of the cracks in 3 different points (bottom).

**Table 2.7.** Density, porosity, mass loss, and shrinkage of sintered silicon nitride components.

<b>Bulk density (g cm<sup>-3</sup>)</b>	<b>Apparent density (g cm<sup>-3</sup>)</b>	<b>Mass loss (%)</b>	<b>Volumetric shrinkage (%)</b>
2.70 ± 0.02	2.90 ± 0.04	29.35 ± 0.01	49.07 ± 7.83

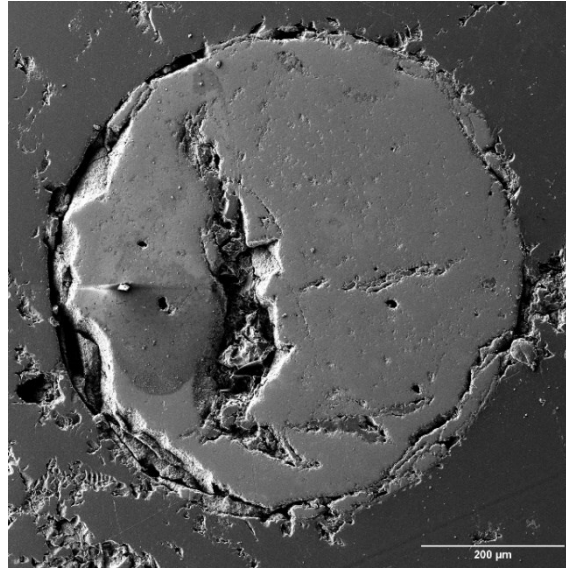


**Figure 2.35.** SEM image of the cross-section of a sintered filament, embedded in resin.

Additionally, differences between the bulk and apparent density (**Table 2.7**) suggest the presence of open porosities. This was confirmed by analyzing the morphology of the sintered samples using an optical stereomicroscopy (AxioCam ERc 5 s Microscope Camera, Carl Zeiss Microscopy, Thornwood, USA). As reported in **Figure 2.34**, cracks formed in different part of the structure, particularly in correspondence of the connection points between trusses. Indeed, this could be associated to the densification process during the sintering phase: since the geometry is constrained, the stresses generated during the sintering step and shrinkage of the sample will create a differential stress status between the nodes and the trusses, thus leading to the cracks. Moreover, it should be pointed out that Si<sub>3</sub>N<sub>4</sub> particles and the glassy phase formed by the sintering aids (i.e., Al<sub>2</sub>O<sub>3</sub> and Y<sub>2</sub>O<sub>3</sub>) represent the only contribution to the final ceramic yield; in this sense, no additional source is able to compensate for the high volumetric shrinkage (i.e., 49.07 ± 7.83 %), leading in this way to the formation of defects. A possible solution to this problem could be the one proposed by Clarkson et al. [62], which introduced a carbon-rich SiC forming preceramic polymer in a silicon nitride suspension: thanks to its excellent ceramic

conversion, lower shrinkage and higher ceramic yield can be reached, ultimately resulting in a 99% relative density after sintering.

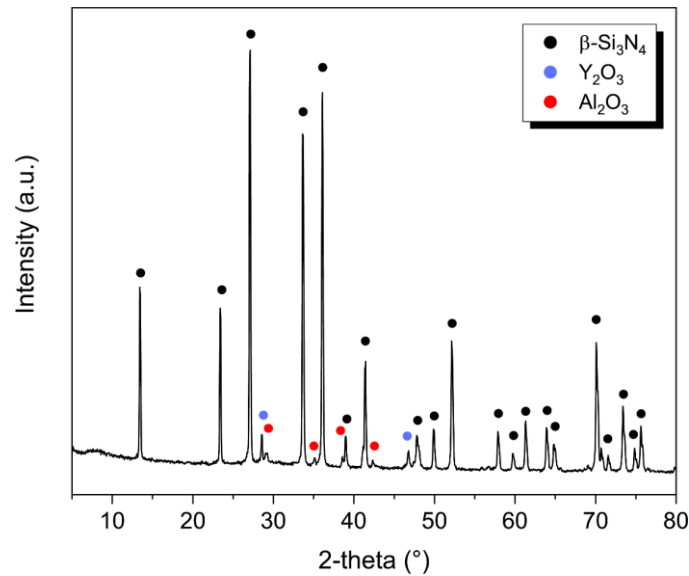


**Figure 2.36.** XRD profile of sintered silicon nitride sample.

The XRD profile of the sintered sample reported in **Figure 2.36** shows the presence of  $\beta\text{-Si}_3\text{N}_4$ ,  $\text{Y}_2\text{O}_3$  and  $\text{Al}_2\text{O}_3$  phases, resulting from the precipitation and dissolution of the  $\alpha$ -phase in a glassy matrix filled with acicular grains [193]. Indeed, the sintering process of silicon nitride is a liquid-sintering process which is driven by the presence and reaction between the sintering aids (i.e., yttrium and alumina oxides) with the silicon oxide present on the surface of the silicon nitride particles [194]. Such interaction creates a liquid phase which coats the  $\beta\text{-Si}_3\text{N}_4$  grains and remains as secondary phase after sintering, as confirmed by the SEM image shown in **Figure 2.37**.

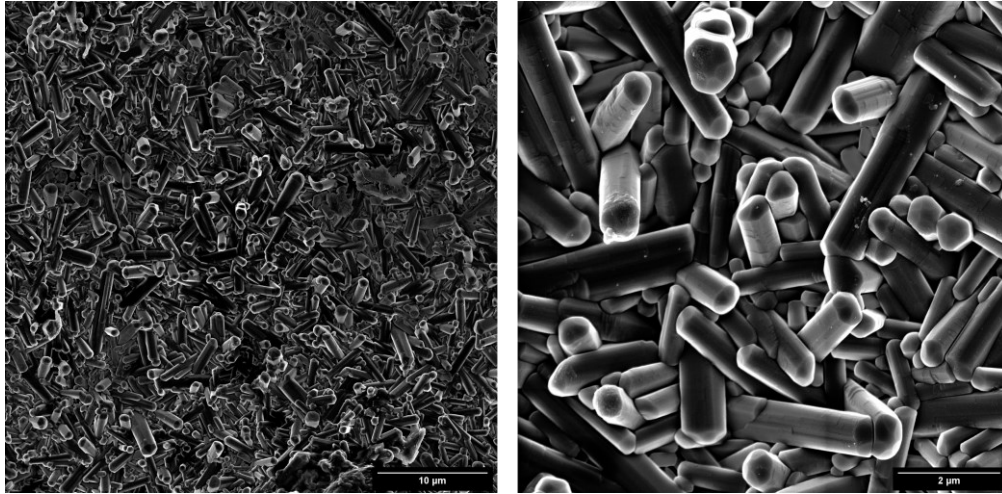


**Figure 2.37.** SEM images of the surface of a sintered filament at 15'000 X (left) and 72'500 X (right).

Finally, with the aim to address the mechanical properties of such structures through flexural testing, a new lattice-beam structure was designed with dimensions (after sintering and consequent volumetric shrinkage measured from sintered samples from preliminary tests, see §2.4.2) according to the normative EN 843-1:2006 [195]. In order for the applied loading to be homogeneously distributed in all struts, the beam was designed with a zig-zag pattern similar to what proposed by Warren et al. for the construction of suspended truss-made bridges [196]; its nominal dimensions (following the schematics in **Figure 2.32** (a)) are  $l = h = 8$  mm and  $w = 82$  mm and its overall porosity is 72%. **Figure 2.38** shows a beam printed at  $3 \text{ mm s}^{-1}$  and 1 bar. The measured strut thickness of  $0.86 \pm 0.03$  mm confirms again the freeform ability of the ink. Nonetheless, differently from the previous structure, some of the joints failed to connect, thus not acting as support for the upper layers. This issue could be attributed to the way that the beam has been designed and the limits imposed by the current setup. It should be considered that (i) the present UV-DIW technique is based on the continuous flow of the ink from the start to the end of the gcode and that, (ii) the nozzle can only move vertically while going upwards, as downwards movement are restrained by the collision between the extruded filament and the nozzle itself. This means that, in order to print all the required trusses of the beam, an intricate path had to be designed, consisting specifically in the continuous change of inclination with respect to the printing head and on the multiple passage of the nozzle in the same locations. Moreover, as previously described (see §2.3.1), a perfect match of the printing speed with the ink flow should consider the curing speed of the ink and directly depends upon the point of curing. Indeed, in order to avoid the nozzle clogging, the UV light was oriented to create a

shadowed space of 1 mm with respect to the nozzle end, ultimately resulting in a partial collapse of the extruded filament in correspondence of the more severe turns (highlighted in **Figure 2.39**).

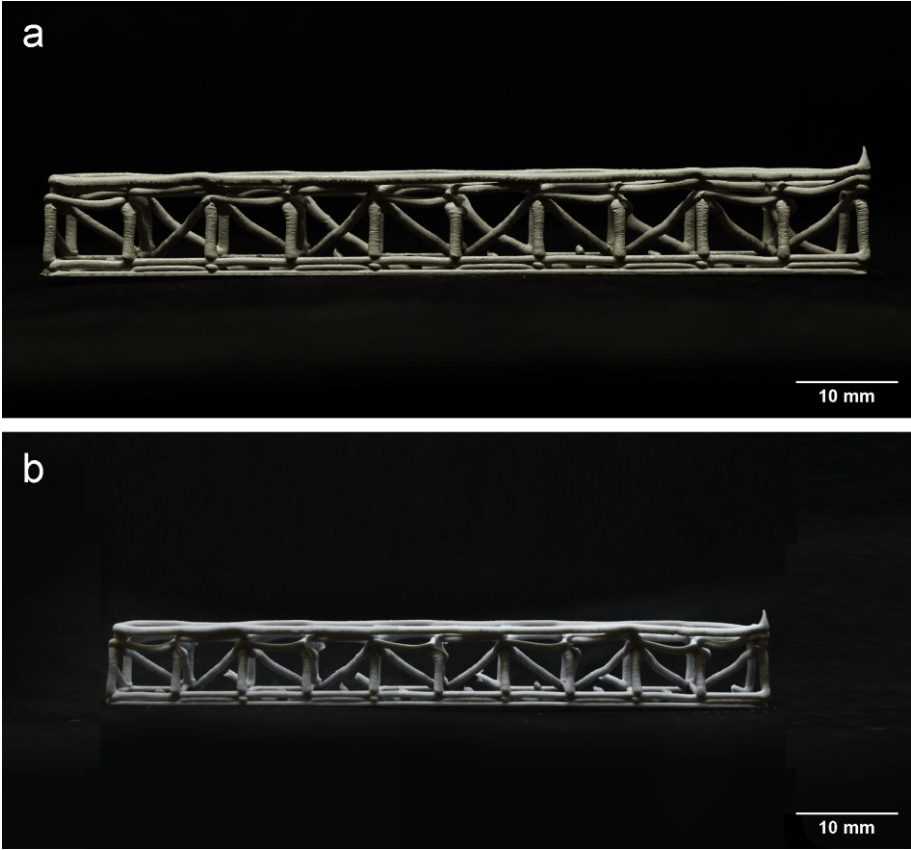


**Figure 2.38.** Truss-made beam structure: green state (a) and after sintering (b).

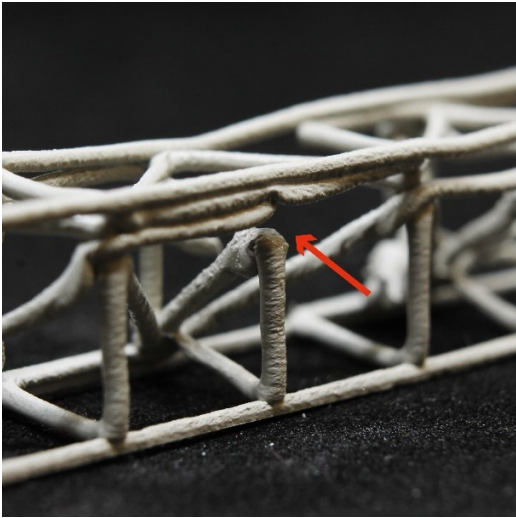


**Figure 2.39.** Magnification of a partially collapsed truss inside of the beam structure.

Once sintered (**Figure 2.38** (b)), lattice-beams were subjected to 4-point bending test. As shown in **Figure 2.40** (a), samples having cross-section  $h \times w$  were placed on two supporting pins equally distanced ( $L/4$ ) from two loading pins which were moved down at a constant rate of 0.7 mm/min until failure of the sample. By measuring the fracture load ( $F$ ), it is possible to calculate the flexural strength as:

$$\sigma_f = \frac{3 FL}{4 wh^2} \quad (7)$$

Data thus obtained can be described through the Weibull distribution, which represents the probability density function for strength variables:

$$f\left(\frac{\sigma}{\sigma_0}\right) = \frac{m}{\sigma_0} \left(\frac{\sigma}{\sigma_0}\right)^{m-1} \exp\left[-\left(\frac{\sigma}{\sigma_0}\right)^m\right] \quad (8)$$

Where  $m$  is the Weibull modulus,  $\sigma$  is the flexural strength and  $\sigma_0$  is a normalizing parameter. Through the linear-regression method [197] it is possible to plot the flexural strength values obtained from (7) as a function of their survival probability (1-P), thus obtaining the graph shown in **Figure 2.40** (b), which reports the statistical distribution of the calculated flexural strengths performed on 11 different samples. By fitting of a linear curve, it is possible to estimate  $m$  (i.e., slope of the curve) and  $m \cdot \ln(\sigma_0)$  (i.e., intercept) and obtain characteristic values of  $m = 1.84 \pm 0.11$  and  $\sigma_0 = 18.8$  MPa. As the Weibull modulus is a measure of the mechanical reliability of the tested specimens, high values (i.e.,  $m \sim 20$ ) should be preferred, thus indicating of a narrow defects size population. Nonetheless, as previously reported, the presence of closed porosities and/or cracks in correspondence of the connection points (**Figure 2.34**) and of partially collapsed trusses (**Figure 2.39**), makes the distribution of defects quite wide and not homogeneous. Moreover, as demonstrated by Keles et al. [198], low values of  $m$  (i.e.,  $m < 10$ ) are generally expected for highly porous (i.e.,  $> 50\%$ ) ceramics – as the lattice beams here analyzed. Indeed, similar considerations can be made regarding the low value of flexural strength obtained (i.e., 18.8 MPa) compared to the target strength expected from Kyocera's material (i.e., 700 MPa). As reported by Larsen et al. [199], a quantitative relationship can be used to describe the porosity dependence of the strength for silicon nitride, being:

$$\sigma = 598 \exp(-5.5\varphi) \quad (9)$$

Considering the overall volume fraction of porosity ( $\varphi$ ) equal to 74% (i.e., lattice beam porosity + open porosity in the struts), this results in a theoretical flexural strength of 10.2 MPa, which is consistent with the experimental one, thus ultimately validating the fabrication of porous  $\text{Si}_3\text{N}_4$  lattice structures using the UV-DIW technique.

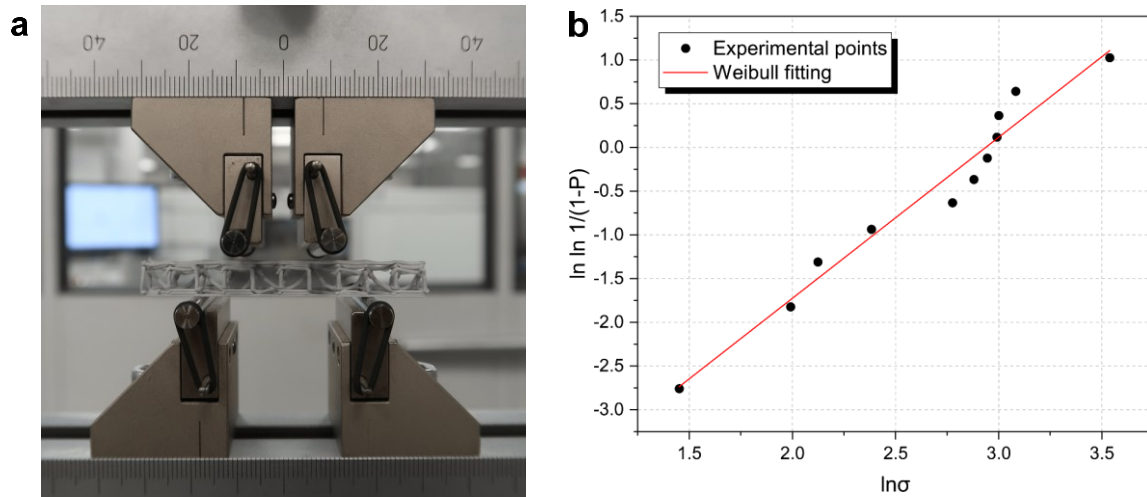


**Figure 2.40.** (a) lattice beam specimen on 4-point bending test, and (b) Weibull graph from bending test performed on 11 lattice beams samples.

## 2.5 Hybrid UV-DIW on a robot arm

The following section has been partially published in: [De Marzi, A.](#), Vibrante, M., Bottin, M., Franchin, G., "**Development of robot-assisted hybrid additive manufacturing technology for the freeform fabrication of lattice structures**" Additive Manufacturing, vol. 66, 2023, p. 103456.

It is clear by now that while the hybrid technique presented can overcome the limits of the layer-by-layer construction, such a freeforming process still relies on a 3-axis setup: the high degree of freedom given by the non-planar construction is limited by the collision of the printing head with the printed structure [200], [201]. In addition to that, the angle between the nozzle and the deposition direction varies during the printing process, hence continuously changing the point

of solidification and affecting the accuracy of the free-hanging structure [66], [202]. Such a phenomenon is even more clear in the 3D honeycomb-like structure (**Figure 2.41**) where both downward and upward movements of the nozzle are present. In particular, as the nozzle moves downwards on the semi-hexagon shape, its shadows the extruded filament retarding its curing and causing its partial collapse.

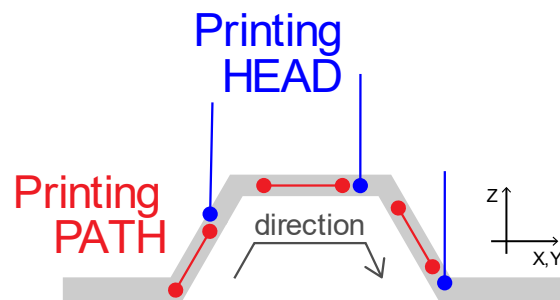


**Figure 2.41.** Schematic of the printing head and path direction during the printing of a semi-hexagon shape.

Given the limitations imposed by the constrained orientation of the printing head, the next step towards technological advancement could only be achieved by transferring the UV LEDs array setup to a 6-axes robotic arm [203]–[206]. By unlocking these additional axes, a higher degree of freedom of the printing head is permitted: equal irradiation of the filament through the entire print is obtained, resulting in more precise shape retention and structural accuracy.

A custom UV LEDs setup was designed and then mounted as the end-effector of a 6-axis robot arm. A schematic of the setup is shown in **Figure 2.42**. It consists of a dispensing system - extruder (vipro-HEAD 3, ViscoTec Pumps and Dosing Technology GmbH, Germany) and UV-blocking nozzle tip ( $d = 0.84$  mm, Vieweg GmbH, Germany) - installed as the end-effector on a 6-axis industrial robot (RV-4FRL-D, Mitsubishi Electric Corporation, Japan). The printing of the parts takes place above an elevated non-reflective glass plate to avoid the non-homogeneous solidification of material caused by the reflected UV light from the plane. The connection of the extruder to the robotic flange is possible through the use of aluminum support. Such support has been designed so that the robot workspace is maximized. The encumbrance of the extruder makes it easy for the robot to collide with its structure when tight movements are required by the task. A custom 3D printed copper add-on was instead designed to allocate a set of six UV LEDs (395-400 nm,  $I=34$  mW cm<sup>-2</sup>, 3 Watt) which was placed around the nozzle tip of the extruder and used to dissipate the heat generated by UV LEDs.



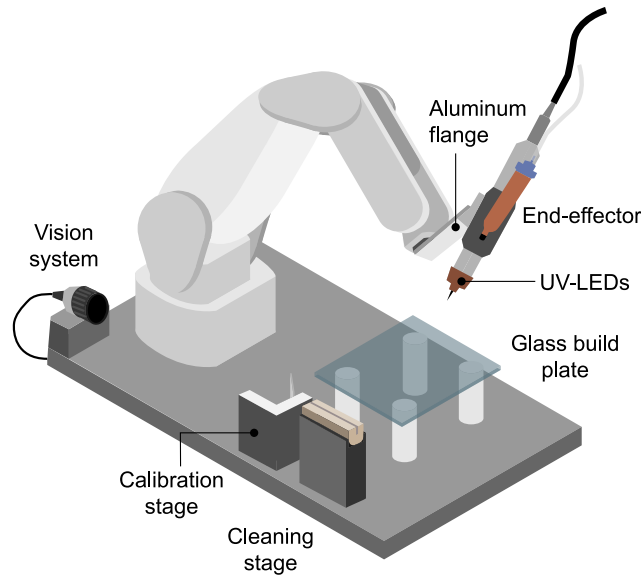


**Figure 2.42.** Schematic of the robot hybrid UV-DIW setup.

The fabrication of components using the robot-assisted hybrid AM technology was possible thanks to the development of a custom Graphical User Interface (GUI), schematized in **Figure 2.43**. Specifically, G-code files are the input data for the GUI: they contain information about the cartesian coordinates of the path, the printing speed, and the extrusion parameter ( $E$ ), defining the deposition of the material along the cartesian path. G-code files are then processed following two different paths. On one hand, the cartesian coordinates of the G-code file are converted, through a kinematic inversion process, in joint coordinates and sent as output to the software RT Toolbox 3 (Mitsubishi Electric Corporation, Japan), which controls the robot movements. To guarantee printing accuracy, a vision system was employed to identify the nozzle position and orientation in the robot reference frame. It consisted of an Allied Vision Mako G-192B camera that points at a station composed of two back-light panels of plexiglass and a mirror, disposed like in **Figure 2.44**. To properly calibrate the nozzle in the building space, the camera takes a picture of both the nozzle tip and its reflection in the mirror: the direct and reflected images of the nozzle are processed and compared to a reference position, thus allowing to correct and calibrate the  $X$ ,  $Y$ , and  $Z$  coordinates, as well as the rotations ( $\alpha$ ,  $\beta$ ,  $\gamma$ ) around the axes of the nozzle reference frame.

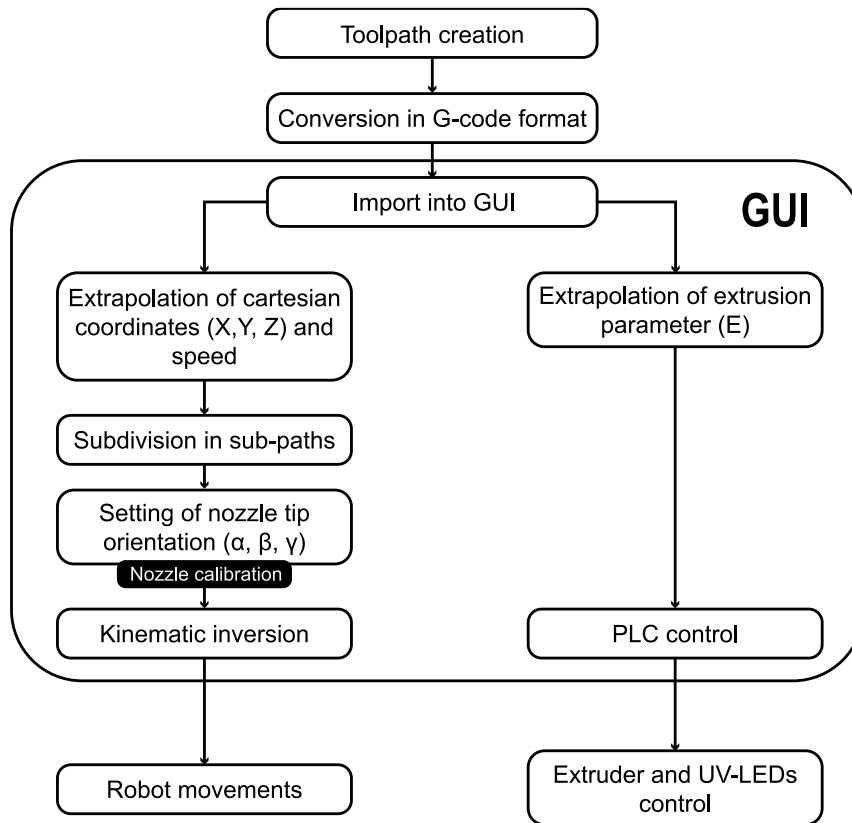


**Figure 2.43.** Flow chart of the part production process using the GUI.

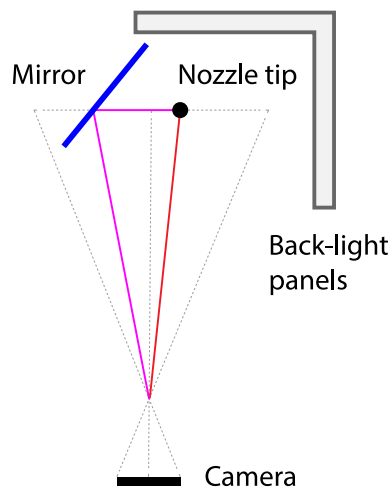


**Figure 2.44.** Scheme of the vision system viewed from the top.

On the other side, a PLC (EK1100, Beckhoff Automation GmbH & Co. KG, Germany) is employed to control the switching of the module associated with the extruder (EL7370, Beckhoff Automation GmbH & Co. KG, Germany) and that of the UV-LEDs (EL2808, Beckhoff Automation GmbH & Co. KG, Germany). This information is essential to simultaneously control

the robot movements and the end-effector through the PLC, but it is not sufficient. Indeed, the kinematic of industrial robots, and in particular that of the anthropomorphic manipulators, requires information about translations, rotations, and configurations of the robotic arm to execute the kinematic inversion.

The translation movements are provided by the cartesian coordinates of the G-code file and the configuration is defined by default as the result of an optimization of the robot workspace; on the other side, the rotations that the nozzle tip assumes along the path during AM operations can either be manually set by the user or automatically calculated by the GUI. In the first case, the orientation of the nozzle with respect to the vertical direction will be kept constant throughout the printing process. This limits the high degree of freedom provided by the additional axes possessed by the robot arm compared to 3-axis AM techniques. In this sense, the GUI was customized to automatically calculate the inclination of the end-effector: the nozzle tip was oriented to keep its axis always coincident with the direction of the G-code path. Considering the encumbrance of the end-effector and the optimization of the workspace, an angle of  $60^\circ$  with respect to the vertical direction was found as the maximum inclination capacity of the end-effector setup. The E parameter is also fed through the G-code file, which represents the length of the truss to be extruded. The GUI translates such parameters in the rotational speed of the extruder by using a multiplier which depends on the truss printing speed. The printing speed range was defined between  $0.5$  and  $5 \text{ mm s}^{-1}$ .

### 2.5.1 Printing and freeform ability

The UV-DIW printing process derives from the coupling of the DIW technique with an external UV source: the printing parameters usually associated with the extrusion processes (i.e., printing speed and flow rate), had to be tailored also considering the polymerization mechanism of the ink. Specifically, as previously demonstrated, a suitable ink for the UV-DIW process is represented by a highly reactive photo-curable paste possessing sufficient viscosity to allow for a stable flow out of the nozzle and a flow rate than can be matched by the curing rate of the system [207].

In order to clearly address the challenges associated with the complex setting up of the new system, a simple model material was here employed, with the aim of moving later into ceramic-containing inks. A commercially available resin (Industrial Blend, FunToDo, Netherlands) consisting in a mixture of acrylate and diacrylate monomers combined with a phosphine oxide-based photoinitiator was selected for its rapid curing behavior upon exposition to UV light [208]; 0.5 wt% of a coloring dye (E122, Squires Kitchen, England) was introduced to create a visible contrast between the building plate and the trusses during the printing process.

The commercial resin shows high reactivity, yet it also displays a nearly Newtonian behavior in the range of shear rates  $1\text{-}1000\text{ s}^{-1}$  with a viscosity (of  $0.14\text{ Pa s}$ , shown in **Figure 2.45** (a)) too low to meet the process requirements. Therefore, to tailor its rheological behavior, the resin was loaded with different fractions of hydrophobic fumed silica treated with octamethylcyclotetrasiloxane (Aerosil® R 106, Evonik Industries AG, Germany). As expected, an increase in the value of the solid loading – from 5 wt% (2.6 vol%) to 10 wt% (5.4 vol%) – results in the gradual increase of the ink viscosity and a shift from a Newtonian to a shear-thinning behavior, as shown in **Figure 2.45** (b), which aids preventing the sagging of the extruded filament before its curing [65]. The ink with 10 wt% loading was selected as it matches the behavior of the silica-based ink shown in §2.3.1.

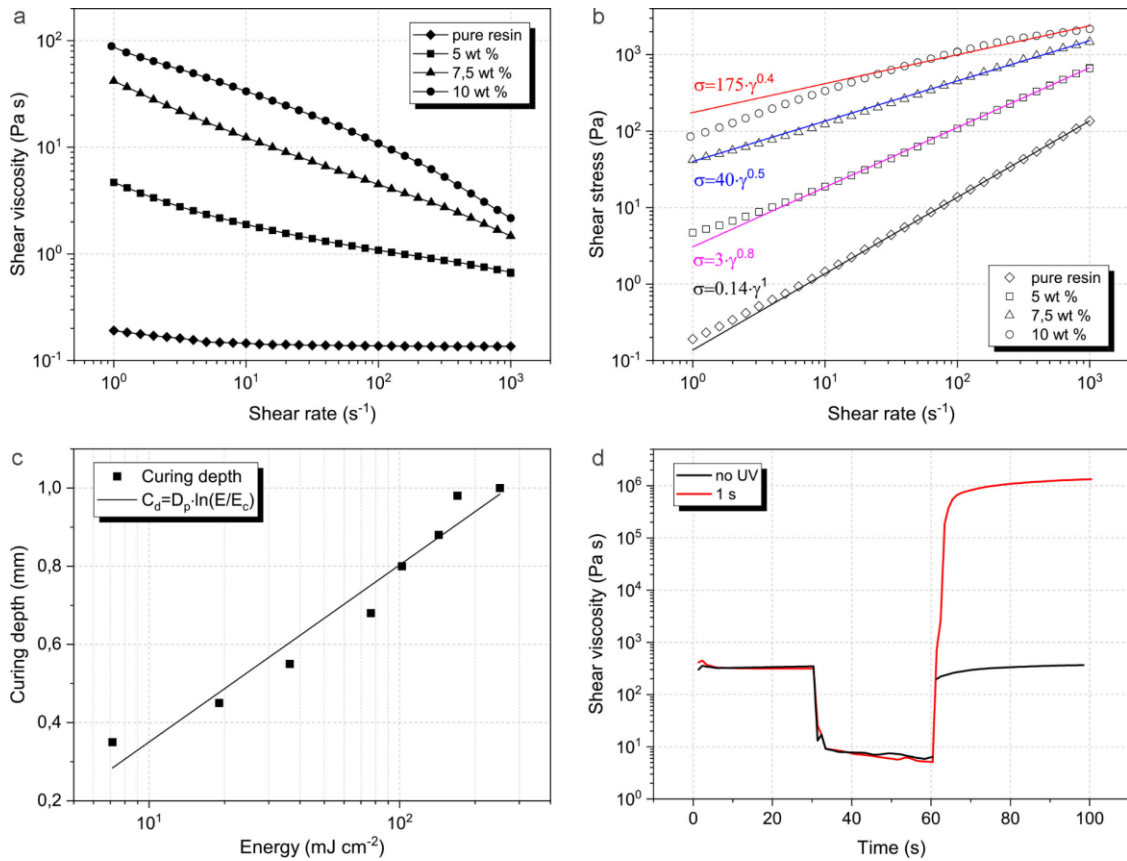


**Figure 2.45.** Effect of the amount of silica on the (a) viscosity and (b) shear stress profile; (c) curing depth of the ink as a function of exposure energy density (logarithmic scale); (d) comparison of the three intervals thixotropy test (3ITT) on the 10wt% ink.

[65] The critical energy dose required to start the polymerization process can be calculated using the Jacobs equation (5), as described in §2.3.1. The curing depth values of the ink were measured as a function of the energy density, as reported in **Figure 2.45** (c). By following (5), the fitting of the experimental values returns the characteristics parameters of the ink:  $D_p = 0.19 \pm 0.02$  mm and  $E_c = 1.7 \pm 0.6$  mJ cm<sup>-2</sup> ( $R^2 = 0.95$ ). Hence, a filament having a diameter of 0.84 mm would require only 0.46 s to fully cure upon radial exposition to UV light ( $C_d = 0.42$  mm,  $E = 15.5$  mJ cm<sup>-2</sup>,  $I = 34$  mW cm<sup>-2</sup>), suggesting a rapid retention of the filament after extrusion.

The freeform ability of the ink was verified by assessing its stiffness after curing; to do so, the 3ITT was employed. Specifically, as shown in **Figure 2.45** (d), if the UV light is not switched on after extrusion, the ink takes a long time (> 20 s) to regain its initial viscosity; on the other hand, when the ink is UV-cured, there is a rapid increase of viscosity (3 orders of magnitude higher than its initial status). This suggests that a rigid cured filament can rapidly retain its shape after extrusion, thus validating its freeform ability.

While more mechanically efficient structures will be proven able to be printed using the robot-assisted hybrid UV-DIW, the high degree of freedom offered by the technology was firstly demonstrated by fabricating the honeycomb structure. As shown in **Figure 2.46**, the high reactivity of the ink coupled with the increased degree of freedom of inclination of the printing head, results in a higher correspondence of the digital model with the printed component. Additionally, as a proof-of-concept of the system capabilities, different truss-made structures (i.e., interlocked geometries, dodecahedron and fullerene cell) were printed (**Figure 2.47**).

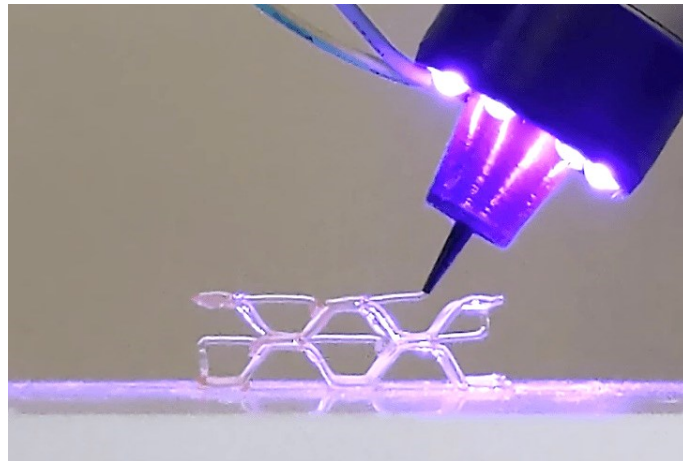


**Figure 2.46.** Video frame of the honeycomb structure being printed with the robot assisted hybrid UV-DIW setup. Note that in the early stages of setup development, no photo-absorber was present in the ink (hence the transparent color of the structure).

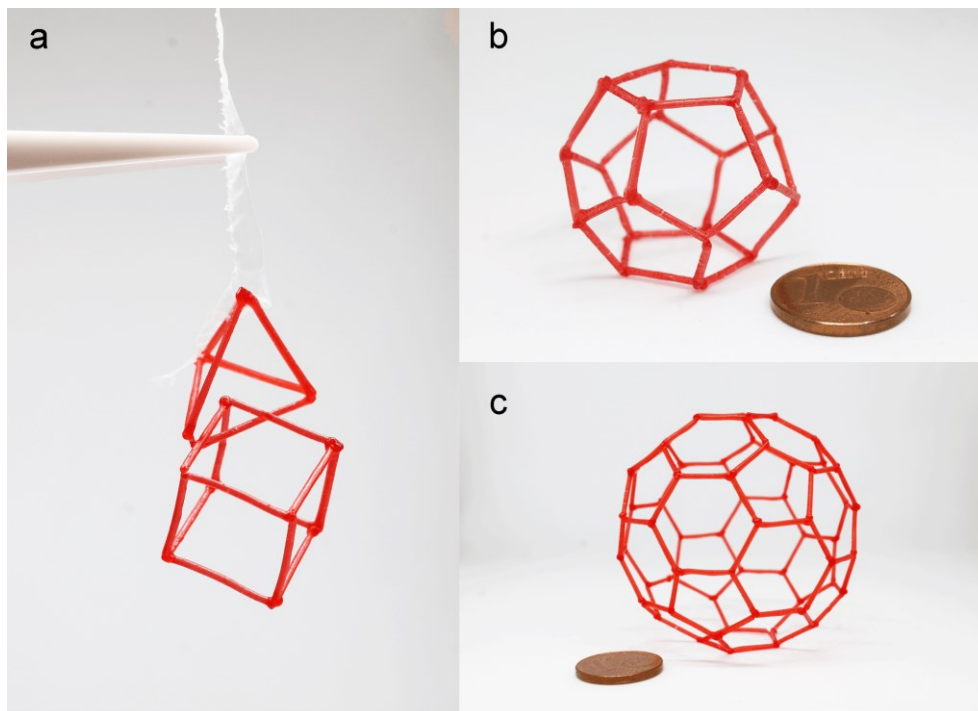


**Figure 2.47.** Different truss-based components are printed with the hybrid UV-DIW robot-assisted AM technology. Interlocked cube and triangular pyramid (a); dodecahedron cell (b); fullerene cell (c).

## 2.5.2 Fabrication of lattice structures

Lattices are a particular class of cellular solids characterized by the repetition of a regular pin-jointed frame made of trusses and surrounded by a void space [209]. A more rigorous classification can be done based on their connectivity and its influence on the deformation mechanism. Specifically, whereas low-connected lattices deform following a bending-dominated mechanism, high-connected lattices behave as stretch-dominated structures, meaning that their trusses do not bend upon loading but only carry tension or compression [210]. Such mechanism for the distribution of stresses creates a rigid, un-foldable structure with a strength-to-weight ratio especially suitable for lightweight structural applications (i.e., aerospace, bio-engineering, and architecture) [211], [212]. Typical representations of such configurations are tetrahedron and octahedron shapes, which gained great importance due to such mechanical properties [209], [213].

Demonstrating that such structures could be produced with the UV-DIW robot assisted system could validate its capabilities. Indeed, with additional axes available, a higher degree of freedom of the printing head movement is permitted: equal irradiation of the filament through the entire print is obtained, resulting in a more precise shape retention and structural accuracy. Moreover, such increased control over the inclination of the printing head with respect to the printing path is set have a major effect on the final mechanical properties of such structures, thanks to the absence of interfaces.

Octets were designed having a unit cell length of 10 mm and thickness of 0.84 mm (**Figure 2.48**) – corresponding to the diameter of the nozzle – therefore resulting in a theoretical aspect ratio  $\nu$  equal to 0.084 ( $\nu = \phi / L$ ). Whereas higher aspect ratios are usually desired in order to increase the final stiffness of the lattices [209], structures possessing low values of  $\nu$  results in a higher energy absorption [214], making them particularly useful for lightweight and dynamic load conditions.

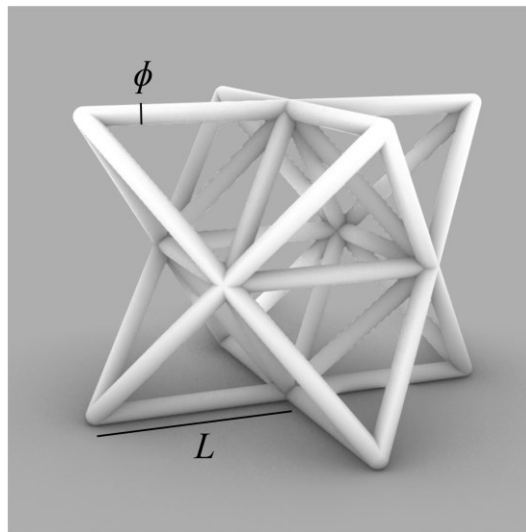


**Figure 2.48.** Render image of the CAD model of an octet cell.

Thanks to the use of an automatic extruder, allowing to systematically control the flow of the ink, the construction of the part using the UV-DIW technique coupled with the custom GUI is characterized by a discontinuous depositions of ink forming the trusses. **Figure 2.49** shows a simulation of the printing process. Initially, the robot moves so that the tip of the extruder gets near the initial point; once in its proximity, the extruder approaches it by keeping its axis coincident with the direction of the to-be-printed truss (1). As the extrusion starting point is reached,



ink is pre-extruded for a certain time (s), thus assuring the adhesion of the new truss to the platform or previously printed part (2). After that, the filament is extruded while moving at a certain printing speed and with the UV light switched on (3); at the end of this phase, an extra UV exposure time (s) can be scheduled during which the extruder is not moving and does not extrude additional material (4). After that the filament is rigid enough to support itself, UV light is switched off and the extruder departs keeping its former direction (5). Finally, after moving away from the filament, the extruder travels again either to continue the construction of the next truss (6) or to the nozzle cleaning stage. Indeed, preliminary experiments highlighted frequent clogging and extrusion imperfections during the printing process, thus leading to the accumulation of cured material around the nozzle end and consequently badly influencing the deposition of the next trusses. Therefore, the setup was provided of a cleaning nozzle tip station, ultimately resulting in a reduction of material waste and increase of printing repeatability. In addition to that, it was demonstrated how slower printing speeds are usually best for support-less features – since it means an increased energy dose in the same point – thus assuring a faster increase of the ink rigidity [66].

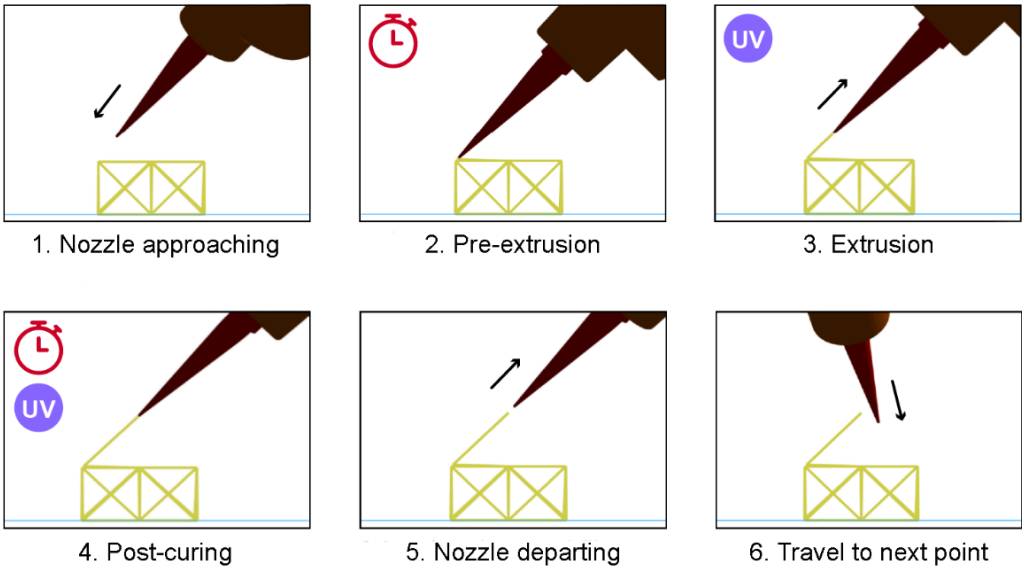


**Figure 2.49.** Production part phases.

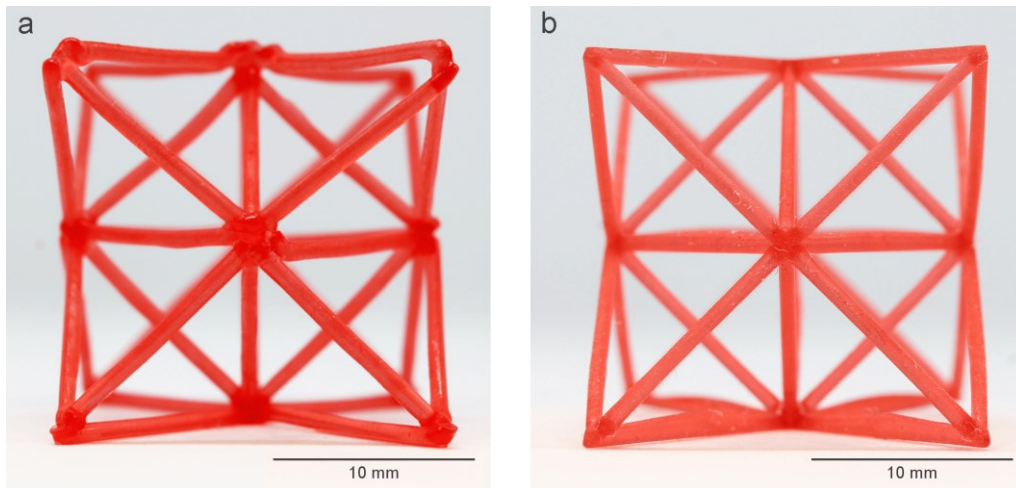


**Figure 2.50.** Printed octet lattices; (a) via hybrid UV-DIW; (b) via DLP.

**Figure 2.50** (a) displays the obtained octet in which trusses were printed at  $0.85 \text{ mm s}^{-1}$ . As it is possible to notice, there is a quite good resemblance with the digital model; struts have a thickness of  $0.96 \pm 0.06 \text{ mm}$  and they are oriented at an angle of  $44.5 \pm 0.5^\circ$  in the front view. The noticeable discrepancy between the measured and modelled strut thickness (i.e.,  $0.84 \text{ mm}$ ), suggests a slight mismatch of the extruder speed with the printing one, as well as swelling associated to polymer extrusion [215]. On the contrary, the inclination of the struts reflects the designed one (i.e.,  $45^\circ$ ) in all directions. When compared to what described in §2.3.1 and §2.4.2, this is deemed possible by the increased degree of freedom provided by the robot arm. Thanks to the custom developed GUI, it is possible to tilt the printing head and orient it along the truss axes, consequently avoiding the partial hindrance of the extruded filament by the nozzle and allowing for a precise shape retention along the define printing paths.

### 2.5.3 Effect of the manufacturing method on the mechanical properties

Thanks to the optimal orientation of the printing head with respect to the printing path, it is possible to fabricate components in a non-planar fashion. Therefore, failure mechanisms associated to the stress evolution promoted by the interlaminar interfaces in layer-wise produced components can be avoided [216], [217].

In order to verify such hypothesis, the mechanical properties of the octet lattices printed employing the presented hybrid UV-DIW technique were compared to those fabricated using a DLP printer (Prusa SL1, Prusa Research, Czech Republic) (**Figure 2.50 (b)**). It should be noted that DLP octets were fabricated using the less loaded ink (5 wt%). In fact, only inks with lower viscosity (i.e., below 5 Pa s) could be processed (i.e., easily and quickly cured) [29]. The effect of a 5 wt% increase in the silica content on the elastic modulus of a polymer nanocomposite is expected to be only marginal [218]. On the other hand, it can have a larger influence on its tensile strength: in similar materials, depending on the polymer matrix, the strength is shown to increase by about 12% to 24% when the silica content increases from 5 wt% to 10wt% [219].

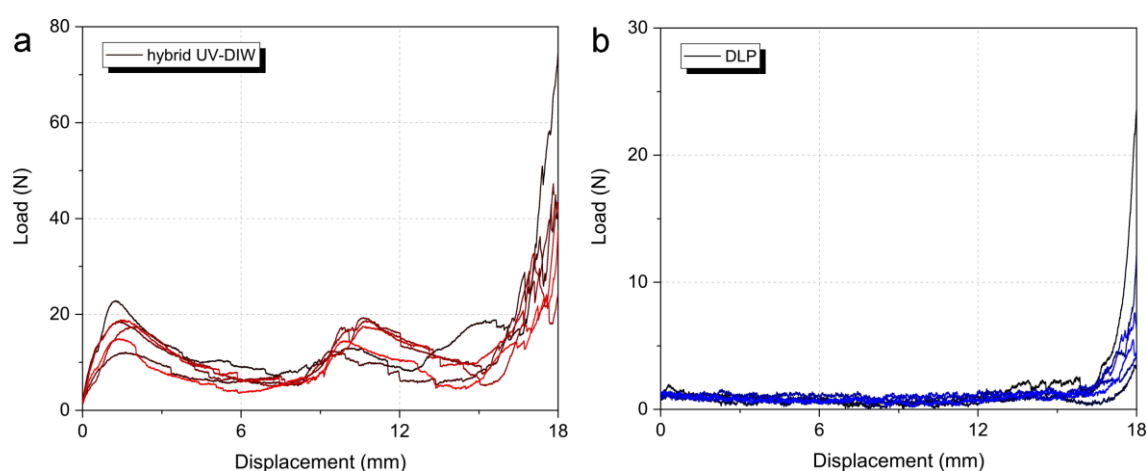


**Figure 2.51.** Load vs. displacement curves for the octet cells printed with hybrid UV-DIW setup (a) and DLP machine (b).

**Figure 2.51** shows the compressive behavior of the two lattices tested using a universal testing machine (Quasar 25, Galdabini S.r.l., Italy) operating with a crosshead speed of  $2 \text{ mm min}^{-1}$ . As expected, both structures behave as cellular solids: as the displacement increases, a first peak in the load (i.e., collapsing value) is reached, denoting the elastic region. Afterwards, lattices enter the yielding phase, characterized by a fluctuation of the load value; this depends on the buckling, collapsing and re-distribution of the applied compression force to adjacent integer struts. Finally, there is a rapid increase of the load due the compression of the material between the testing machine plates [213].

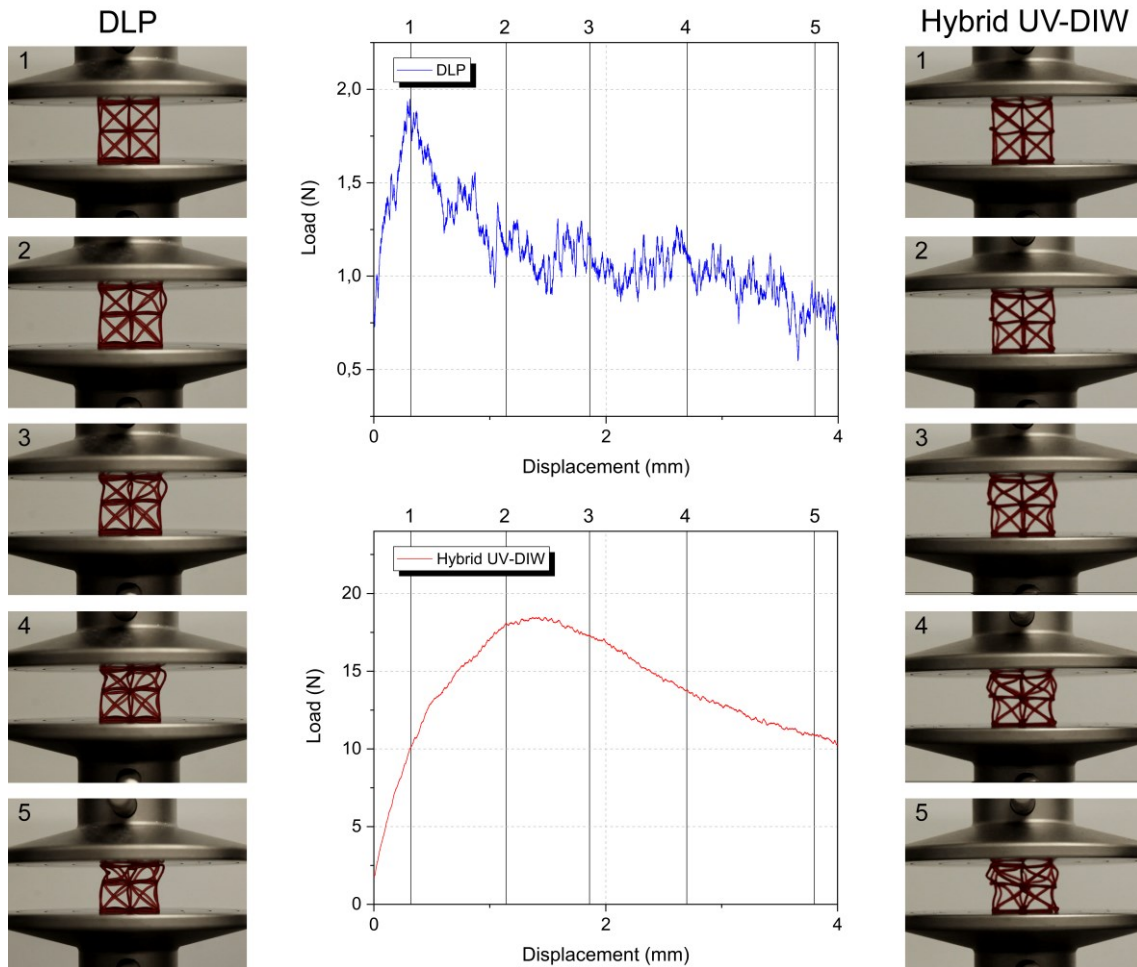


**Figure 2.52.** Comparison of the failure mechanism of octet fabricated using a DLP printer and the hybrid UV-DIW setup by means of video frames and their corresponding moment in the compressive curves.

As a further confirmation of their cellular-like behavior, the failure mechanism of the two structures is observed; **Figure 2.52** indeed shows that both octets collapse by a gradual failure of the singular cells, moving from the one close to the moving plate through the static one [220]. However, differences between the two collapsing values can be noticed which should be attributed to the different manufacturing methods employed. Specifically, structures obtained via DLP display a collapsing value lower by 1 to 2 orders of magnitude compared to the one showed by octets printed via the hybrid technique.

This can be attributed to two different mechanisms. The first one depends on the hybrid UV-DIW production process: in order to guarantee the connection between a new extruded truss and the already printed part, a pre-extrusion stage is performed at the beginning of each of the filaments. As a consequence, a higher amount of ink is accumulated in the nodes – as visible in

**Figure 2.53** – thus leading to an increase of the rigidity of the final component [206], [221]. Differently, DLP structures are printed by the subsequent curing of the slices composing the CAD model. As depicted in **Figure 2.50** (b), such a method allows for the fabrication of quite precise structures, thanks to the higher resolution of the DLP printer compared to the robot-assisted UV-DIW, which consequently avoids the broadening of the node zones, thus however resulting in a poorer mechanical response.

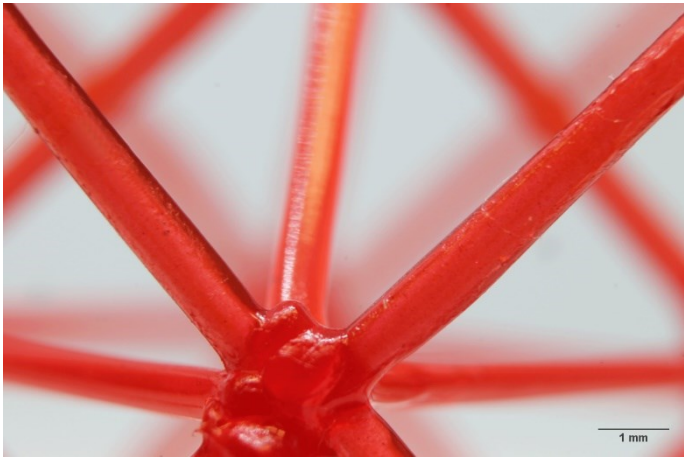


**Figure 2.53.** Close-up of one node of an octet printed with the hybrid UV-DIW technique.

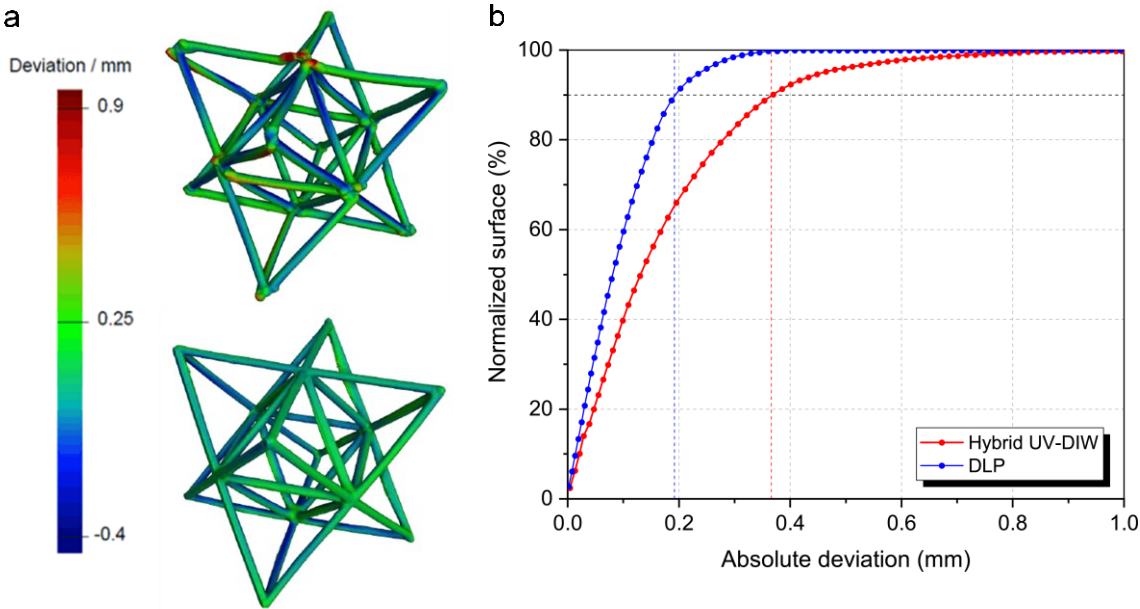


**Figure 2.54.** (a)  $\mu$ -CT of octets fabricated using the hybrid UV-DIW (a) and DLP (b) techniques with colormap representing their deviation with respect to the CAD model; (b) normalized surface (%) as a function of the absolute deviation. *Courtesy of N. Bonato and S. Carmignato, University of Padova.*

Such differences were further confirmed by scanning both octets through  $\mu$ -CT: **Figure 2.54** (a-b) displays the results of the comparison with the CAD model. As it can be noted, deviations up to the dimension of the nozzle diameter (i.e., 0.9 mm) can be measured in the octet fabricated through the hybrid technique, particularly in the correspondence of the upper part of the structure. This is confirmed considering the absolute deviation of the normalized surfaces: **Figure 2.54** (b) indeed shows that the majority (i.e., 80%) of the robot-printed structure is characterized by errors up to 30  $\mu$ m, which are consistent with the resolution of the hybrid setup and its displacement (see Appendix A – Robot calibration for UV-DIW).

In order to assess the impact of the nodes on the mechanical behavior, the CAD model employed for DLP (**Figure 2.48**) was modified; to mimic the robot pre-extrusion, spheres with a 0.9 mm diameter (i.e., consistent with deviations measured through  $\mu$ -CT) were added at the starting point of each of the trusses. **Figure 2.55** (a-b) shows the modified CAD model and the corresponding compressive behaviour of 6 different samples being printed via DLP. As expected, the accumulation of ink at the nodes results in an increment of the strength (i.e., from  $1.5 \pm 0.3$  N to  $8.0 \pm 1.2$  N); nonetheless, even considering the influence of the additional silica content discussed above, it remains significantly lower than that of octets printed with the hybrid technique (i.e.,  $17.5 \pm 3.7$  N).

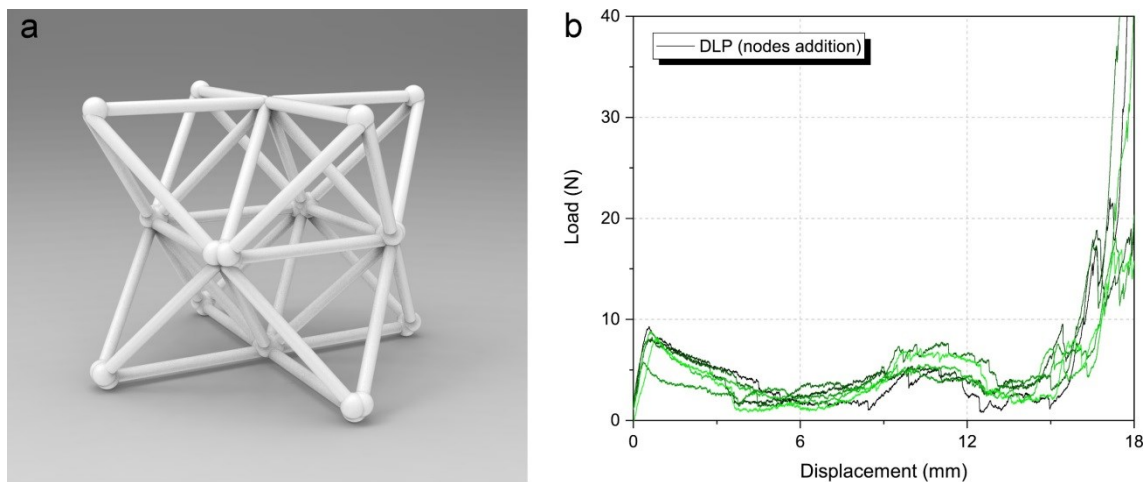


**Figure 2.55.** Render image of the CAD model of the modified octet with additional material in the node zones (a) and load vs. displacement curves for the structures printed via DLP (b).

The difference is therefore imputed to a second, more important mechanism, related to the presence of interlayer interfaces between layers which characterizes all the conventional AM

techniques, including DLP. Specifically, the layer-by-layer construction introduces an additional roughness on the surface of the trusses, thus reducing their quality and ultimately creating new stress concentration points for crack propagation [222], [223]. This is confirmed by **Figure 2.56** (a-b), which shows one of the 45° inclined trusses of the DLP-octet: the crack initiated from the interface between two adjacent layers and resulted in the final rupture of the truss perpendicular to the printing direction. SEM investigation of the filament in the proximity of the fracture surface **Figure 2.56** (c) confirms this finding and also shows crack formation at several other interfaces.

A wide range of collapsing values is displayed by the hybrid printed structures (**Figure 2.51** (a)); this can be attributed to errors associated with the robot arm setup. As previously stated, the setup design was chosen to maximize the workspace; on the other hand, its off-axis position lowers the precision of the last joint movements. In particular, the preliminary study (see Appendix A – Robot calibration) done for the calibration of the robot setup and building volume showed that the nozzle position can be misplaced up to its diameter size, introducing systematic errors which are compensated manually by locally adapting the printing parameters (i.e., change of pre-extrusion time, phase 3 in **Figure 2.49**). In this sense, the most optimal configuration for the hybrid UV-DIW setup would be reached by aligning the axis of the extruder with that of the last joint of the robot arm. Such adjustment, however, would result not only in a smaller workspace but especially in a smaller range of inclination reachable by the printing head, thus downsizing the free-forming ability of the hybrid setup.

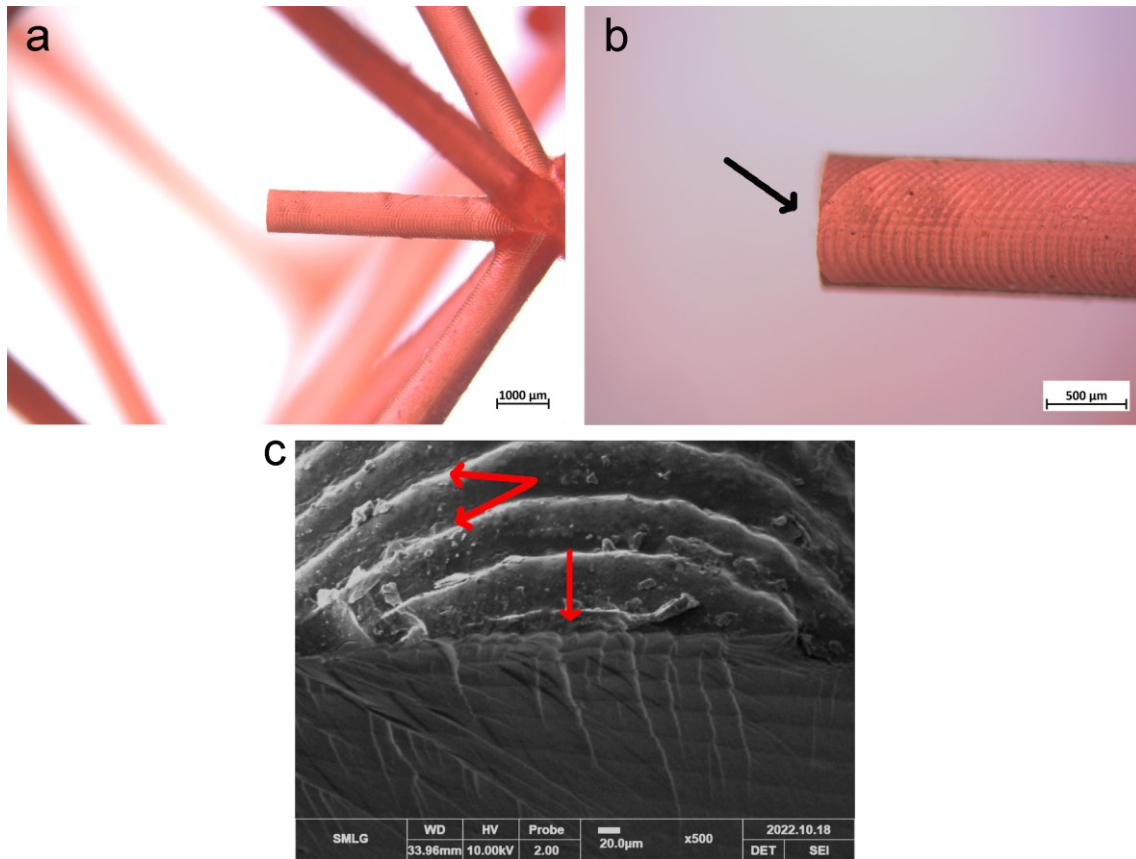


**Figure 2.56.** (a) truss of a DLP-octet broken during the compression test; (b) magnification and (c) SEM image of the fracture profile.



## Appendix A – Robot calibration for UV-DIW

The calibration method described in §2.5 has been tested with the experimental setup. After a calibration process, rotations around the three axes of the tool reference frame are performed, and the displacement errors of the tips with respect to the reference position are measured by means of the vision system. To assess the validity of the method, it has been compared with two other methods: the first one uses the transformation matrix between the robot flange and the tool reference frame retrieved by the CAD model, while the other uses the robot integrated calibration procedure, which is given by the proprietary software RT Toolbox.

Results are shown in **Figure A 1** (a-c). The results obtained with the proposed calibration method are aligned and, in some cases, even better than those obtained with the other existing methods. However, the main advantages of the proposed method rely on two aspects: time savings and reduction of human errors. As mentioned, the calibration process must be performed each time a new nozzle is manually mounted at the end of the extruder. The RT Toolbox method requires manual robot movements which may take a very long time and is prone to errors. Instead, the proposed method is fully automated by means of the GUI program. Moreover, the CAD method does not consider the inevitable changes in the tool reference frame that are due to the different nozzle tightening forces. As per our tests, the proposed method has proved to be more reliable and less time-consuming for the operator.

Please note that the design of the end effector is prone to manufacturing errors in all 6 degrees of freedom of the tool transformation matrix (both displacements and rotations) since none of the tool reference frame axes is aligned with the robot axes [224]. This design is required since the extruder is particularly long, thus cannot be installed aligned with the robot 6-axis.

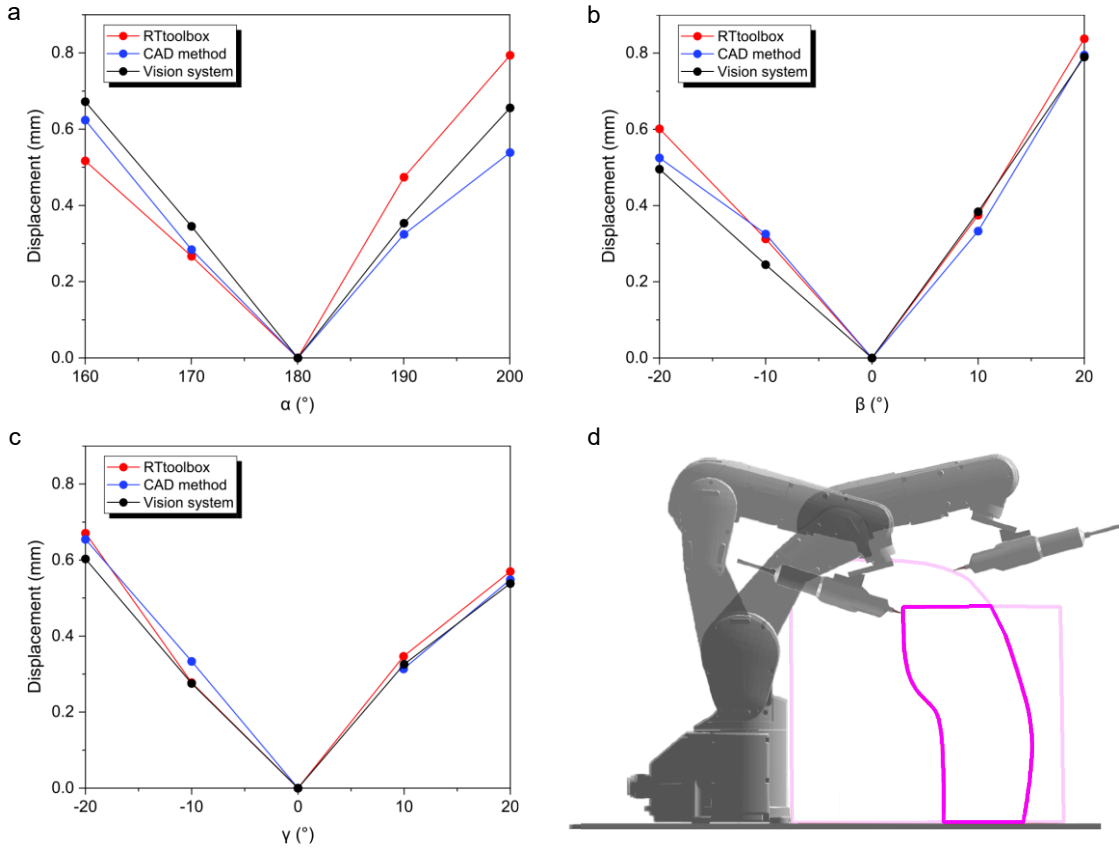


**Figure A 1.** Displacement of the nozzle tip with respect to the reference position during the rotation around the three axes of the reference frame:  $\alpha$  (a),  $\beta$  (b),  $\gamma$  (c). Valid robot configurations with the nozzle inclined of  $+60^\circ$  (right) and  $-60^\circ$  (left) with respect to the vertical axis. The overall valid workspace is the intersection of the two volumes (pink) (d).

To optimize the setup design, an analysis of the workspace dimension has been performed. In such analysis, the target was to calculate each position of the entire robot workspace in which the robot could print with the nozzle placed within a vertical cone with a maximum angle of  $60^\circ$  with respect to the vertical axis; in other words, every position of the workspace in which the robot can incline the nozzle up to  $60^\circ$  with respect to the vertical axis and rotate around the vertical axis about  $360^\circ$ . Both joint mechanical limits and collision with the work cell equipment have been considered. In **Figure A 1** (d) examples of valid configurations are shown where the nozzle inclination with respect to the vertical axis is either  $+60^\circ$  or  $-60^\circ$ . Each configuration can only reach specific positions; their intersection, i.e., the central volume in the graph, defines the valid workspace of the setup. Within this space, the printing volume can be placed according to the needs. Note that the tool has been designed so that the nozzle tip is inclined by  $45^\circ$  with respect to the last joint axis. In fact, the workspace volume with such an angle is around  $6800 \text{ cm}^3$ , while a nozzle tip aligned with the last joint axis would allow a

workspace of around 1000 cm<sup>3</sup>. Moreover, we decided to use a raised platform (**Figure 2.42**) in order to prioritize the printing area rather than the height.



### 3 Multi-material LSD-DIW technology

As already stated, the combination of different materials within the same print is set to increase not only the part performance and complexity but especially its functionality and range of application. Indeed, the simultaneous cooperation of different materials could potentially overcome limits imposed by conventional manufacturing methods, extreme atmospheric conditions, process costs or product weight. Specifically for this goal, the present Chapter will describe the fabrication of ceramic and multi-material components which was conducted at BAM (Bundesanstalt für Materialforschung und-prüfung, Berlin, Germany), the developer of the LSD-DIW technology, during an abroad research period of 6 months.

In this framework, the printing setup was developed starting from the previously published work of de Melo et al. [43], and resulted from the combination of a 6-axes robot arm assembled in an LSD machine, composed of a heated building plate and used to deposit layers of a ceramic slurry. The robot instead was used for both removal and addition of material thanks to a drilling tool and an extruder attached as end-effectors. Thanks to combination of such processes, the LSD-DIW technique allows for the fabrication of ceramic dense components having embedded three-dimensional paths.

It is clear that different combinations of materials can be coupled using the hybrid LSD-DIW technique; to fully exploit its potentialities, the set goal of the presented work was the fabrication of ceramic monoliths containing either complex channels or conductive paths, ultimately demonstrating the wide applicability of the LSD-DIW technology. Hence, an alumina-based (96%  $\text{Al}_2\text{O}_3$ ) HTCC (High Temperature Co-Firing Ceramics) powder (HS 14/2, CERA SYSTEM Verschleißschutz GmbH, Germany) and  $d_{50}$  of about 150  $\mu\text{m}$ , was selected as the ceramic base due to its chemical and thermal properties and co-firing capabilities [89], [225]; graphite and tungsten were respectively chosen as the sacrificial and metal phase. Indeed, by thermally treating the alumina/graphite part, it is possible to obtain a ceramic component with hollow channels which could be particularly interesting for the fabrication of heat exchangers

[226] and micro-reactors [227]. The conventional shaping processes for such components have been limited for many years to injection molding [228] and ion-etching [229], which require complex procedures and tools (i.e., molds, photo-lithography masks). DLP technique could overcome such issues and further increase the freedom of design, enabling the fabrication of very fine structures and geometries (i.e., dimensions of 5-20  $\mu\text{m}$ ). Nevertheless, the embedded channels would be filled with un-cured, ceramic filled ink, which can be difficult to remove prior to the debinding step and detrimental to the production of non-obstructed channels [226]. While the present LSD-DIW approach also employs a sacrificial material to provide the necessary support to subsequent layer build-up, its different chemical nature allows to obtain hollow, non-obstructed channels without the need of a cleaning step. Furthermore, the greater strength of the green body enables machining of complex geometries and a less delicate and time-consuming debinding during the subsequent heat treatment. On the other hand, an interesting application for multi-material components is also represented by the electric and IT industry [230], [231]. Here, the fabrication of robust multi-layer sensors or embedded circuits has been limited to the tape casting method: a metallic paste is printed over flat glass-ceramic sheets that are then pressed through lamination, resulting in very simple and not enthralling geometries. Hence, as a further advancement of the LSD-DIW technology [43] and following recent developments in the fabrication of multi-material components [89], tungsten paths were embedded into the alumina matrix, thus obtaining three-dimensional integrated conductive circuits.

The LSD-DIW printing process is depicted in **Figure 3.1** and consists in the repetition of three different steps: (1) the deposition of the ceramic slurry to form a predetermined number of layers, each of which was alternated with a drying phase before starting the deposition of a new layer of fresh slurry; (2) the selective removal of the dried ceramic through the machining tool, thus forming hollow channels; (3) the extrusion of a second phase ink to fill said channels.

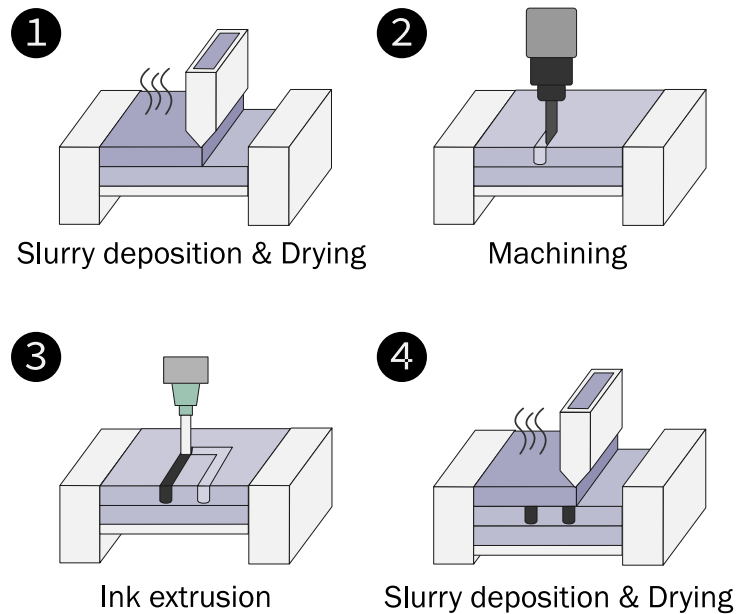


**Figure 3.1.** Process schematic of the LSD-DIW process.

Although the hybrid LSD-DIW setup can be considered as a fully integrated system [43], each of the printing steps and tools involved are controlled individually. Therefore, a custom graphical script was developed in Grasshopper to simultaneously manage the geometrical coordinates of the path and tools (see later, Appendix B – Grasshopper script for LSD-DIW). While it is important to finely calibrate the extrusion and machining tools mutual position within the robot environment, it is the slurry deposition (phase 1 in **Figure 3.1**) that represents the most crucial phase of the printing process. Indeed, the ceramic-based slurry should not only possess a shear-thinning behavior in order to easily flow and be spread by the doctor blades, but especially it should be able to rapidly dry without forming cracks.

As previously described in the introduction, the LSD step can be considered itself a hybrid technology deriving from the combination of tape and slip casting [42], [232]. Specifically, like tape casting, the slurry is being deposited using a doctor blade [32], while, as in slip casting, the layers are being deposited on a porous substrate [36] (first the heated platform and later the previously deposited and dried layers). When a newly fresh layer is deposited, its drying is driven by two different mechanisms: on one hand, the evaporation of the solvent due to the heated building platform; on the other hand, the absorption of the solvent due to the capillary forces exercised by the previously dried and porous layer (**Figure 3.2**). It is clear that fast drying rates should be preferred in order to accelerate the overall printing process, however, a too rapid

removal of the solvent leads to the formation of cracks. Indeed, as water is being removed from the slurry, the solid particles will get closer, and the deposited layer will shrink. Nevertheless, such layer is being constrained to the dried layer below and shrinkage is only possible in the out-of-plane direction, consequently creating a differential state of stresses which can result in cracking and distortions [233]. Therefore, in order to control the drying phase and avoid such defects, particular attention was posed onto the optimization of the slurry composition and, especially, on the appropriate selection of type and concentration of the binder/dispersant system (§3.2).

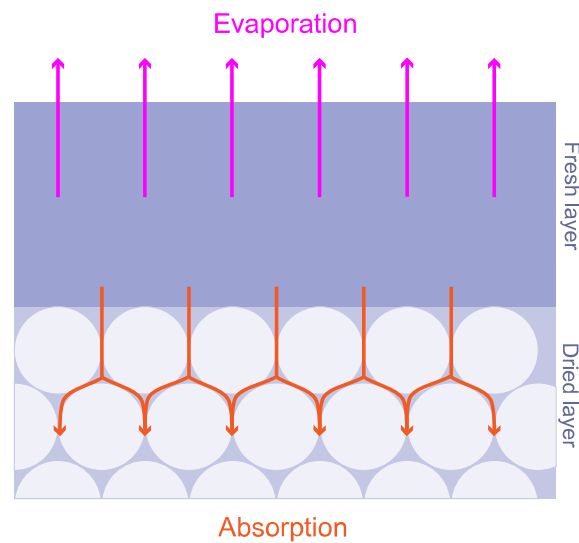


**Figure 3.2.** Graphical representation of the forces driving the drying phase of the LSD technique.

### 3.1 Hybrid setup and printing process

A schematic of the hybrid LSD-DIW setup is shown in **Figure 3.3**. It can be divided in two parts: the first corresponds to a six-axis robot arm (RV-E4NM, Mitsubishi, Japan) which end-effector consists in the combination of a machining tool (Dremel 4000, Dremel, Germany) with a 0.9 mm diameter drill bit (CEREC, Sirona Dental Systems GmbH, Germany), rotating at  $10^4$  rpm, and two dispensing systems – extruder (vipro-HEAD 3, ViscoTec Pumps and Dosing Technology GmbH, Germany) and syringe (30 cc, Nordson EFD, USA) with stainless steel tips ( $d = 0.84$  mm, Nordson EFD, USA). The machining tool is equipped with a flex shaft attachment (Dremel flexible shaft 225, Dremel, Germany) that can be installed on the robot arm



without occupying too much space or increasing the payload at the robot end. The machining and dispensing tools are placed orthogonally in respect of each other through the use of a custom aluminum flange. The extruder and the syringe are instead aligned together through the use of a PLA flange, such as that their nozzle ends are in the same height. Considering the previously published work [43], it has been already proven how the combination of a machining tool and extruder allows for the fabrication of porcelain/graphite parts. This double dispensing system, specifically developed during the research activity done at BAM, is to consider as a further improvement of the published setup, thus demonstrating that more than one secondary phase can be introduced in the ceramic matrix. The robot speed during the machining phase was set at  $10 \text{ mm s}^{-1}$  while the one during extrusion was selected in the range  $3\text{-}10 \text{ mm s}^{-1}$ .

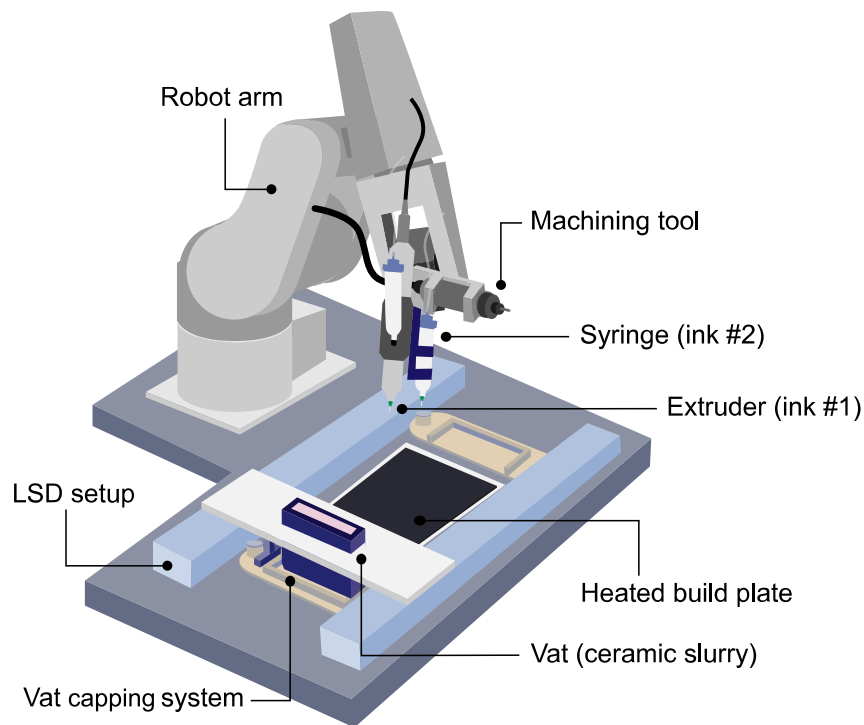


**Figure 3.3.** Schematic of the hybrid LSD-DIW setup.

The second part of the setup is a custom LSD machine which is composed of a  $200 \times 200 \text{ mm}^2$  heated porous platform which moves down along the Z direction in order to allow for the layer-by-layer fabrication of the ceramic matrix. The slurry is contained inside of a vat and poured along the plane of the platform with a deposition speed of  $80\text{-}100 \text{ mm s}^{-1}$ . The vat is used both as a slurry reservoir and as a deposition unit. The homogeneous spreading of the slurry on the platform is made possible through the use of two parallel blades leaving an opening of  $3 \times 60$

mm<sup>2</sup>. The distance between the bottom of the vat and the platform corresponds to the thickness of the layer which was selected in the range 100-150 μm. The platform was heated at a temperature of 95 °C, thus favoring the rapid evaporation of water from the deposited layer; typical values of drying time were in the range of 10-30 s.

It should be pointed out that the slurry is able to exit the vat by the combination of the gravitational force and deposition movement: in order to avoid the waste of material and/or any spillage outside of the deposition phase, two mechanical capping stations were added at the extremities of the platform. Details of such system are displayed in **Figure 3.4**. Its functioning can be explained by considering the deposition process: when the vat moves from one capping station to the other, a small vertical gap between the vat aperture and the platform (corresponding to the layer thickness) favors the flow of the slurry. Once the vat is in the proximity of the next capping station (1), the feet (one on each side of the vat) hit the station, thus lowering it and allowing the vat to move forward. Thereafter, the small gap in the center of the feet (see side view) allows the capping station to rapidly rise up thanks to the pin-cap connection and the addition of a spring, thus resulting in the blocking of the flow of slurry (2).

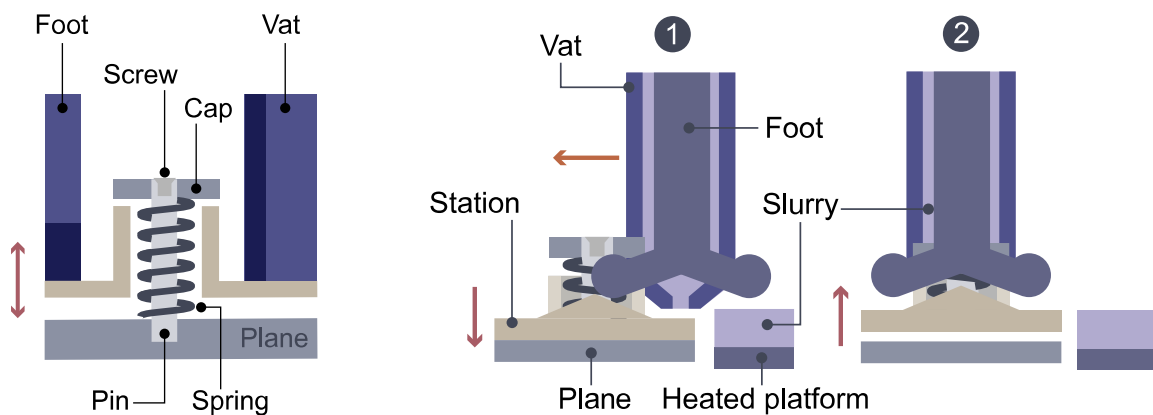


**Figure 3.4.** Schematic of the vat blocking system (front view) and its functioning (side view).

## 3.2 Alumina slurry optimization

Considering what was stated above, both the rheology and drying behavior of the slurry should be analyzed and controlled to obtain a suitable slurry for the LSD-DIW process. Indeed, a slurry

with high solids content and a shear-thinning behavior is desirable to favor the homogeneous deposition of the suspension with the desired thickness. At the same time, it should dry rapidly and without forming cracks; in this way, compact and uniform layers can be deposited one on top of the other, thus allowing for the fabrication of a green sample with high density.

In order to obtain such a slurry, available literature on both tape and slip casting was taken into consideration. Specifically, a classical slurry formulation consists in a mixture of different components, each of which have a different role and impact in the printing process [32], [234]. Clearly, the most important element is represented by the ceramic powder which should be dispersed into a liquid vehicle in order to increase its formability and, especially, create a slurry with low viscosity that can be spread with the doctor blades. Nevertheless, in order to reach a highly loaded and yet low viscous slurry, other fundamental ingredients are represented by surfactants and dispersants; their role is to coat and modify the surface of the particles, controlling the surface charge and increasing the particles dispersion while maintaining a low viscosity [235]. Lastly, binders and plasticizers are also added: they are constituted by long-chained polymers that partially adsorb onto the ceramic particles surface, inducing a gel-like behavior, i.e., changing the Newtonian behavior of the solvent to shear-thinning. Moreover, they remain confined between the particles during the solvent evaporation, increasing the strength of the network and the flexibility of the tape upon drying [235], [236].

Specifically for this work, the goal was the development of a water-based alumina slurry. While non-aqueous suspensions are usually preferred for tape casting, due to their higher drying rate and strength of the green part compared to water-based ones, they often employ either hazardous or environmentally toxic reagents [237]. Indeed, research over water-based slurries has recently increased also due to their cheaper cost [238]. Nevertheless, the high heat of vaporization [239] results in a dramatic built up of pressure during the evaporation which favors tape cracking [233]. The formation of defects should be controlled through the presence of different type and quantities of binders and/or plasticizers.

**Table 3.1.** List of alumina water-based compositions prepared.

wt%	1	2	3	4
Water	30.0	30.0	30.0	30.0
HTCC powder	70.0	70.0	70.0	70.0
Darvan® 811	1.5	1.5	1.5	1.5
AGITAN® 271	0.7	0.7	0.7	0.7
PEG 200	1.5	1.5	1.5	-
PVA	0.2	0.4	1.0	-
HEC	-	-	-	1.0

The research first focused on the development of an optimal mix of additives able to control the rheological properties and drying behavior of the slurry. **Table 3.1** shows the list of the compositions investigated. Poly(vinyl alcohol) (PVA,  $M_w$  31000-50000, Sigma Aldrich, Germany), and hydroxyethyl cellulose (HEC, Merck, Germany) were selected as potential binders. Darvan® 811 (Vanderbilt Minerals LLC, Germany), i.e., a sodium polyacrylate with  $M_w = 3500$ , and polyethylene glycol 200 (PEG200, Sigma Aldrich, Germany) were introduced to act as surfactant and plasticizer, respectively. The compositions shown in **Table 3.1** were formulated starting from an alumina concentration in water of 70 wt%; the weight fraction of the additives refers to their quantity with respect to water. Final weight (**Table C 1**) and volume (**Table C 2**) fractions are listed in Appendix C – Alumina water-based compositions.

A batch of slurry is produced by dissolving the selected binder in deionized water under magnetic stirring at 60 °C for 4 h. After that, the surfactant and the alumina powder are added, and the solution is ball-milled using  $Al_2O_3$  spheres with 8 mm diameter. Preliminary tests evidenced the formation of bubbles during the preparation of the slurry, therefore AGITAN® 271 (Münzing Group, Germany) is introduced as a defoamer. The slurry is finally mixed for 8 h on a roller mixer and then sieved in order to remove the  $Al_2O_3$  milling balls.

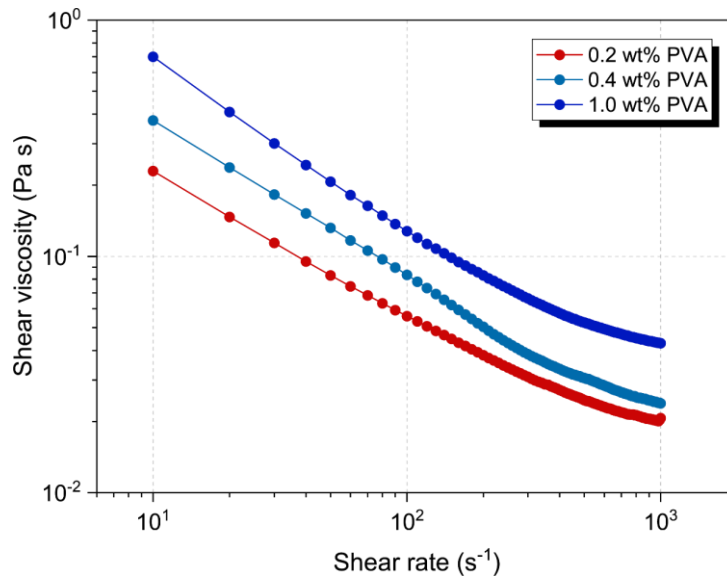


**Figure 3.5.** Effect of the amount of PVA on the viscosity profile of alumina slurries.

In order to verify the role of PVA inside of the slurry, the rheological flow curves of compositions 1, 2 and 3 were analyzed in a range of shear rate from 10 to 1000 s<sup>-1</sup>, using a rotational rheometer (MCR 301, Anton Paar GmbH, Germany) equipped with concentric cylinders ( $d_{\text{bob}}=27$  mm). **Figure 3.5** shows the viscosity profiles obtained. As expected, all three compositions possess a shear-thinning behavior thanks to the gel-like behavior promoted by the surfactant and binder mixture; moreover, increasing the PVA content resulted in an increase of viscosity. Nevertheless, considering typical values of shear rates during the deposition phase between 500 and 1000 s<sup>-1</sup>, the studied slurries present too low values of viscosity compared to the characteristics values for tape casting (i.e., 0.1 Pa s); this suggests not only a poor control of the layer thickness during the slurry deposition but, particularly, a higher sedimentation tendency [235]. Additionally, preliminary deposition tests using such slurries demonstrated that they could not efficiently prevent crack formation during the drying stage (**Figure 3.6**). This issue can be attributed to the poor binding between the alumina particles [240]. A possible solution to this problem could be represented by increasing the concentration of PVA; yet, it has been proven that the higher the amount of PVA and the higher the tendency of the slurry to foam and, consequently, to develop voids and defects in the green tape [241], [242]. Another way to overcome such problems would be to use a binder with higher molecular weight. Nevertheless, while different PVAs with  $M_w$  ranging from 22000 to 200000 were tested, none of those could efficiently prevent the rapid evaporation of water from the deposited tape, ultimately resulting in similar appearances as the one shown in **Figure 3.6**.

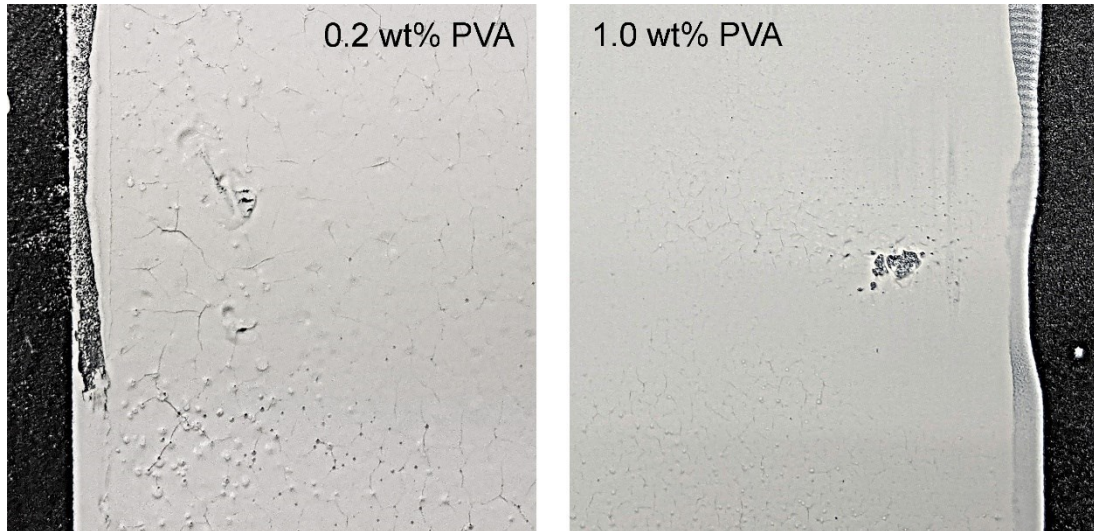


**Figure 3.6.** Top view of the defects and cracks of dried layer of alumina based slurries with 0.2 wt% (left) and 1 wt% (right) of PVA.

Hence, in order to control the drying phase without dramatically increasing the viscosity of the slurry, the binder-plasticizer system had to be modified. Specifically, hydroxyethyl cellulose (HEC) was selected due to its high hydrophilicity, gelling and water retention behavior, for which it is already exploited in the production of dry mix mortars [243] and as rheological tuning agent in the development of DIW inks [244]. Indeed, it has been shown that the HEC in water has the tendency to create a polymer network with high intermolecular water sorption capacity [245]. **Figure 3.7** (a-b) shows the viscosity and shear stress profile of slurry with composition 4 (1 wt% HEC) and its comparison with the ones of slurry with composition 3 (1 wt% PVA). According to the interpolation by the power law model ((3) in §2.3) showed in **Figure 3.7** (a), the ink possesses a flow index of  $n = 0.8 \pm 0.0$  and a consistency factor of  $K = 0.6 \pm 0.0 \text{ Pa s}^n$  ( $R^2=0.99$ ), thus confirming its shear-thinning behavior. Nevertheless, the different binding system provoked a different evolution of the viscosity at increasing shear rates by reducing the slope of the curve – specifically in the LSD-DIW shear rates region – and thus suggesting a more stable behavior of the slurry during the deposition phases. In addition to that, preliminary printing tests using the HEC based slurry evidenced its influence and effect on the drying of the layers. As shown in **Figure 3.8**, no cracks and/or pinholes on the surface are detectable, therefore confirming the initial premises.

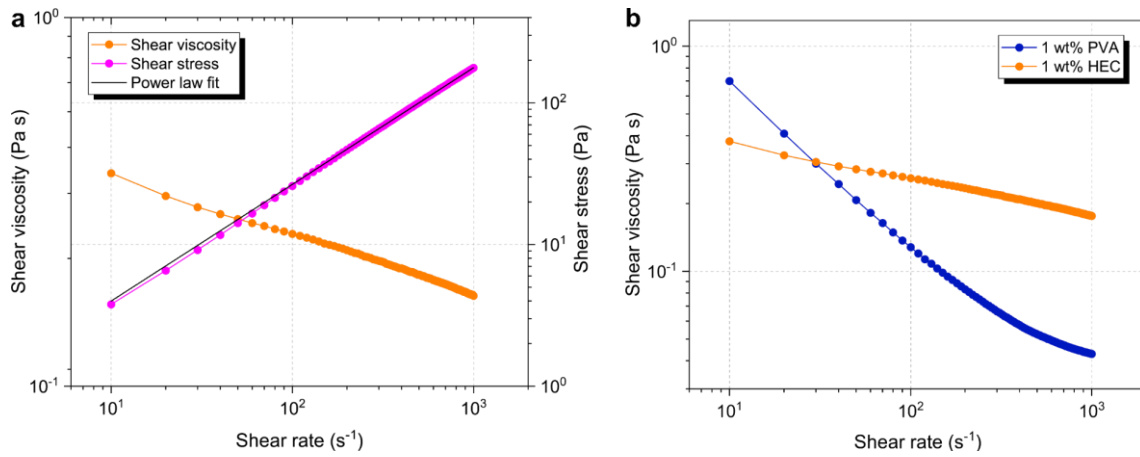


**Figure 3.7.** Viscosity and shear stress profile as a function of shear rate with interpolation by the power law model.



**Figure 3.8.** Top view of a deposited and dried layer of the HEC based slurry.

### 3.3 Inks characterization

As previously described in the Introduction (§ 1.1.1), the fine optimization of the ink rheology is fundamental in the design of an ink for DIW. Specifically, it should ensure the shear-thinning behavior of the ceramic paste, thus allowing not only the homogeneous flow of the ink through the nozzle but especially a fast recovery of its solid-like behaviour and its shape retention. Contrary to conventional DIW, however, an ink being deposited during the LSD-DIW process is

not required to rapidly retain its extruded shape. Indeed, a weak elastic behavior of the ink is preferred as it allows for a homogeneous filling of the machined channels, thus assuring to obtain non-obstructed embedded hollow paths after sintering [43]. In this sense, both graphite-based and tungsten-based inks developed in the present work, will be characterized not only in terms of their shear rate dependence of viscosity but especially by analyzing their viscoelastic properties.

### 3.3.1 Graphite ink

Due to the heating of the build plate, the extrusion phase of the LSD-DIW process is performed on a hot substrate; hence, as the filament is being deposited, it is simultaneously dried up. This means that, when a new layer of alumina slurry is being spread on top of the embedded graphite feature, the latter becomes a (different) drying substrate for the slurry. A mismatch between the drying rates of the alumina slurry and of the graphite ink could be detrimental for the process due to the presence of differential absorption/evaporation forces in the upper layer. Indeed, this was the case when a non-aqueous based graphite ink was employed. Such ink consisted in a dispersion of 41 wt% graphite crystalline powder (325 mesh, Alfa Aesar Johnson Matthey Company, USA) in poly-propylene glycol 2000 (PPG2000, Sigma Aldrich, USA) and was previously formulated for the initial assessment of the LSD-DIW process using a porcelain slurry as matrix material [43]. When more challenging features are attempted in the alumina parts, i.e. the connection of two piled channels to form a single one, the alumina layers covering the bottom channel could not be effectively machined: the much slower drying rate of PPG2000 with respect to HEC inhibited the drying of the upper part of the lower channel. As a result, the drilling tool dragged and pushed the alumina down instead of removing it. **Figure 3.9** shows the  $\mu$ -CT image of the sintered section of such a sample, where the residual alumina is clearly visible and prevents the connection of the channels.



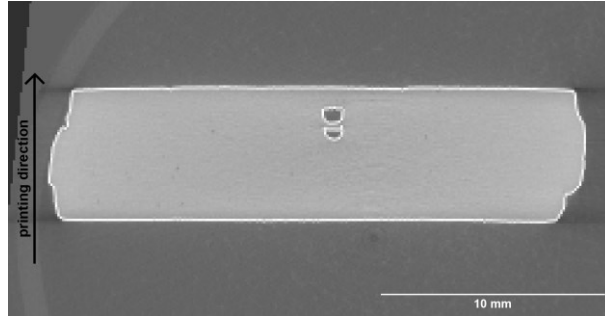


**Figure 3.9.**  $\mu$ -CT of a sintered sample with failed connection of piled channels (to form a single one with dimensions 1.8 x 0.9 mm<sup>2</sup> (h x w)).

For this reason, a new graphite ink was formulated by dispersing 42 wt% of graphite powder in a 1 wt% HEC water-based solution, thus employing the same solvent used in the alumina slurry formulation (§3.2). Alternatively to the power law model [126], the flow behavior of a DIW ink can be also interpreted with the Herschel-Bulkley model [246]:

$$\sigma = \sigma_0 + K \cdot \dot{\gamma}^n \quad (10)$$

Thus referring to a paste possessing an yield stress ( $\sigma_0$ ) and where K and n correspond respectively to the consistency factor and flow behavior index [247]. **Figure 3.10** (a) shows the flow curve obtained for the graphite ink: by interpolation with **(10)** it is possible to obtain the characteristic values of  $\sigma_0 = 0.0 \pm 0.9$  Pa,  $K = 20.9 \pm 0.6$  Pa s<sup>n</sup> and  $n = 0.4 \pm 0.0$  ( $R^2=0.99$ ), thus indicating an ink possessing a nearly zero yield stress and a shear-thinning behavior (i.e.,  $n < 1$ ). **Figure 3.10** (b) displays the storage and loss moduli curves at increasing shear stress applied at a frequency of 1 Hz. The first thing to notice is that the ink possesses a gel-like behavior:  $G'$  is higher than  $G''$  at low shear stresses (i.e., ink at rest) up to a cross-over point (i.e., 2 Pa) after which the ink behaves like a viscous liquid. It is worth noting that such switch in the ink behavior happens at very low shear stresses, ultimately verifying the nearly zero yield stress determined from the flow curve. In addition to that, **Figure 3.10** (b) shows a plateau value of  $G'$  (i.e.,  $2 \cdot 10^2$  Pa) comparable to the one reported for weak gels [248] and thus confirming the behavior previously described. Indeed, as the graphite ink is being deposited, it will have insufficient strength to sustain its shape therefore smoothly flowing and filling into the channels.

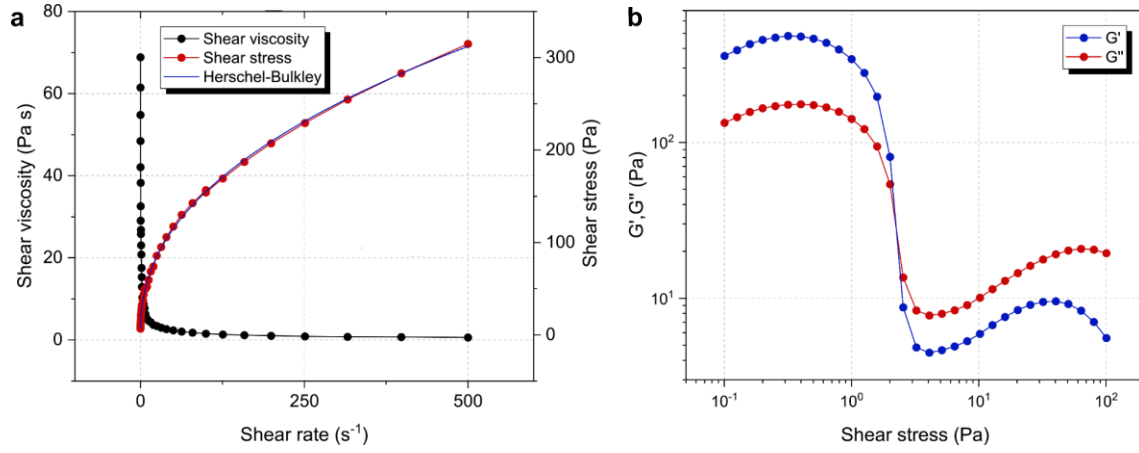


**Figure 3.10.** (a) viscosity and shear stress evolution of the graphite based ink as a function of shear rate with interpolation by the Herschel-Bulkley model; (b) storage and loss moduli as a function of the oscillation stress at 1 Hz.

### 3.3.2 Tungsten ink

Contrary to the graphite-based ink, a commercially available, non-aqueous tungsten based ink (M-20 Tungsten Conductor Paste 300000 cP, Ceronics Inc., USA) was selected as conductive metal phase. **Figure 3.11** (a) displays the flow curve and shear stress profile of the ink. It is worth mentioning that due to the high density of the ink, the shear stress values were obtained as a function of the shear rates by performing an oscillatory test at 1 Hz, reported in **Figure 3.11** (b). Considering the Herschel-Bulkley model (10), and the rheological equation of generalized Newtonian fluids [249]:

$$\sigma = \mu_{eff}(\dot{\gamma}) \cdot \dot{\gamma} \quad (11)$$

(10) can be transformed in order to extrapolate and calculate the shear viscosity, such as:

$$\mu_{eff} = \sigma_0 \cdot \dot{\gamma}^{-1} + K\dot{\gamma}^{n-1} \quad (12)$$

Thus, resulting in the points displayed in **Figure 3.11** (a). Following (10), it is possible to interpolate and obtain typical values of  $\sigma_0 = 9.4 \pm 0.8$  Pa,  $K = 167.5 \pm 1.1$  Pa s<sup>n</sup> and  $n = 0.8 \pm 0.0$  ( $R^2=0.99$ ), thus confirming the shear-thinning behavior of the ink.

As it can be noted, however, the tungsten ink does not display a weak gel behavior; in fact, as reported in **Figure 3.11** (b), the higher value of  $G''$  with respect to  $G'$  for all the shear stress region analyzed suggests that it behaves like a viscous liquid. Indeed, the tungsten paste selected is being conventionally employed for the screen printing of small metal features in buried electrode layers: a liquid-like and shear-thinning ink is required in order to easily extrude the paste out of fine nozzle diameters [250]. Considering the LSD-DIW process, such behavior is both advantageous and detrimental: while favoring the complete filling of the machined channel, as previously described above for the graphite ink, a continuous flowing of the ink is expected even after its deposition. Moreover, it has been demonstrated how the non-aqueous based nature of the tungsten paste is set to create a differential drying mechanism, thus slowing the building speed and drying rate of the alumina in the surroundings of the tungsten feature. Yet, no adjacent tungsten paths were designed in order to avoid what described in **Figure 3.9**; indeed, the present work should be considered as a proof-of-concept for the LSD-DIW/alumina-tungsten combination. Future work on this subject will include the formulation of a water-based ink loaded with tungsten particles. Formulating a stable ink in water is however very challenging, due to the high density and poor oxidation stability of tungsten. At the current stage of development, the issue was rather circumvented by optimizing the design of the tungsten paths to avoid any overlapping, thus preventing what described in **Figure 3.9**.

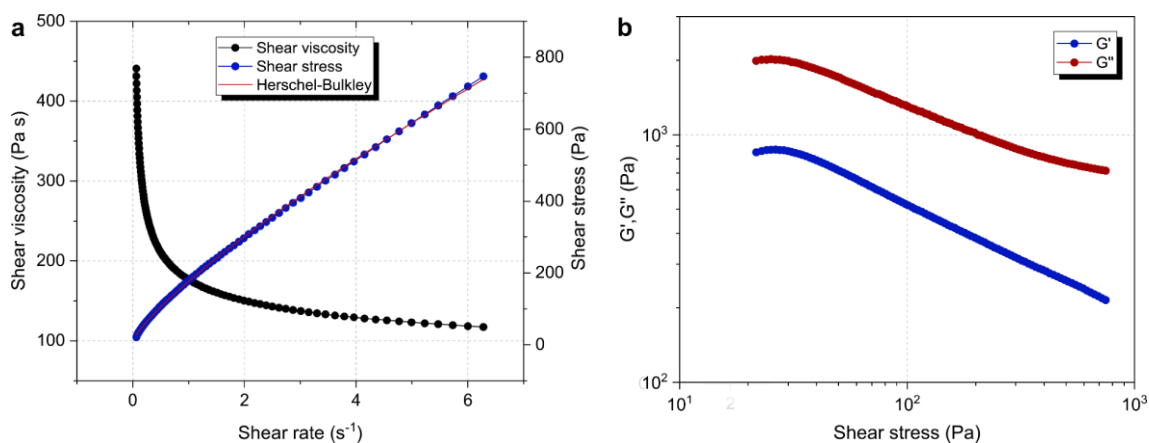


**Figure 3.11.** (a) viscosity and shear stress evolution of the tungsten-based ink as a function of shear rate with interpolation by the Herschel-Bulkley model; (b) storage and loss moduli as a function of the oscillation stress at 1 Hz.

### 3.4 Parts fabrication and characterization

As previously stated, the LSD-DIW process is based on the subsequent repetition of different manufacturing steps (§3.1), each of which relies on the previous one and influences the next. Indeed, the optimization of the binder system of the alumina-based slurry plays a critical role not only for the obtainment of a dense and crack-free matrix, but especially in the following machining step. In this sense, the long-chained structure of HEC helps on further increasing the strength of the dried alumina layers, thus allowing to avoid crack formation upon material removal with the machining tool. Particularly for this work, the machined channels were designed to have dimensions  $0.9 \times 0.9 \text{ mm}^2$  ( $h \times w$ ) in order to accommodate filaments being extruded through a nozzle having diameter of  $0.84 \text{ mm}$ . The drilling procedure was repeated 3 times and consisted in (i) moving the building plate up by  $0.3 \text{ mm}$ , (ii) moving the robot along the designed path at a speed of  $10 \text{ mm s}^{-1}$  while the drilling tool rotates at  $10^4 \text{ rpm}$ . The gradual increase in drilling depth allows to reduce stresses and cracks in the alumina matrix. Moving the platform up (instead of the tool down) allowed to generate and use a single set of files for the robot (i.e., .MBA and .POS, see Appendix B – Grasshopper script for LSD-DIW), thus ultimately decreasing the overall process time of the drilling step.

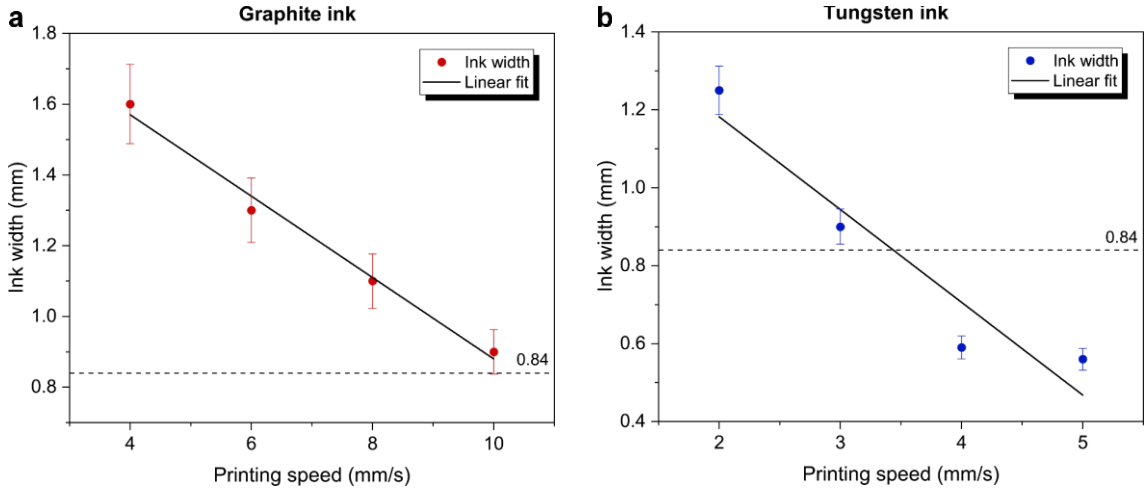


**Figure 3.12.** Ink width as a function of the printing speed at fixed extruder speed (a; graphite ink) and applied pressure (b; tungsten ink).

In order to optimize the filling of the machined channel, it is necessary to control the extrusion width; to do so, the flow rate of the ink out of the nozzle had to match the speed of the extruder

head (i.e., robot). Therefore, preliminary extrusion tests were performed for both the graphite and tungsten inks by varying the printing speed at fixed flow rate. Due to the lower amount of tungsten ink available in the framework of this work with respect to the graphite, the former was extruded through the syringe, while the graphite-based formulation was deposited using the extruder. A pressure of 1.5 bar and an extruder speed of 18 rpm were instead selected for both in order to maintain a stable flow. **Figure 3.12** (a-b) reports the measured extruded width as a function of printing speed. As expected, the lower the printing speed and the higher the over-extrusion tendency of both inks with respect to the theoretically expected width (i.e., 0.84 mm). Hence, the printing speed of the robot was set at  $3.5 \text{ mm s}^{-1}$  and  $10 \text{ mm s}^{-1}$  for the for the syringe and extruder tool, respectively.

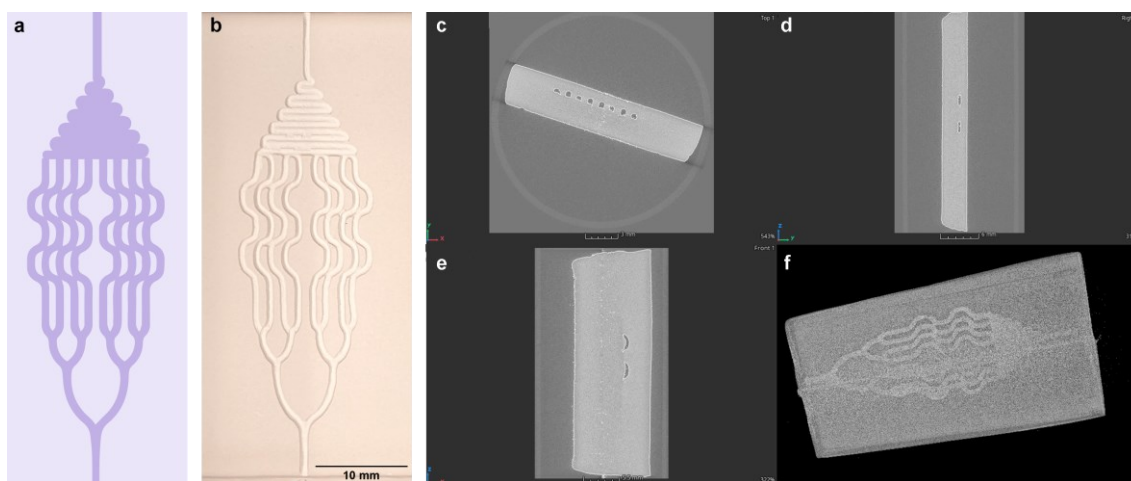


**Figure 3.13.** (a) graphical representation of a micro-reactor design and (b) its result after machining. Results of  $\mu$ -CT scan of the sintered part containing the micro-reactor geometry: (c) perpendicular and (d) longitudinal section; (f) overall projection of the hollow channel.

To demonstrate the technique capabilities, an intricate geometry was designed drawing inspiration from alumina micro-reactor devices previously reported [227]. As shown in **Figure 3.13** (a), such geometry consists of an inlet channel (bottom) separating into multiple branches which later reunite as a single outlet (top). Such a geometry could be useful to distribute a fluid through the ceramic part and to allow for its extensive mixing and homogenization (e.g., for heat exchangers). **Figure 3.13** (b) shows the geometry after the machining step: the measured width of the channel was  $0.87 \pm 0.07 \text{ mm}$  and its height was  $0.86 \pm 0.04 \text{ mm}$ , thus suggesting a good precision of the drilling tool along the building plate. Small discrepancies with the nominal dimensions can still be detected; they are attributed to the repeatability of the robot arm, but

they also result from the way the geometry was constructed. Indeed, in order to reduce the time required for the machining step, the path was designed to follow a continuous polyline; therefore, the tool passes through the same points in order to create the junctures between the branches, and in such junctures a larger channel is obtained.

Once machined, the micro-reactor geometry was filled with graphite ink and covered with other layers of alumina slurry; then, the sample was heat treated following the thermal profile reported in §3.5. **Figure 3.13** (c-f) displays a set of images of the resulting component analyzed via  $\mu$ -CT scanning ( $\mu$ CT 40, Scanco Medical, Switzerland). As it can be noted, channels with round section (area of  $0.19 \pm 0.06 \text{ mm}^2$ ) travel through the sintered part (details in **Figure 3.13** (c-e)): thanks to its gel-like behaviour, the deposited graphite ink was able to withstand the subsequent spreading of the alumina slurry without losing its shape. The slurry flew around the graphite, filling the air gaps between the ink and machined channel and preventing the development of sharp edges; the thorough optimization of the slurry's rheological properties thus allowed to overcome what was reported as one of the main issues of the LSD-DIW technique [43].

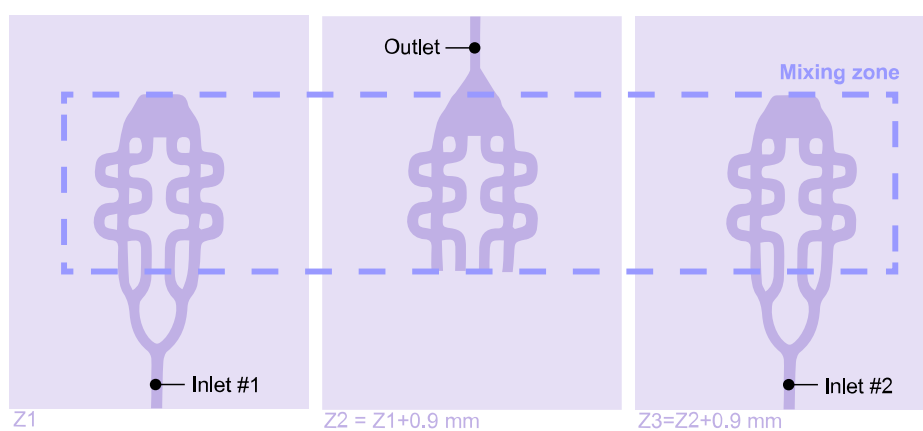


**Figure 3.14.** Schematic of the three channels composing the micro-reactor design.

While the former design can effectively distribute a single fluid through a ceramic component, micro-reactors should allow for the mixing and/or reaction of different fluids. In this sense, a similar geometry was designed, in which two fluids can be injected from two separate inlets piled one on top of the other; in the central (mixing) zone, the two channels are connected, allowing the two fluids to mix (and react) and to exit the component from a single outlet on the other side. The three layers are schematized in **Figure 3.14**. Two steps of the printing process

are reported in **Figure 3.15**: the first image (a) shows the upper inlet after the machining step, which exposes the lower deposited graphite ink (corresponding to the outlet); the second image (b) shows the channel after filling with graphite. In the two images, defects on both the machining and extrusion process can be detected, which can be attributed to the LSD-DIW setup. As mentioned before, the continuous polyline followed by the machining tool results in wider channels at junctions; the same applies to the extruder, as its .MBA file uses the same .POS file of the machining tool, resulting in wider filaments deposited at junctions as highlighted by the black arrows in **Figure 3.15** (b). Moreover, the ink flow out of the nozzle is controlled through a software (Plug & Drive Studio, Nanotec Electronic GmbH & Co. KG, Germany) which is not synchronized with the robot movements; therefore, start/stop commands are manually imparted by the operator and might not exactly match the robot movements.

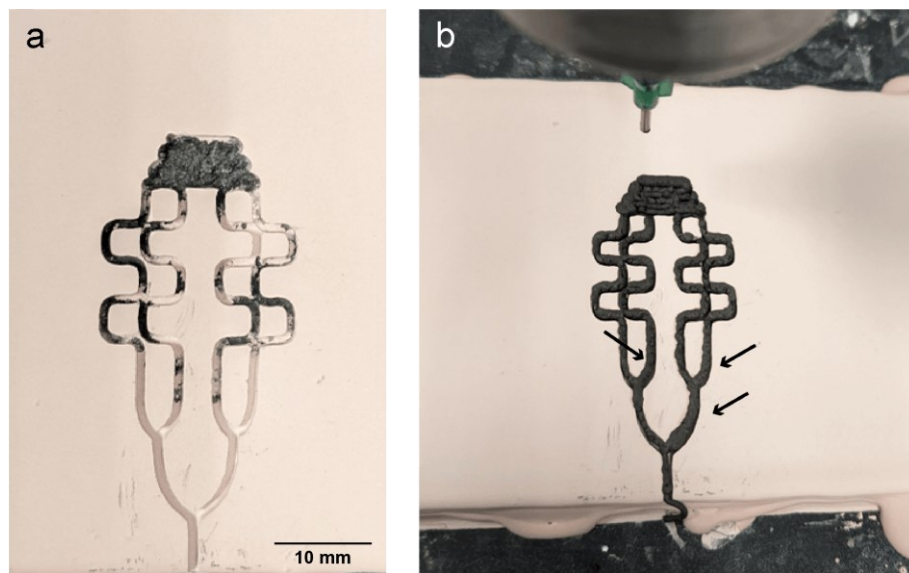


**Figure 3.15.** upper inlet (a) after machining, exposing the outlet layer underneath; (b) after filling with the graphite ink.

In addition to such in-plane defects, it appears from **Figure 3.15** (a) that the machining of the upper inlet did not entirely expose the underlying outlet layer. Mapping the Z coordinate of the drilling tool with respect to the XY plane (**Figure 3.16**) in the printing region (see Appendix B – Grasshopper script for LSD-DIW) shows that small displacements in the XY plane (i.e., 10 mm) correspond to a mismatch in Z in the range of 0.1-0.2 mm: as a result, some parts of the underlying channel are not properly exposed by the drilling step, affecting the connection

between the adjacent channels. Therefore, extra machining steps were performed in order to ensure that hollow, connected channels could be obtained.

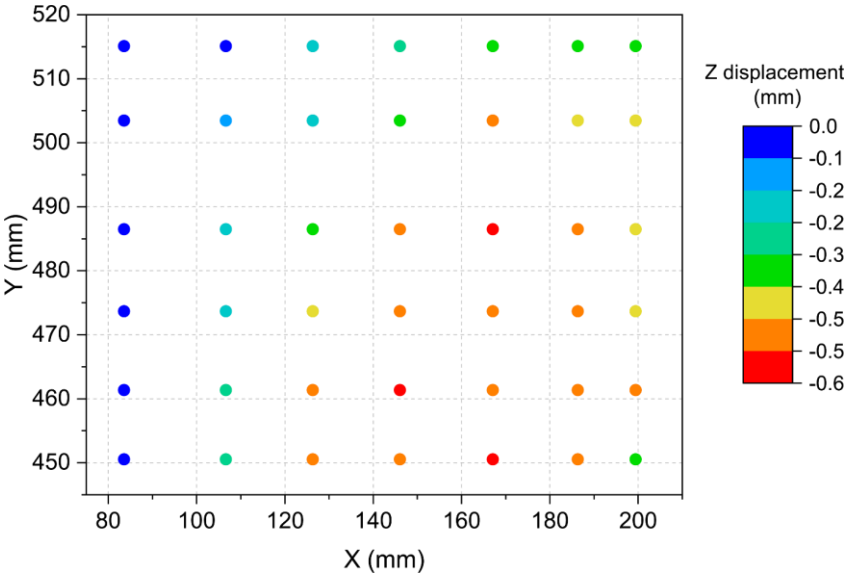


**Figure 3.16.** Z mapping of the drilling tool with respect to the XY plane.

**Figure 3.17** displays the result of the  $\mu$ -CT scan of a sintered part: a hollow, interconnected geometry is obtained throughout all the machined paths; at the two extremities, the sections show the two separate inlets (a) and the single, common outlet (b). The section of the upper inlet is slightly bigger as a result of the extra machining step performed in order to completely expose the outlet layer. However, , at least in the present work, the micro-reactors designs do not possess the fine features usually expected for micro-devices. Nonetheless, since the resolution of the machined path depends on the drilling tool and on the repeatability of the robot arm positioning (i.e., 30  $\mu$ m, according to the manufacturer specifications), narrower channels could be potentially achieved.



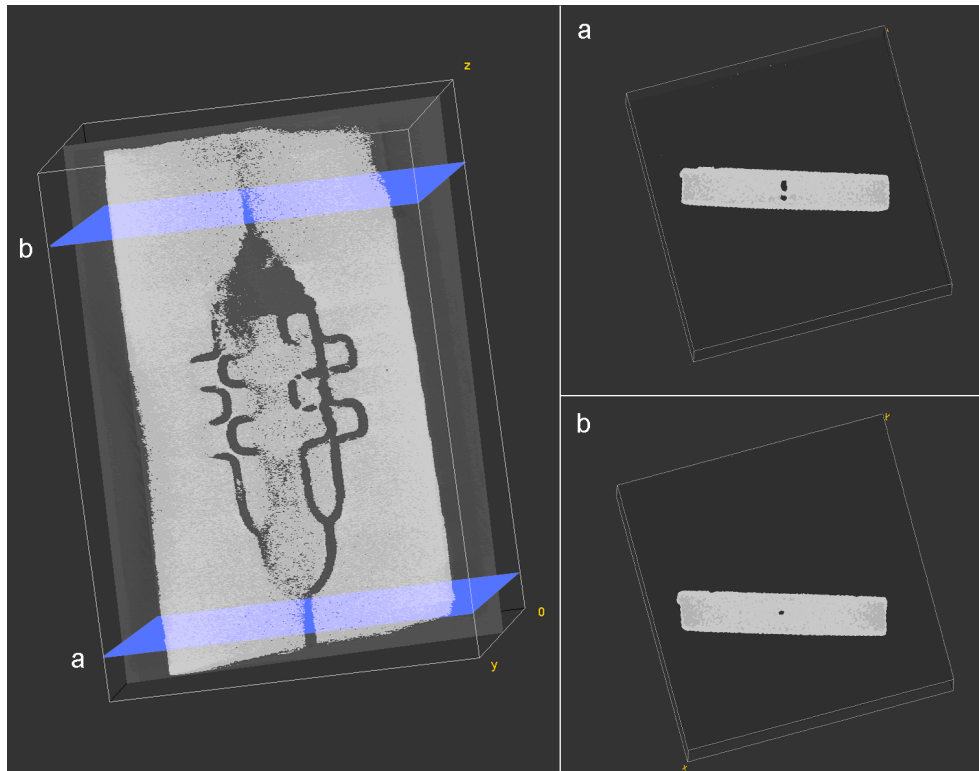


**Figure 3.17.** Volumetric view of a micro-reactor geometry with one inlet and one outlet misaligned in the Z direction and two different sections: inlets (a) and outlet (b).

While the combination of alumina and graphite allows for the production of hollow features (with applications as heat exchangers and micro-reactors), that of alumina and tungsten enables the fabrication of a multi-material component after sintering, suited for high temperature applications. HTCC devices are commonly employed as high-performance heating elements in applications requiring high environmental temperatures coupled with corrosive atmospheres and/or thermally induced stresses. As a proof-of-concept, a simple, circular heating element was designed (**Figure 3.18 (a)**) and fabricated via LSD-DIW (**Figure 3.18 (b-d)**). The curved path was transformed into a list of points (Appendix B – Grasshopper script for LSD-DIW), therefore it appears divided into small segments, visible in **Figure 3.18 (b)**. **Figure 3.18 (c)** shows the deposition of the tungsten paste; due to its liquid-like behavior (§3.3.2), when the tungsten ink is extruded out of the nozzle, it does not flow continuously but rather results in a sequence of droplets. For this reason, it is not able to successfully follow the movements of the printing head and fill the channel precisely, especially at sharp edges and corners (as highlighted by the black arrows in the figure). In addition to this issue, pinholes appear on the subsequent layer of alumina (**Figure 3.18 (d)**); this is attributed to the evaporation of the solvent present in

the tungsten paste formulation and to the differential drying mechanism with respect to the alumina matrix, leading to the generation of bubbles. Nevertheless, the deposition of a continuous, single path of tungsten able to close an external electric circuit (attached at the extremities of the straight vertical lines) could be shown.

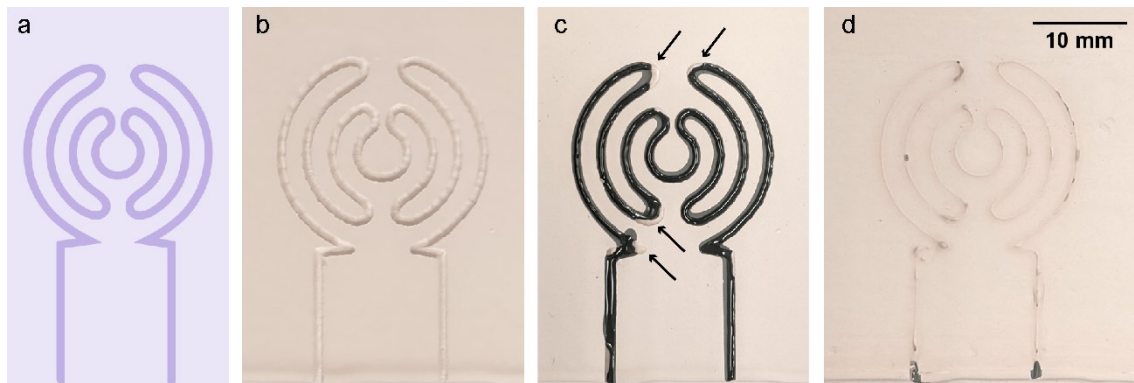


**Figure 3.18.** Graphical representation of the heating element design (a), after being machined (b), after being filled with the tungsten paste (c), and after deposition of a fresh layer of alumina slurry.

### 3.5 Heating treatments

The different multi-material systems required the development of dedicated thermal profiles. A hot stage microscope (Hesse-Instruments, Germany) was employed to identify the optimal sintering temperature and holding time for full densification of the alumina matrix in air. The variation of sectional area of a powder-pressed cylinder was monitored upon heating up to 1410 °C at 10 °C min<sup>-1</sup>. As reported in **Figure 3.19**, the maximum shrinkage of the sample is reached by holding such temperature for about 3 h. In such conditions, the density of sintered samples measured using Archimedes method was  $3.77 \pm 0.01 \text{ g cm}^{-3}$ , corresponding to a relative density of about 99% with respect to the value provided by the powder supplier (i.e.,  $3.82 \text{ g cm}^{-3}$ ). An example of a sample before and after sintering is reported in **Figure 3.20** (a and b, respectively); the overall linear shrinkage was about 13%. Further SEM analysis over the cross-section of a sintered sample (**Figure 3.21**) shows some residual porosity (dark areas) which is typical of this sintered material; however, such porosity was homogeneously distributed and no accumulation of pores or delamination between the layers could be observed.

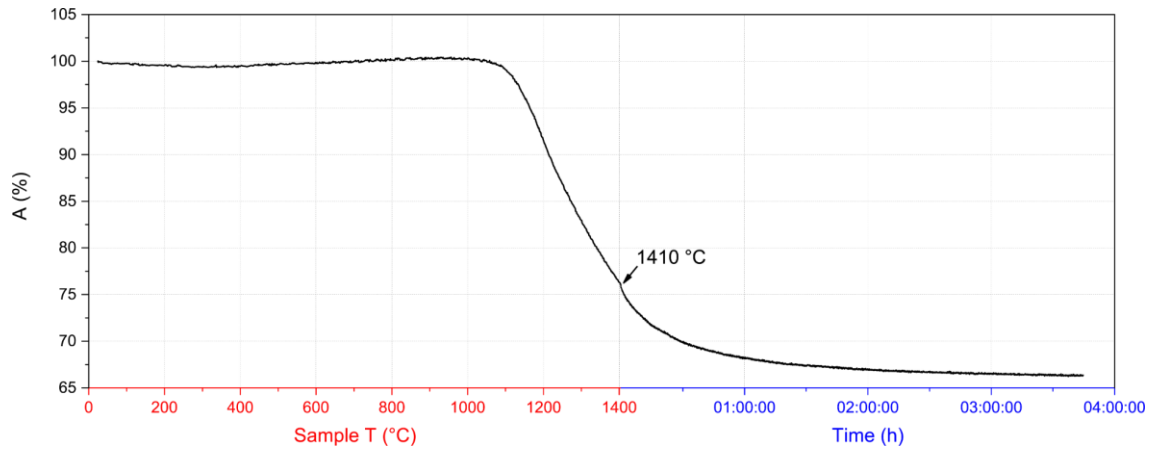


**Figure 3.19.** Relative variation of the cross-sectional area of an alumina sample during heating in a hot stage microscope.

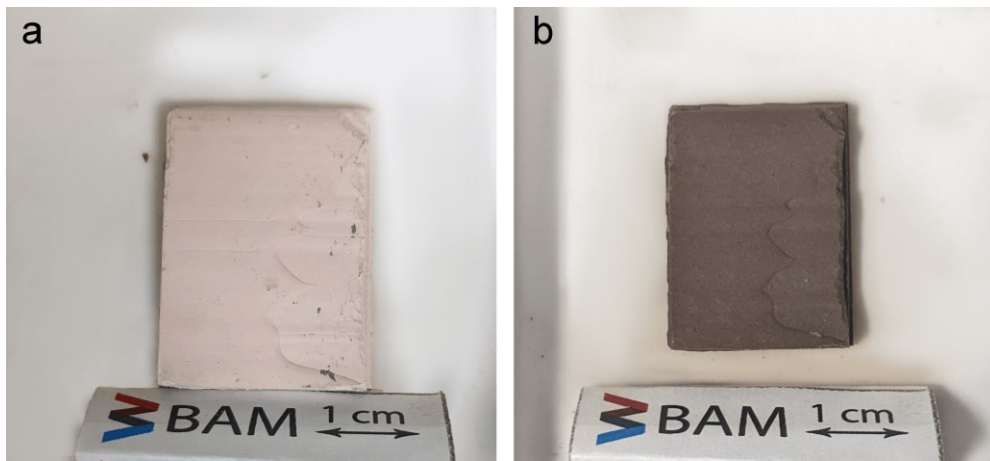


**Figure 3.20.** Bulky alumina component fabricated via LSD-DIW: after printing (a) and after sintering (b).

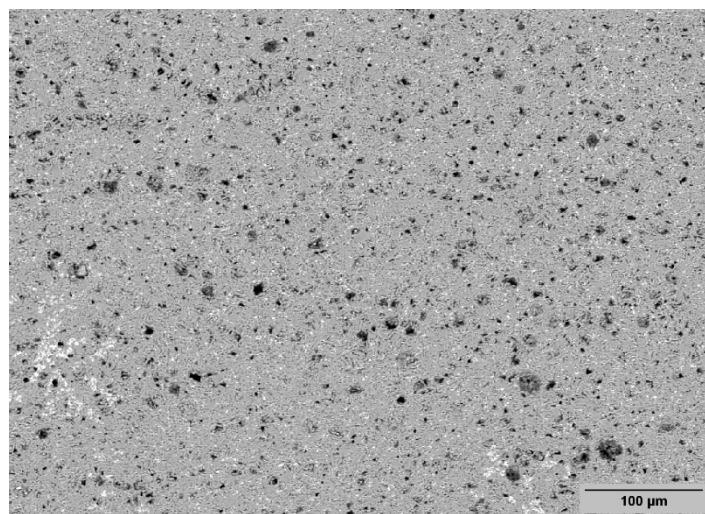


**Figure 3.21.** SEM image of the cross-section of an alumina sintered sample.

The TGA curve of graphite (reported in **Figure 3.22**) served as a basis for the design of the debinding profile for the graphite/alumina samples, with the goal to fully remove the graphite in order to expose the hollow channels without damaging the surrounding matrix. A first heating step up to 300 °C with a heating rate of 2 °C min<sup>-1</sup> was adopted, followed by a second step up to 700 °C with a heating rate of 1 °C min<sup>-1</sup> and a dwelling time of 2 h.

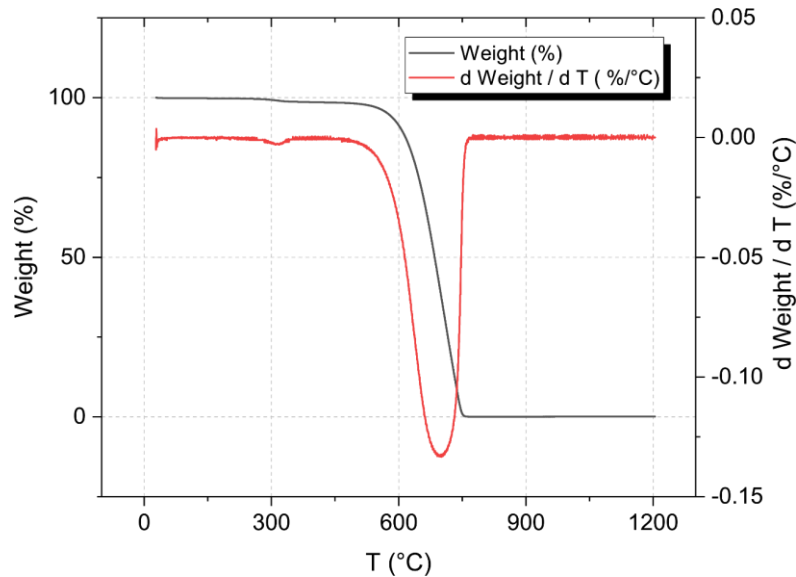


**Figure 3.22.** Thermogravimetric curve (TGA) and 1<sup>st</sup> derivative curve of TGA of the graphite based ink.

In the tungsten/alumina parts, the metallic phase is to be retained in order to obtain a ceramic matrix with embedded conductive paths. The co-firing of multi-material components represents one of the most critical steps of the overall process, due to the different conditions that are required by the singular materials to promote full densification yet avoid crack formation and reactions. Specifically, while alumina can be sintered in air, it would cause the oxidation of the tungsten phase and the formation of a film of WO<sub>3</sub> already at low temperature (i.e., 250 °C) [89], [251]: the oxide layer would cover the embedded metal lines and would expand inside the ceramic matrix, ultimately resulting in cracked and non-conductive parts.

Therefore, tungsten/alumina samples were thermally treated under vacuum following the previous heating profile of alumina: 3 h at 1410 °C with heating a rate of 5 °C/min and a cooling rate of 10 °C/min. **Figure 3.23** shows an example of a tungsten/alumina part in which two disconnected lines draw the profile of a duck. The sample turned black after sintering as the absence of oxygen does not allow for the combustion and efficient removal of the organics.

Indeed, Raynaud et al. [89], recently demonstrated that it is possible to obtain a carbon-free HTCC part by using an Ar/2%H<sub>2</sub> atmosphere with fine tuning of the water partial pressure: a first wet debinding phase followed by a sintering phase in dry conditions allows for the decomposition of the organic phase while avoiding the oxidation of tungsten. While such atmosphere could not be employed for the present work, it represents one of the next steps of investigation for the co-firing of tungsten/alumina components.



**Figure 3.23.** tungsten/alumina part example after printing (left) and after thermal treatment under vacuum (right).

Despite the carbon residues, it should be noted that the tungsten path did not expand nor caused any stresses at the interface with alumina (**Figure 3.24** (a-b)), suggesting that no oxidation took place and that it could be used as electrical conductor. Indeed, while the tungsten path continuity could be verified with a tester, its resistance could not be properly measured due to a too low value with respect to the scale of the device (i.e.,  $> 0.05 \Omega$ ). Nonetheless, as a mere proof-of-concept of the overall system, the conductivity of the tungsten path was validated by connecting the two disjointed tungsten lines within a circuit closed by inserting a LED as the eye of the duck. As shown in **Figure 3.25**, by connecting a power supply of 12 V – 5 A, the LED bulb lights up, confirming the ability of the sintered tungsten path to conduct electricity.

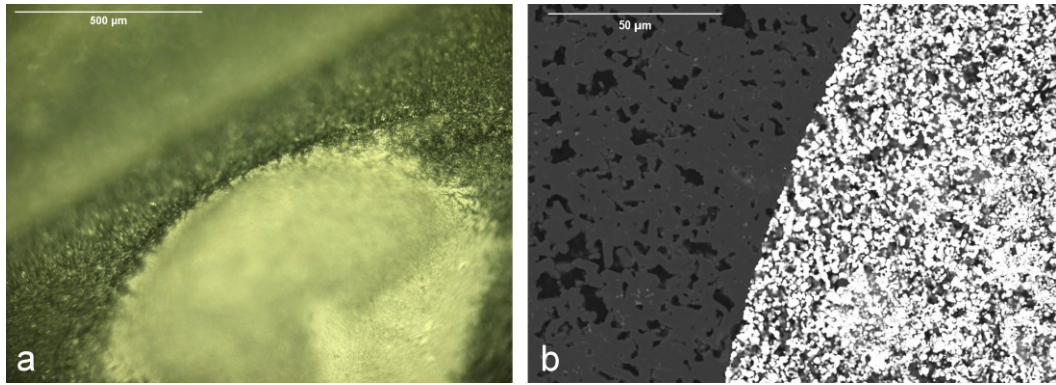


**Figure 3.24.** Optical (a) and SEM (b) image of the interface between alumina (dark, upper left) and tungsten (light, bottom right).

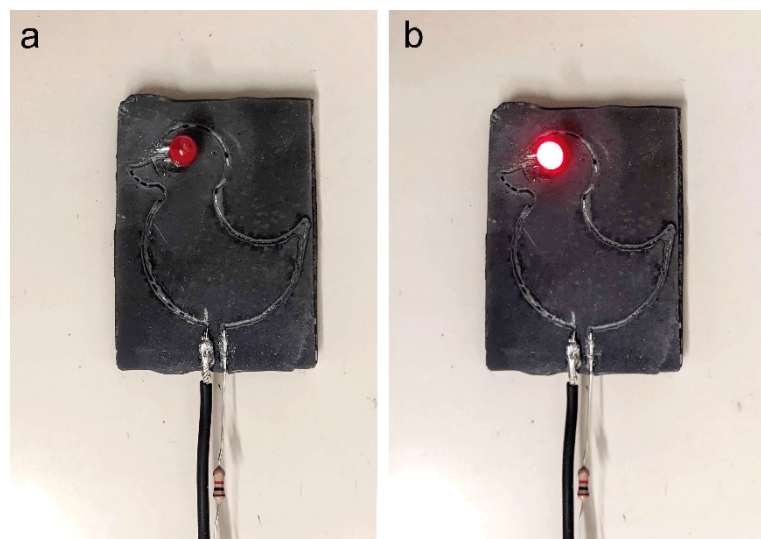


**Figure 3.25.** Test of the connectivity of the tungsten path after sintering in vacuum atmosphere: the LED is off when the circuit is open (a) and lights up when the circuit is closed (b).



## Appendix B – Grasshopper script for LSD-DIW

The calibration and control of the tools was found to be fundamental for the final result of the printing process. Indeed, critical steps of the LSD-DIW technique are represented by the machining of the ceramic layers and the subsequent extrusion of the secondary phase: a mismatch in the position of the drill bit and nozzle tip results in a poorly filled channel and thus, to either obstructed cavities or short circuited metal paths. It should be considered, in fact, that both the machining and dispensing tools are mounted as the end-effector of the robot arm through a flange and placed orthogonally between each other. This means that each of the tool possess different X, Y and Z coordinates, as well as different A, B and C angles in the robot environment.

Before going into details of the script developed, some preliminary considerations must be made. The first regards the printing setup and, in particular, the way that the robot can be programmed. Specifically, the COSIROP software (COSIROP 2.0, Mitsubishi Electric Europe B.V., Germany) is employed to control the robot movements which, as input, requires two different types of files written in the MELFA-BASIC IV language. The first is a .POS file which represents the list of points that define the path through which the robot should move. **Figure B 1** shows an example of .POS file: each line corresponds to a different point (PD n) followed by the XYZ and joint (ABC) jogs coordinates and the sequence R, A, F, O which refers to the robot posture (i.e., Right, Above, Flip, Open). Such position list corresponds to the input of the .MBA file which instead represents the lines of commands that the robot should execute; in the presented work, only linear movements were required, therefore, as shown in **Figure B 1**, the command MVS was used at the beginning of each line to move the robot through P1, P2 and P3 at a speed of  $10 \text{ mm s}^{-1}$  (SPD 10).



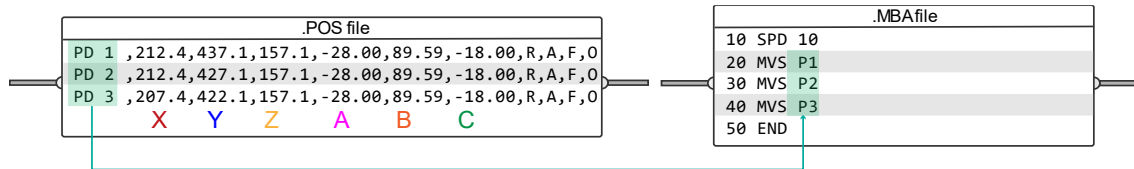


Figure B 1. Examples of .POS and .MBA files.

The conventional method for the writing of such scripts is to directly edit .POS and .MBA files inside of the COSIROP software. Between the two, the .POS file is the most complicated: each position in the points list is created by repeatedly moving the robot in the desired coordinates through the robot T/B remote (Teach Pendant) and then storing them in a blank .POS file. Nevertheless, this means that not only the time required to complete the .POS file directly depends on the number of points, but it especially relies on the sense of space of the operator. Indeed, while a first sketch of the path could be draw and positioned on the building platform, thus guiding into the selection of the positions, such approach should be repeated with all the tools involved in the printing process, each of which possessing different XYZ and ABC coordinates. It is clear that this routine is not sustainable, particularly considering that the main goal of this work is to exploit the advantages of the LSD-DIW technique by fabricating high complex embedded paths composed by a large number of points and by switching between different tools.

Hence, in order to simultaneously manage the geometrical coordinates of the path and tools and create the required .POS and .MBA files, the Grasshopper plugin (2020, Grasshopper3D, Robert McNeel & Associates, USA) of Rhino (2020, Rhinoceros 6, Robert McNeel & Associates, USA), was employed. Such combination of software allows to control and manage the geometric items of the Rhino environment (i.e., polylines, points) through the generation of an algorithm which can contain and combine different types of data, including numbers and texts.

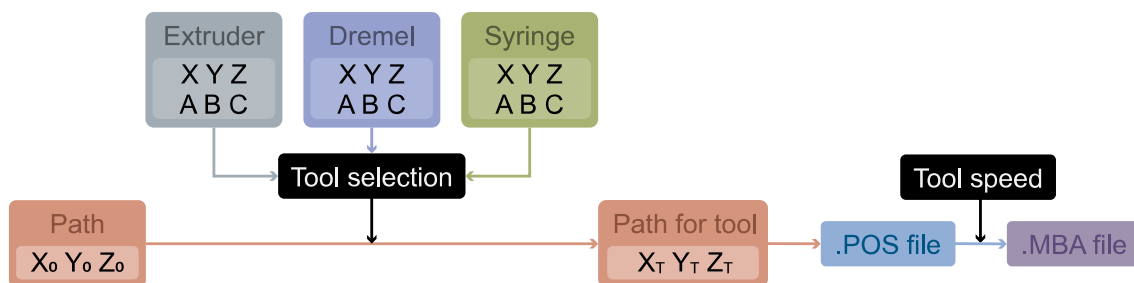
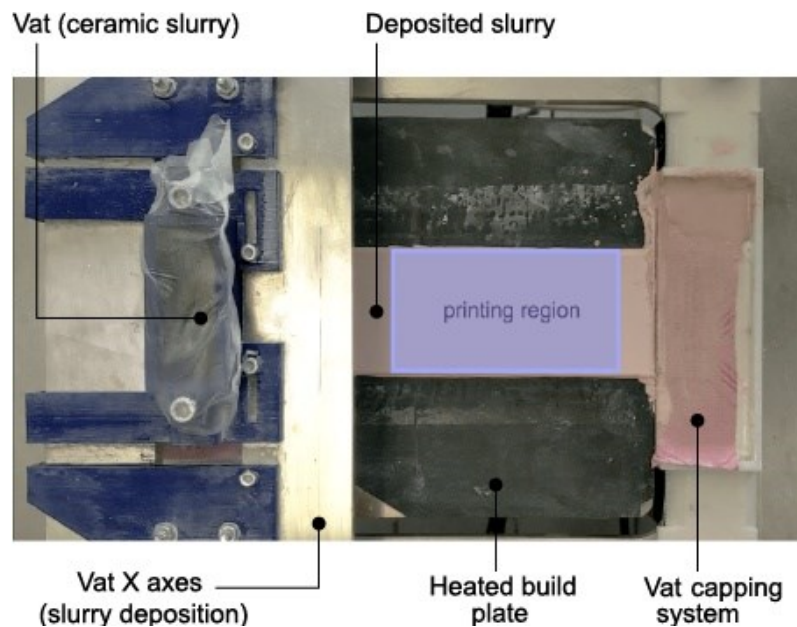


Figure B 2. Schematic of the Grasshopper algorithm.

In this sense, the construction of the algorithm, schematized in **Figure B 2**, can be summarized by the following steps:

1. definition of the working limits of each of the tool (i.e., extruder, syringe and machining drill) with respect to the building platform, thus setting the singular XYZ and ABC ternaries; in this regard, particular attention was posed on the selection of the available printing zone. Specifically, it was necessary to consider not only the encumbrance of the tool head but also the one of the X axes moving the vat along the build plate. In this way, the resulting area was of  $60 \times 120 \text{ mm}^2$  (h x w) and graphically displayed in **Figure B 3**;



**Figure B 3.** Top view of the LSD-DIW setup highlighting the available printing region. Note that the deposited layer is partially covered by the X axis of the vat containing the alumina slurry.

2. selection of the path and translation of its coordinates (XYZ) into the specific tool environment, thus defining the points list; curves designed into the Rhino environment were translated into polylines by means of a tolerance distance of 0.001 mm;
3. construction of the .POS file;
4. selection of the tool speed and construction of the .MBA file.

Once written, .POS and .MBA files can be loaded into the robot to be executed through the COSIROP software. It should be noted that the time required for such a strategy is not

influenced by the number of points and that highly complex geometry can be designed and modified using Rhino, thus decreasing the time required for the design of the channels.



## Appendix C – Alumina water-based compositions

**Table C 1.** List of alumina water-based compositions prepared referring to the final wt% of reagents.

<b>wt%</b>	<b>1</b>	<b>2</b>	<b>3</b>	<b>4</b>
Water	29.2	29.1	28.9	29.5
HTCC powder	68.1	67.9	67.5	68.9
Darvan® 811	0.9	0.9	0.9	1.0
AGITAN® 271	0.2	0.2	0.2	0.2
PEG 200	1.5	1.5	1.4	-
PVA	0.2	0.4	1.0	-
HEC	-	-	-	0.3

**Table C 2.** List of alumina water-based compositions prepared referring to the final vol% of reagents.

<b>vol%</b>	<b>1</b>	<b>2</b>	<b>3</b>	<b>4</b>
Water	60.7	60.6	60.1	61.2
HTCC powder	35.8	35.7	35.4	36.0
Darvan® 811	1.0	1.0	1.0	1.6
AGITAN® 271	0.4	0.4	0.4	0.4
PEG 200	1.9	1.9	1.9	-
PVA	0.2	0.5	1.2	-
HEC	-	-	-	0.8



# Conclusions

The research project focused on the optimization of two different hybrid AM technologies with the aim of further assessing their limits and capabilities.

A spatial UV-assisted DIW technology, derived from the combination of DIW and DLP, was employed for the fabrication of ceramic-based components from UV-curable solutions. The custom set-up was designed to achieve high freedom of movement as well as focusing UV light with sufficient intensity and precision to promote rapid curing of the inks. Silica and silicon nitride-based suspensions were formulated and optimized to obtain highly loaded yet printable inks.

The rheological behavior and the reactivity of the silica containing ink were controlled by tailoring the particle-liquid interactions with an appropriate blend of acrylates as well as with the addition of a silicon alkoxide. The latter also represents an additional silica source contributing to the final ceramic yield, allowing for faster debinding and sintering treatments despite the low particle loading of the ink. The final components are in good agreement with the intended shape provided by the CAD model, and show a homogeneous, amorphous microstructure; their high transmittance, density, hardness and refractive index are all indicative of a dense silica glass. Cerium doped components were fabricated by the introduction of a nitrate precursor and the modification of the ink formulation. Transparent multicomponent glasses with photoluminescence properties were ultimately obtained thanks to the modification of the heating profile.

Regarding the silicon nitride ink, increased dispersion of the particles was reached by maximizing the packing density of the system. The particle size distribution and shape were found to be critical aspects for the homogeneous and stable flow of the ink out of the nozzle. Hence, three different particles size were selected, and their amounts optimized according to the Bolomey equation, while a silane compound was employed to act as steric agent, thus increasing the reproducibility of the ink. Albeit the high refractive index of silicon nitride makes it hardly printable via vat-photopolymerization techniques, the poor curing depth did not compromise

the fabrication of freeform geometries; this further demonstrated that the UV-DIW technology is able to effectively overcome the light-particle interaction issue. Highly porous lattice-beam geometries with mechanical properties comparable to the ones of porous silicon nitride structures were ultimately obtained.

The spatial capabilities of the hybrid technology were further explored by employing a 6-axis robotic arm as the extrusion head carrier. The additional freedom allowed to overcome the 3-axis limitations of the process by promoting uniform irradiation of the extruded filament. This was enabled by the development of a custom GUI: the print head could be selectively oriented with the truss direction, thus promoting fast curing of the ink and increasing the accuracy of the printed part in comparison with the digital model. A better printing resolution could be achieved using a DLP process. Nevertheless, such technology requires a much longer time to fabricate the same structure (i.e., 45% more), more material to fill the printing vat, and an unavoidable cleaning step in order to remove excess material. In addition, the layer-less approach offered by the robot assisted technology ultimately results in an increase in their strength as well as their energy absorption capabilities. This is despite the creation of enlarged nodes in the lattices fabricated using the hybrid technique and a higher filled ink.

An LSD-DIW technology was instead employed for the fabrication of ceramic-metal components. Alumina, tungsten and graphite were selected respectively as the ceramic matrix, conductive, heating element and sacrificial material for the development of hollow channels. Crack formation arising from the evaporation of the alumina slurry was controlled by using a highly hydrophilic and water-retention agent. Moreover, the development of a custom graphical script was found to be essential in order to increase the complexity of the printable paths. Micro-reactor and heater geometries were fabricated and thermally treated under different atmospheres. Hollow embedded channels were obtained thanks to the removal of the graphite ink in air; debinding and sintering were instead performed under vacuum conditions to avoid oxidation of tungsten, thus not compromising its conductivity properties. Compared with other ceramic-metal components fabricated via AM, this technology allows the introduction of secondary phases within the same printing process chain. Similar integrated systems combining SLA and DIW could in principle produce devices with better surface finish and higher resolution; nonetheless, they would require for much more delicate heating schedules in order to fully



remove the higher amount of organic, i.e., the cured polymer in the matrix, and would be more limited in thickness and size.

Overall, the optimization of the UV-DIW and LSD-DIW technologies demonstrated the high degree of freedom that can be unlocked through the hybridization of multiple AM techniques, not only in terms of design but especially of functionality. Yet, it also highlighted some of their limitations which persist as current challenges and will inform future developments.

Firstly, the UV-DIW technique relies upon the DIW process: its lower production speed and printing resolution – compared to the vat photopolymerizations techniques – represent intrinsic technology drawbacks that cannot be fully overcome. Indeed, while higher printing speed could be reached by further tailoring of the ink reactivity and/or UV light source intensity, higher resolution could be obtained only by employing smaller nozzle diameters, which, on the contrary, are limited by the particles size and by the rheological behavior of the ink. In this sense, another unavoidable aspect associated to the UV-DIW technique is that it still requires for the formulation of shear-thinning inks, thus entailing the additional tuning of the particles surface properties with respect to the photocurable resin mixture. Furthermore, the absorption phenomena of dark or colored particles cannot be completely avoided: appropriate tuning of the UV light source intensity is required to preserve the freeform capabilities of the system.

Nonetheless, it was demonstrated how they are not influenced by the high refractive index of ceramic particles. Hence, potential work to be dedicated to the hybrid UV-DIW technology would include the further advancement of the hybrid setup capabilities by fabricating lattice structures using different materials. Taking advantage of the capabilities robot assisted UV-DIW technology, the combination of the mechanical properties of silicon nitride or other advanced materials could be coupled together with the enhanced mechanical response of the structures printed using the 6-axis setup (i.e., stretch-dominated geometry). The use of coaxial nozzles is also of interest, as it would allow to extrude multi-material filaments where only the outer shell needs to be photo-curable; the core could be a sacrificial ink which could be removed upon thermal treatment leaving behind a hollow, tubular structure, or a different material with no photocuring requirements.

In the case of silica glass components, different metal oxides could be added into the formulation in order to specifically tune and enhance the optical properties of the final glass (i.e., higher refractive index, color), thus increase the range of applications (i.e., optics, sensors). The silicon nitride ink, on the other hand, could also benefit from the introduction of preceramic precursors or further modification of the silicon nitride particle surface (i.e., by oxidation) for achieving a higher density of the sintered structures; the generation of cracks in the connection point of the lattices remains an open issue to be solved.

For what concerns the LSD-DIW technology, the process is still in its early stage of development and only proofs-of-concept could be shown, which are still far from the achievable geometrical complexity of channels and conductive tracks. The differential drying rate of the different materials employed and the poor coordination between the robot movements and the dispensing units highly influenced the experiments outcome. In this sense, the scripting editor used to write the robot files could be modified to minimize the Z displacement error and allow for a better connection of adjacent channels; additional commands of the MELFA-BASIC IV language could be employed to fully automate the printing setup. Moreover, the resolution of the machined paths could also be increased by change the tool and nozzle diameters to smaller sizes. Ultimately, the incorporation of the grinding and DIW extrusion tool on the LSD gantry should be considered in order to minimize misplacements. In addition to that, multi-material devices could be fabricated by embedding both sacrificial and conductive inks inside of the alumina matrix: for example, a micro-reactor with a mixing zone which can be heated through an embedded tungsten-made resistor. Nonetheless, further optimization of the heating schedule and atmosphere conditions should be performed in order to prevent the oxidation of tungsten and obtain a dense and multi-functional component.



# References

- [1] ISO/ASTM International, *Standard Terminology for Additive Manufacturing - General Principles - Terminology*. 2016, pp. 1–9.
- [2] V. B. John, “The Shaping of Materials,” in *Introduction to Engineering Materials*, Palgrave Macmillan, London, 1983, pp. 137–177. doi: 10.1007/978-1-349-17190-3\_8.
- [3] B. DeBoer, N. Nguyen, F. Diba, and A. Hosseini, “Additive, subtractive, and formative manufacturing of metal components: a life cycle assessment comparison,” *Int. J. Adv. Manuf. Technol.*, vol. 115, no. 1–2, pp. 413–432, Jul. 2021, doi: 10.1007/S00170-021-07173-5.
- [4] D. D. Camacho *et al.*, “Applications of Additive Manufacturing in the Construction Industry - A Prospective Review,” in *34th International Symposium on Automation and Robotics in Construction*, 2017. doi: 10.22260/ISARC2017/0033.
- [5] I. Gibson, D. Rosen, B. Stucker, and M. Khorasani, *Additive Manufacturing Technologies*. 2021.
- [6] H. Kodama, “Automatic method for fabricating a three-dimensional plastic model with photo-hardening polymer,” *Rev. Sci. Instrum.*, vol. 52, no. 11, p. 1770, Jun. 1998, doi: 10.1063/1.1136492.
- [7] E. C. Hammel, O. L.-R. Ighodaro, and O. I. Okoli, “Processing and properties of advanced porous ceramics: An application based review,” *Ceram. Int.*, vol. 40, no. 10, pp. 15351–15370, 2014, doi: 10.1016/j.ceramint.2014.06.095.
- [8] D. W. Richerson and W. E. Lee, “Modern Ceramic Engineering : Properties, Processing, and Use in Design,” *Mod. Ceram. Eng.*, Apr. 2018, doi: 10.1201/9780429488245.

- [9] P. Karandikar, M. Watkins, A. McCormick, B. Givens, and M. Aghajanian, “Additive Manufacturing (3D printing) of Ceramics: Microstructure, properties, and product examples,” in *Ceramic Engineering and Science Proceedings*, 2018, pp. 175–190. doi: 10.1002/9781119474746.ch17.
- [10] N. Travitzky *et al.*, “Additive Manufacturing of Ceramic-Based Materials,” *Adv. Eng. Mater.*, vol. 16, no. 6, pp. 729–754, Jun. 2014, doi: 10.1002/ADEM.201400097.
- [11] A. Zocca, G. Franchin, P. Colombo, and J. Günster, “Additive Manufacturing,” *Encycl. Mater. Tech. Ceram. Glas.*, vol. 1–3, pp. 203–221, Jan. 2021, doi: 10.1016/B978-0-12-803581-8.12081-8.
- [12] M. A. S. R. Saadi *et al.*, “Direct Ink Writing: A 3D Printing Technology for Diverse Materials,” *Adv. Mater.*, vol. 34, no. 28, p. 2108855, Jul. 2022, doi: 10.1002/ADMA.202108855.
- [13] J. Cesarano, “A review of robocasting technology,” *Mater. Res. Soc. Symp. Proc.*, vol. 542, pp. 133–139, 1998, doi: 10.1557/proc-542-133.
- [14] J. Cesarano, “Robocasting of Ceramics and Composites using Fine Particle Suspensions,” 1999.
- [15] J. A. Lewis, J. E. Smay, J. Stuecker, and J. Cesarano, “Direct Ink Writing of Three-Dimensional Ceramic Structures,” *J. Am. Ceram. Soc.*, vol. 89, no. 12, pp. 3599–3609, 2009, doi: 10.1111/j.1551-2916.2006.01382.x.
- [16] H. Lopez Hernandez, J. W. Souza, E. A. Appel, H. Lopez Hernandez, J. W. Souza, and E. A. Appel, “A Quantitative Description for Designing the Extrudability of Shear-Thinning Physical Hydrogels,” *Macromol. Biosci.*, vol. 21, no. 2, p. 2000295, Feb. 2021, doi: 10.1002/MABI.202000295.
- [17] J. A. Lewis, H. Matsuyama, G. Kirby, S. Morissette, and J. F. Young, “Polyelectrolyte Effects on the Rheological Properties of Concentrated Cement Suspensions,” *J. Am.*

- Ceram. Soc.*, vol. 83, no. 8, pp. 1905–1913, Aug. 2000, doi: 10.1111/J.1151-2916.2000.TB01489.X.
- [18] J. E. Smay, J. Cesarano, and J. A. Lewis, “Colloidal inks for directed assembly of 3-D periodic structures,” *Langmuir*, vol. 18, no. 14, pp. 5429–5437, Jul. 2002, doi: 10.1021/la0257135.
- [19] J. N. Stuecker, J. Cesarano, and D. A. Hirschfeld, “Control of the viscous behavior of highly concentrated mullite suspensions for robocasting,” *J. Mater. Process. Technol.*, vol. 142, no. 2, pp. 318–325, Nov. 2003, doi: 10.1016/S0924-0136(03)00586-7.
- [20] B. H. King, S. L. Morissette, H. Denham, J. Cesarano, and D. Dimos, “Influence of Rheology on Deposition Behavior of Ceramic Pastes in Direct Fabrication Systems,” in *Solid Freeform Fabrication Proceedings*, 1998, pp. 391–398. doi: 10.26153/TSW/623.
- [21] W. Li, A. Ghazanfari, D. McMillen, M. C. Leu, G. E. Hilmas, and J. Watts, “Fabricating ceramic components with water dissolvable support structures by the Ceramic On-Demand Extrusion process,” *CIRP Ann.*, vol. 66, no. 1, pp. 225–228, Jan. 2017, doi: 10.1016/j.cirp.2017.04.129.
- [22] W. Li and M. C. Leu, “Material Extrusion Based Ceramic Additive Manufacturing,” in *Additive Manufacturing Processes*, ASM International, 2020, pp. 97–111. doi: 10.31399/asm.hb.v24.a0006562.
- [23] C. Hinczewski, S. Corbel, and T. Chartier, “Ceramic suspensions suitable for stereolithography,” *J. Eur. Ceram. Soc.*, vol. 18, no. 6, pp. 583–590, Jan. 1998, doi: 10.1016/S0955-2219(97)00186-6.
- [24] J. W. Halloran, “Ceramic Stereolithography: Additive Manufacturing for Ceramics by Photopolymerization,” *Annu. Rev. Mater. Res.*, vol. 46, pp. 19–40, Jul. 2016, doi: 10.1146/ANNUREV-MATSCI-070115-031841.
- [25] T. Chartier, C. Chaput, F. Doreau, and M. Loiseau, “Stereolithography of structural

- complex ceramic parts,” *J. Mater. Sci.*, vol. 37, no. 15, pp. 3141–3147, Aug. 2002, doi: 10.1023/A:1016102210277.
- [26] O. Santoliquido, P. Colombo, and A. Ortona, “Additive Manufacturing of ceramic components by Digital Light Processing: A comparison between the ‘bottom-up’ and the ‘top-down’ approaches,” *J. Eur. Ceram. Soc.*, vol. 39, no. 6, pp. 2140–2148, Jun. 2019, doi: 10.1016/J.JEURCERAMSOC.2019.01.044.
- [27] Y. De Hazan, J. Heinecke, A. Weber, and T. Graule, “High solids loading ceramic colloidal dispersions in UV curable media via comb-polyelectrolyte surfactants,” *J. Colloid Interface Sci.*, vol. 337, no. 1, pp. 66–74, Sep. 2009, doi: 10.1016/j.jcis.2009.05.012.
- [28] M. L. Griffith and J. W. Halloran, “Freeform Fabrication of Ceramics via Stereolithography,” *J. Am. Ceram. Soc.*, vol. 79, no. 10, pp. 2601–2608, 1996, doi: 10.1111/j.1151-2916.1996.tb09022.x.
- [29] G. Taormina, C. Sciancalepore, M. Messori, and F. Bondioli, “3D printing processes for photocurable polymeric materials: technologies, materials, and future trends,” *J. Appl. Biomater. Funct. Mater.*, vol. 16, no. 3, pp. 151–160, Jul. 2018, doi: 10.1177/2280800018764770.
- [30] S. P. Gentry and J. W. Halloran, “Light scattering in absorbing ceramic suspensions: Effect on the width and depth of photopolymerized features,” *J. Eur. Ceram. Soc.*, vol. 35, no. 6, pp. 1895–1904, Jun. 2015, doi: 10.1016/J.JEURCERAMSOC.2014.12.006.
- [31] T. Krause, S. Engler, J. Günster, and J. G. Heinrich, “Process and a device for producing ceramic molds,” U.S. Patent No. 6,827,988, Dec. 07, 2004
- [32] R. E. Mistler, “Tape casting: past, present, potential,” *Am. Ceram. Soc. Bull.*, vol. 77, no. 10, pp. 82–86, 1998.
- [33] F. Doreau, G. Tari, C. Pagnoux, T. Chartier, and J. M. F. F. Ferreira, “Processing of

- aqueous tape-casting of alumina with acrylic emulsion binders,” *J. Eur. Ceram. Soc.*, vol. 18, no. 4, pp. 311–321, Apr. 1998, doi: 10.1016/S0955-2219(97)00144-1.
- [34] I. J. Induja, P. Abhilash, S. Arun, K. P. Surendran, and M. T. Sebastian, “LTCC tapes based on Al<sub>2</sub>O<sub>3</sub>–BBSZ glass with improved thermal conductivity,” *Ceram. Int.*, vol. 41, no. 10, pp. 13572–13581, Dec. 2015, doi: 10.1016/J.CERAMINT.2015.07.152.
- [35] O. Lyckfeldt, E. Lidén, M. Persson, R. Carlsson, and P. Apell, “Progress in the fabrication of Si<sub>3</sub>N<sub>4</sub> turbine rotors by pressure slip casting,” *J. Eur. Ceram. Soc.*, vol. 14, no. 5, pp. 383–395, Jan. 1994, doi: 10.1016/0955-2219(94)90076-0.
- [36] S. Schafföner and C. G. Aneziris, “Pressure slip casting of coarse grain oxide ceramics,” *Ceram. Int.*, vol. 38, no. 1, pp. 417–422, Jan. 2012, doi: 10.1016/j.ceramint.2011.06.064.
- [37] S. Schafföner, L. Freitag, J. Hubáľková, and C. G. Aneziris, “Functional composites based on refractories produced by pressure slip casting,” *J. Eur. Ceram. Soc.*, vol. 36, no. 8, pp. 2109–2117, Jul. 2016, doi: 10.1016/j.jeurceramsoc.2016.02.008.
- [38] J. Günster, S. Engler, and J. G. Heinrich, “Forming of complex shaped ceramic products via layer-wise slurry deposition,” *Bull. Eur. Ceram. Soc.*, vol. 2, no. 4, pp. 217–226, 2011, doi: 10.4416/JCST2011-00038.
- [39] W. Löschau, R. Lenk, S. Scharek, M. Teichgraber, S. Nowotny, and C. Richter, “Prototyping of complex-shaped parts and tools of Si/SiC-ceramics by selective laser sintering,” *Adv. Sci. Technol.*, pp. 567–573, 1999.
- [40] A. Mostafaei *et al.*, “Binder jet 3D printing—Process parameters, materials, properties, modeling, and challenges,” *Prog. Mater. Sci.*, vol. 119, p. 100707, Jun. 2021, doi: 10.1016/J.PMATSCI.2020.100707.
- [41] M. Li, G. Miao, M. Moghadasi, Z. Pei, and C. Ma, “Ceramic binder jetting additive manufacturing: Relationships among powder properties, feed region density, and powder bed density,” *Ceram. Int.*, vol. 47, no. 17, pp. 25147–25151, Sep. 2021, doi:



10.1016/j.ceramint.2021.05.175.

- [42] T. Mühler, C. M. Gomes, J. Heinrich, and J. Günster, “Slurry-Based Additive Manufacturing of Ceramics,” *Int. J. Appl. Ceram. Technol.*, vol. 12, no. 1, pp. 18–25, Jan. 2015, doi: 10.1111/IJAC.12113.
- [43] R. de Melo Bernardino, S. Valentino, G. Franchin, J. Günster, and A. Zocca, “Manufacturing of ceramic components with internal channels by a novel additive/subtractive hybridization process,” *Open Ceram.*, vol. 2, Jul. 2020, doi: 10.1016/j.oceram.2020.100010.
- [44] A. Zocca, P. Colombo, C. M. Gomes, and J. Günster, “Additive Manufacturing of Ceramics: Issues, Potentialities, and Opportunities,” *J. Am. Ceram. Soc.*, vol. 98, no. 7, pp. 1983–2001, Jul. 2015, doi: 10.1111/JACE.13700.
- [45] Z. Chen *et al.*, “3D printing of ceramics: A review,” *J. Eur. Ceram. Soc.*, vol. 39, no. 4, pp. 661–687, Apr. 2019, doi: 10.1016/J.JEURCERAMSOC.2018.11.013.
- [46] A. T. Gaynor and J. K. Guest, “Topology optimization considering overhang constraints: Eliminating sacrificial support material in additive manufacturing through design,” *Struct. Multidiscip. Optim.*, vol. 54, no. 5, pp. 1157–1172, Nov. 2016, doi: 10.1007/S00158-016-1551-X.
- [47] C. S. O’Bryan *et al.*, “Three-dimensional printing with sacrificial materials for soft matter manufacturing,” *MRS Bull.*, vol. 42, no. 8, pp. 571–577, Aug. 2017, doi: 10.1557/MRS.2017.167.
- [48] P. Yin *et al.*, “Engineering of Removing Sacrificial Materials in 3D-Printed Microfluidics,” *Micromachines*, vol. 9, no. 7, Jun. 2018, doi: 10.3390/MI9070327.
- [49] X. Wang *et al.*, “Microstructure and properties evolution of silicon-based ceramic cores fabricated by 3D printing with stair-stepping effect control,” *J. Eur. Ceram. Soc.*, vol. 41, no. 8, pp. 4650–4657, Jul. 2021, doi: 10.1016/J.JEURCERAMSOC.2021.03.036.

- [50] M. R. Karamooz Ravari, M. Kadkhodaei, M. Badrossamay, and R. Rezaei, "Numerical investigation on mechanical properties of cellular lattice structures fabricated by fused deposition modeling," *Int. J. Mech. Sci.*, vol. 88, pp. 154–161, Nov. 2014, doi: 10.1016/J.IJMECSCI.2014.08.009.
- [51] R. L. Hope, R. N. Roth, and P. A. Jacobs, "Adaptive slicing with sloping layer surfaces," *Rapid Prototyp. J.*, vol. 3, no. 3, pp. 89–98, 1997, doi: 10.1108/13552549710185662.
- [52] M. Taufik and P. K. Jain, "Role of build orientation in layered manufacturing: A review," *Int. J. Manuf. Technol. Manag.*, vol. 27, no. 1–3, pp. 47–73, 2013, doi: 10.1504/IJMTM.2013.058637.
- [53] K. S. Bhole and B. Kale, "Techniques to minimise stair-stepping effect in micro-stereolithography process: A Review," *Adv. Mater. Proceeding Technol.*, pp. 3615–3634, 2021, doi: 10.1080/2374068X.2021.1970997.
- [54] J. Jiang, X. Xu, and J. Stringer, "Optimization of process planning for reducing material waste in extrusion based additive manufacturing," *Robot. Comput. Integr. Manuf.*, vol. 59, pp. 317–325, Oct. 2019, doi: 10.1016/j.rcim.2019.05.007.
- [55] B. Lauwers, F. Klocke, A. Klink, A. E. Tekkaya, R. Neugebauer, and D. McIntosh, "Hybrid processes in manufacturing," *CIRP Ann.*, vol. 63, no. 2, pp. 561–583, Jan. 2014, doi: 10.1016/J.CIRP.2014.05.003.
- [56] G. Schuh, J. Kreysa, and S. Orilski, "'hybrid production' road map," *Zeitschrift fuer Wirtschaftlichen Fabrikbetr.*, vol. 104, no. 5, pp. 385–391, May 2009, doi: 10.3139/104.110072.
- [57] L. Li, C. Diver, J. Atkinson, R. Giedl-Wagner, and H. J. Helml, "Sequential laser and EDM micro-drilling for next generation fuel injection nozzle manufacture," *CIRP Ann.*, vol. 55, no. 1, pp. 179–182, 2006, doi: 10.1016/S0007-8506(07)60393-X.
- [58] Y. de Hazan, M. Thänert, M. Trunec, and J. Misak, "Robotic deposition of 3d

- nanocomposite and ceramic fiber architectures via UV curable colloidal inks,” *J. Eur. Ceram. Soc.*, vol. 32, no. 6, pp. 1187–1198, Jun. 2012, doi: 10.1016/J.JEURCERAMSOC.2011.12.007.
- [59] M. Faes, J. Vleugels, F. Vogeler, and E. Ferraris, “Extrusion-based additive manufacturing of ZrO<sub>2</sub> using photoinitiated polymerization,” *CIRP Ann.*, vol. 14, pp. 28–34, Aug. 2016, doi: 10.1016/J.CIRPJ.2016.05.002.
- [60] N. Kretzschmar *et al.*, “Mechanical properties of ultraviolet-assisted paste extrusion and postextrusion ultraviolet-curing of three-dimensional printed biocomposites,” *3D Print. Addit. Manuf.*, vol. 6, no. 3, pp. 127–137, Jun. 2019, doi: 10.1089/3DP.2018.0148.
- [61] L. Wei *et al.*, “Fabrication of SiOC ceramic with cellular structure via UV-Assisted direct ink writing,” *Ceram. Int.*, vol. 46, no. 3, pp. 3637–3643, Feb. 2020, doi: 10.1016/J.CERAMINT.2019.10.083.
- [62] C. M. Clarkson, C. Wyckoff, M. J. S. Parvulescu, L. M. Rueschhoff, and M. B. Dickerson, “UV-assisted direct ink writing of Si<sub>3</sub>N<sub>4</sub>/SiC preceramic polymer suspensions,” *J. Eur. Ceram. Soc.*, vol. 42, no. 8, pp. 3374–3382, Jul. 2022, doi: 10.1016/J.JEURCERAMSOC.2022.03.001.
- [63] A. Mirjan, F. Gramazio, M. Kohler, F. Augugliaro, and R. D’Andrea, “Architectural fabrication of tensile structures with flying machines: BT - Green Design, Materials and Manufacturing Processes,” *Green Des. Mater. Manuf. Process.*, pp. 513–518, 2013, doi: 10.1201/b15002-99.
- [64] S. Liu, Y. Li, and N. Li, “A novel free-hanging 3D printing method for continuous carbon fiber reinforced thermoplastic lattice truss core structures,” *Mater. Des.*, vol. 137, pp. 235–244, Jan. 2018, doi: 10.1016/J.MATDES.2017.10.007.
- [65] L. L. Lebel, B. Aissa, M. A. El Khakani, and D. Therriault, “Ultraviolet-Assisted Direct-Write Fabrication of Carbon Nanotube/Polymer Nanocomposite Microcoils,” *Adv. Mater.*, vol. 22, no. 5, pp. 592–596, Feb. 2010, doi: 10.1002/ADMA.200902192.

- [66] R. D. Farahani, L. L. Lebel, and D. Therriault, "Processing parameters investigation for the fabrication of self-supported and freeform polymeric microstructures using ultraviolet-assisted three-dimensional printing," *J. Micromechanics Microengineering*, vol. 24, no. 5, p. 055020, Apr. 2014, doi: 10.1088/0960-1317/24/5/055020.
- [67] W. Y. Maeng, J. W. Jeon, J. B. Lee, H. Lee, Y. H. Koh, and H. E. Kim, "Photocurable ceramic/monomer feedstocks containing terpene crystals as sublimable porogen for UV curing-assisted 3D plotting," *J. Eur. Ceram. Soc.*, vol. 40, no. 9, pp. 3469–3477, Aug. 2020, doi: 10.1016/J.JEURCERAMSOC.2020.03.047.
- [68] I. Gibson, D. W. Rosen, and B. Stucker, "The Use of Multiple Materials in Additive Manufacturing," *Addit. Manuf. Technol.*, pp. 436–449, 2010, doi: 10.1007/978-1-4419-1120-9\_17.
- [69] M. Vaezi, S. Chianrabutra, B. Mellor, and S. Yang, "Multiple material additive manufacturing – Part 1: a review," *Virtual Phys. Prototyp.*, vol. 8, no. 1, pp. 19–50, 2013, doi: 10.1080/17452759.2013.778175.
- [70] K. L. Sampson, B. Deore, A. Go, and M. A. Nayak, "Multimaterial vat polymerization additive manufacturing," *ACS Appl. Polym. Mater.*, vol. 3, no. 9, pp. 4304–4324, 2021, doi: 10.1021/acsapm.1c00262.
- [71] J. O. Hardin *et al.*, "Microfluidic Printheads for Multimaterial 3D Printing of Viscoelastic Inks," *Adv. Mater.*, vol. 27, no. 21, pp. 3279–3284, Jun. 2015, doi: 10.1002/ADMA.201500222.
- [72] S. Zheng, M. Zlatin, P. R. Selvaganapathy, and M. Brook, "Multiple modulus silicone elastomers using 3D extrusion printing of low viscosity inks," *Addit. Manuf.*, vol. 24, pp. 86–92, 2018, doi: 10.1016/j.addma.2018.09.011.
- [73] D. Kokkinis, F. Bouville, A. R. Studart, D. Kokkinis, F. Bouville, and A. R. Studart, "3D printing of materials with tunable failure via bioinspired mechanical gradients," *Wiley Online Libr.*, vol. 30, no. 19, May 2018, doi: 10.1002/adma.201705808.

- [74] S. L. Sing *et al.*, “Emerging metallic systems for additive manufacturing: In-situ alloying and multi-metal processing in laser powder bed fusion,” *Prog. Mater. Sci.*, vol. 119, p. 100795, 2021, doi: 10.1016/j.pmatsci.2021.100795.
- [75] Y. H. Chueh, X. Zhang, J. C. R. Ke, Q. Li, C. Wei, and L. Li, “Additive manufacturing of hybrid metal/polymer objects via multiple-material laser powder bed fusion,” *Addit. Manuf.*, vol. 36, p. 101465, Dec. 2020, doi: 10.1016/J.ADDMA.2020.101465.
- [76] C. B. Sweeney *et al.*, “Welding of 3D-printed carbon nanotube–polymer composites by locally induced microwave heating,” *Sci. Adv.*, vol. 3, no. 6, Jun. 2017, doi: 10.1126/SCIADV.1700262.
- [77] O. D. Yirmibesoglu *et al.*, “Multi-material direct ink writing of photocurable elastomeric foams,” *Commun. Mater.*, vol. 2, no. 1, pp. 1–14, Jul. 2021, doi: 10.1038/s43246-021-00186-3.
- [78] V. G. Rocha, E. Saiz, I. S. Tirichenko, and E. García-Tuñón, “Direct ink writing advances in multi-material structures for a sustainable future,” *J. Mater. Chem. A*, vol. 8, no. 31, pp. 15646–15657, Aug. 2020, doi: 10.1039/D0TA04181E.
- [79] R. F. Quero, B. M. C. Costa, J. A. F. da Silva, and D. P. de Jesus, “Using multi-material fused deposition modeling (FDM) for one-step 3D printing of microfluidic capillary electrophoresis with integrated electrodes for capacitively coupled contactless conductivity detection,” *Sensors Actuators B Chem.*, vol. 365, p. 131959, Aug. 2022, doi: 10.1016/J.SNB.2022.131959.
- [80] J. Yin, C. Lu, J. Fu, Y. Huang, and Y. Zheng, “Interfacial bonding during multi-material fused deposition modeling (FDM) process due to inter-molecular diffusion,” *Mater. Des.*, vol. 150, pp. 104–112, Jul. 2018, doi: 10.1016/J.MATDES.2018.04.029.
- [81] J. Koopmann, J. Voigt, and T. Niendorf, “Additive Manufacturing of a Steel–Ceramic Multi-Material by Selective Laser Melting,” *Metall. Mater. Trans. B*, vol. 50, no. 2, pp. 1042–1051, Apr. 2019, doi: 10.1007/s11663-019-01523-1.

- [82] D. Han, C. Yang, N. X. Fang, and H. Lee, “Rapid multi-material 3D printing with projection micro-stereolithography using dynamic fluidic control,” *Addit. Manuf.*, vol. 27, pp. 606–615, May 2019, doi: 10.1016/J.ADDMA.2019.03.031.
- [83] J. W. Choi, H. C. Kim, and R. Wicker, “Multi-material stereolithography,” *J. Mater. Process. Technol.*, vol. 211, no. 3, pp. 318–328, Mar. 2011, doi: 10.1016/J.JMATPROTEC.2010.10.003.
- [84] K. A. Mumtaz and N. Hopkinson, “Laser melting functionally graded composition of Waspaloy® and Zirconia powders,” *J. Mater. Sci.*, vol. 42, no. 18, pp. 7647–7656, Sep. 2007, doi: 10.1007/S10853-007-1661-3.
- [85] S. Geier and I. Potestio, “3D-Printing: from multi-material to functionally-graded ceramic,” *Ceram. Appl.*, vol. 8, pp. 32–35, 2020.
- [86] J. A. Lewis, “Voxel8.” <http://www.voxel8.co/>
- [87] J. Li *et al.*, “Hybrid additive manufacturing of 3D electronic systems,” *J. Micromechanics Microengineering*, vol. 26, p. 105005, 2016, doi: 10.1088/0960-1317/26/10/105005.
- [88] P. Wang *et al.*, “Selectively Metalizable Low-Temperature Cofired Ceramic for Three-Dimensional Electronics via Hybrid Additive Manufacturing,” *ACS Appl. Mater. Interfaces*, vol. 14, no. 24, pp. 28060–28073, Jun. 2022, doi: 10.1021/ACSAMI.2C03208.
- [89] J. Raynaud *et al.*, “Hybridization of additive manufacturing processes to build ceramic/metal parts: Example of HTCC,” *J. Eur. Ceram. Soc.*, vol. 41, no. 3, pp. 2023–2033, Mar. 2021, doi: 10.1016/J.JEURCERAMSOC.2020.10.032.
- [90] P. S. Pappas, *Radiation curing: science and technology*. Springer Science & Business Media, 2013. doi: 10.1007/978-1-4899-0712-7.

- [91] J. A. Arceneaux, “Oligomer Solutions for UV Curable Inkjet and 3D Printing Applications,” in *RadTech Proceedings*, 2016.
- [92] J. W. Halloran and M. L. Griffith, “Ultraviolet Curing of Highly Loaded Ceramic Suspensions for Stereolithography of Ceramics,” *Am. Soc. Mech. Eng. Prod. Eng. Div.*, vol. 68, no. 2, pp. 529–534, 1994, doi: 10.15781/T2599ZM4Q.
- [93] J. N. Israelachvili, *Intermolecular and surface forces*. Academic press, 2011. doi: 10.1016/C2009-0-21560-1.
- [94] M. Wozniak, T. Graule, Y. de Hazan, D. Kata, and J. Lis, “Highly loaded UV curable nanosilica dispersions for rapid prototyping applications,” *J. Eur. Ceram. Soc.*, vol. 29, no. 11, pp. 2259–2265, Aug. 2009, doi: 10.1016/j.jeurceramsoc.2009.01.030.
- [95] J. Kizling, B. Kronberg, and J. C. Eriksson, “On the formation and stability of high internal phase O/W emulsions,” *Adv. Colloid Interface Sci.*, vol. 123–126, no. SPEC. ISS., pp. 295–302, Nov. 2006, doi: 10.1016/J.CIS.2006.05.006.
- [96] M. G. Neumann, C. C. Schmitt, G. C. Ferreira, and I. C. Corrêa, “The initiating radical yields and the efficiency of polymerization for various dental photoinitiators excited by different light curing units,” *Dent. Mater.*, vol. 22, no. 6, pp. 576–584, Jun. 2006, doi: 10.1016/J.DENTAL.2005.06.006.
- [97] R. R. Tummala, “Application of Borate Glasses in Electronics,” *Borate Glas.*, pp. 617–622, 1978, doi: 10.1007/978-1-4684-3357-9\_35.
- [98] M.-L. Anne *et al.*, “Chalcogenide Glass Optical Waveguides for Infrared Biosensing,” *Sensors*, vol. 9, no. 9, pp. 7398–7411, 2009, doi: 10.3390/s90907398.
- [99] O. Dymshits, M. Shepilov, and A. Zhilin, “Transparent glass-ceramics for optical applications,” *MRS Bull.*, vol. 42, no. 3, pp. 200–205, Mar. 2017, doi: 10.1557/MRS.2017.29.

- [100] E. Roeder, "Extrusion of glass," *J. Non. Cryst. Solids*, vol. 5, no. 5, pp. 377–388, May 1971, doi: 10.1016/0022-3093(71)90039-1.
- [101] J. Klein *et al.*, "Additive Manufacturing of Optically Transparent Glass," *Mary Ann Liebert, Inc.*, vol. 2, no. 3, pp. 92–105, 2015, doi: 10.1089/3dp.2015.0021.
- [102] A. Bellini, L. Shor, and S. I. Guceri, "New developments in fused deposition modeling of ceramics," *Rapid Prototyp. J.*, vol. 11, no. 4, pp. 214–220, 2005, doi: 10.1108/13552540510612901.
- [103] E. Gal-Or and A. Bracha, "3d printing nozzle calibration inside a heated chamber," Patent W02018163008A1, 2018
- [104] M. Mader *et al.*, "Melt-Extrusion-Based Additive Manufacturing of Transparent Fused Silica Glass," *Adv. Sci.*, vol. 8, no. 23, p. 2103180, Dec. 2021, doi: 10.1002/ADVS.202103180.
- [105] P. Jain, "Feasibility study of manufacturing using rapid prototyping: FDM approach," *Procedia Eng.*, vol. 63, pp. 4–11, 2013, doi: 10.1016/j.proeng.2013.08.275.
- [106] D. T. Nguyen *et al.*, "3D-Printed Transparent Glass," *Adv. Mater.*, vol. 29, no. 26, Jul. 2017, doi: 10.1002/adma.201701181.
- [107] F. Kotz *et al.*, "Three-dimensional printing of transparent fused silica glass," *Nature*, vol. 544, no. 7650, pp. 337–339, Apr. 2017, doi: 10.1038/nature22061.
- [108] D. G. Moore, L. Barbera, K. Masania, and A. R. Studart, "Three-dimensional printing of multicomponent glasses using phase-separating resins," *Nat. Mater.*, vol. 19, no. 2, pp. 212–217, Nov. 2019, doi: 10.1038/s41563-019-0525-y.
- [109] F. Kotz *et al.*, "Two-Photon Polymerization of Nanocomposites for the Fabrication of Transparent Fused Silica Glass Microstructures," *Adv. Mater.*, vol. 33, no. 9, p. 2006341, Mar. 2021, doi: 10.1002/ADMA.202006341.



- [110] T. Doualle, J.-C. André, and L. Gallais, “3D printing of silica glass through a multiphoton polymerization process,” *Opt. Lett.*, vol. 46, no. 2, p. 364, Jan. 2021, doi: 10.1364/ol.414848.
- [111] C. Liu, B. Qian, R. Ni, X. Liu, and J. Qiu, “3D printing of multicolor luminescent glass,” *RSC Adv.*, vol. 8, no. 55, pp. 31564–31567, Sep. 2018, doi: 10.1039/C8RA06706F.
- [112] P. Cai, L. Guo, L. Liu, Q. Zhang, J. Li, and Q. Lue, “Rapid manufacturing of silica glass parts with complex structures through stereolithography and pressureless spark plasma sintering,” *Ceram. Int.*, vol. 48, no. 1, pp. 55–63, Jan. 2022, doi: 10.1016/J.CERAMINT.2021.08.345.
- [113] R. Arita *et al.*, “Rapid three-dimensional structuring of transparent SiO<sub>2</sub> glass using interparticle photo-cross-linkable suspensions,” *Commun. Mater.*, vol. 1, no. 1, Dec. 2020, doi: 10.1038/s43246-020-0029-y.
- [114] X. Wen *et al.*, “3D-printed silica with nanoscale resolution,” *Nat. Mater.*, vol. 20, no. 11, pp. 1506–1511, Oct. 2021, doi: 10.1038/s41563-021-01111-2.
- [115] C. Liu, B. Qian, X. Liu, L. Tong, and J. Qiu, “Additive manufacturing of silica glass using laser stereolithography with a top-down approach and fast debinding,” *RSC Adv.*, vol. 8, no. 29, pp. 16344–16348, Apr. 2018, doi: 10.1039/C8RA02428F.
- [116] I. Cooperstein, E. Shukrun, O. Press, A. Kamyshny, and S. Magdassi, “Additive Manufacturing of Transparent Silica Glass from Solutions,” *ACS Appl. Mater. Interfaces*, vol. 10, no. 22, pp. 18879–18885, Jun. 2018, doi: 10.1021/ACSAMI.8B03766.
- [117] E. Shukrun, I. Cooperstein, and S. Magdassi, “3D-Printed Organic–Ceramic Complex Hybrid Structures with High Silica Content,” *Adv. Sci.*, vol. 5, no. 8, Aug. 2018, doi: 10.1002/advs.201800061.
- [118] F. Kotz *et al.*, “Glassomer - Processing Fused Silica Glass Like a Polymer,” *Adv. Mater.*,

vol. 30, no. 22, May 2018, doi: 10.1002/ADMA.201707100.

- [119] K. Sasan *et al.*, “Additive Manufacturing of Optical Quality Germania-Silica Glasses,” *ACS Appl. Mater. Interfaces*, vol. 12, no. 5, pp. 6736–6741, Feb. 2020, doi: 10.1021/ACSAMI.9B21136.
- [120] S. Haruehansapong, T. Pulngern, and S. Chucheepsakul, “Effect of Nanosilica Particle Size on the Water Permeability, Abrasion Resistance, Drying Shrinkage, and Repair Work Properties of Cement Mortar Containing Nano-SiO<sub>2</sub>,” *Adv. Mater. Sci. Eng.*, vol. 2017, pp. 1–11, 2017, doi: 10.1155/2017/4213690.
- [121] Q. A. Bhatti, M. K. Baloch, S. Schwarz, and G. Petzold, “Effect of Various Parameters on the Stability of Silica Dispersions,” *J. Solution Chem.*, vol. 43, no. 11, pp. 1916–1928, Nov. 2014, doi: 10.1007/s10953-014-0260-6.
- [122] J. Heiber, F. Clemens, T. Graule, D. Hulsenberg, and D. Hülseberg, “Fabrication of SiO<sub>2</sub> glass fibres by thermoplastic extrusion,” *Glas. Sci. Technol.*, vol. 77, no. 5, pp. 211–216, 2004.
- [123] S. R. Raghavan, H. J. Walls, and S. A. Khan, “Rheology of silica dispersions in organic liquids: New evidence for solvation forces dictated by hydrogen bonding,” *Langmuir*, vol. 16, no. 21, pp. 7920–7930, Oct. 2000, doi: 10.1021/la991548q.
- [124] M. DeLombard-Watts and P. T. Weissman, “Comparison of performance of acrylate and methacrylate aliphatic urethanes,” *RadTech Proc.*, 2004.
- [125] F. J. Rubio-Hernandez, J. H. Sánchez-Toro, N. M. Páez-Flor, F. J. Rubio-Hernandez, J. H. Sanchez-Toro, and N. M. Paez-Flor, “Testing shear thinning/thixotropy and shear thickening/antithixotropy relationships in a fumed silica suspension,” *J. Rheol. (N. Y. N. Y.)*, vol. 64, no. 4, pp. 785–797, May 2020, doi: 10.1122/1.5131852.
- [126] R. P. Chhabra and J. F. Richardson, *Non-Newtonian flow in the process industries : fundamentals and engineering applications*. Butterworth-Heinemann, 1999. doi:

10.1016/B978-0-7506-3770-1.X5000-3.

- [127] N. J. Wagner and J. F. Brady, “Shear thickening in colloidal dispersions,” 2009.
- [128] P. F. Jacobs, “Rapid prototyping & manufacturing : fundamentals of stereolithography,” *Soc. Manuf. Eng. Comput. Autom. Syst. Assoc. SME*, p. 434, 1993.
- [129] T. Chartier, A. Badev, Y. Abouliatim, P. Lebaudy, and L. Lecamp, “Stereolithography process: Influence of the rheology of silica suspensions and of the medium on polymerization kinetics - Cure depth and width,” *J. Eur. Ceram. Soc.*, vol. 32, no. 8, pp. 1625–1634, Jul. 2012, doi: 10.1016/j.jeurcerasoc.2012.01.010.
- [130] S. Jin, E. Kareliussen, and C.-M. Cheng, “Photoinitiator Effect on Depth of Cure in Visible Light Cure Polymerization,” in *RadTech Proceedings*, 2020.
- [131] J. E. Klee, M. Maier, and C. P. Fik, “Applied Photochemistry in Dental Materials: From Beginnings to State of the Art,” *Dye. Chromophores Polym. Sci.*, pp. 123–138, May 2015, doi: 10.1002/9781119006671.CH4.
- [132] R. D. Farahani, M. Dubé, and D. Therriault, “Three-Dimensional Printing of Multifunctional Nanocomposites: Manufacturing Techniques and Applications,” *Adv. Mater.*, vol. 28, no. 28, pp. 5794–5821, Jul. 2016, doi: 10.1002/ADMA.201506215.
- [133] N. Hopkins, R. J. van Vuuren, and H. Brooks, “Additive manufacturing via tube extrusion (AMTE<sub>x</sub>),” *Addit. Manuf.*, vol. 36, Dec. 2020, doi: 10.1016/j.addma.2020.101606.
- [134] G. Li *et al.*, “Fabrication of soluble salt-based support for suspended ceramic structure by layered extrusion forming method,” *Mater. Des.*, vol. 183, p. 108173, Dec. 2019, doi: 10.1016/J.MATDES.2019.108173.
- [135] F. J. Martínez-Vázquez, A. Pajares, and P. Miranda, “A simple graphite-based support material for robocasting of ceramic parts,” *J. Eur. Ceram. Soc.*, vol. 38, no. 4, pp. 2247–

2250, Apr. 2018, doi: 10.1016/j.jeurceramsoc.2017.10.016.

- [136] K. Huang, H. Elsayed, G. Franchin, and P. Colombo, “Embedded direct ink writing of freeform ceramic components,” *Appl. Mater. Today*, vol. 23, Jun. 2021, doi: 10.1016/j.apmt.2021.101005.
- [137] P. Thomas-Vielma, A. Cervera, B. Levenfeld, and A. Várez, “Production of alumina parts by powder injection molding with a binder system based on high density polyethylene,” *J. Eur. Ceram. Soc.*, vol. 28, no. 4, pp. 763–771, Jan. 2008, doi: 10.1016/J.JEURCERAMSOC.2007.08.004.
- [138] Z. Yongheng and G. Zhenan, “The study of removing hydroxyl from silica glass,” *J. Non. Cryst. Solids*, vol. 352, no. 38–39, pp. 4030–4033, Oct. 2006, doi: 10.1016/J.JNONCRY SOL.2006.07.037.
- [139] P. Cai *et al.*, “Effects of slurry mixing methods and solid loading on 3D printed silica glass parts based on DLP stereolithography,” *Ceram. Int.*, vol. 46, no. 10, pp. 16833–16841, Jul. 2020, doi: 10.1016/j.ceramint.2020.03.260.
- [140] F. B. Löffler, E. C. Bucharsky, K. G. Schell, S. Heißler, and M. J. Hoffmann, “Development of silica based organic slurries for stereolithographic printing process,” *J. Eur. Ceram. Soc.*, vol. 40, no. 13, pp. 4556–4561, Oct. 2020, doi: 10.1016/J.JEURCERAMSOC.2020.05.023.
- [141] W. Wan, C. E. Huang, J. Yang, J. Zeng, and T. Qiu, “Effect of sintering temperature on the properties of fused silica ceramics prepared by gelcasting,” *J. Electron. Mater.*, vol. 43, no. 7, pp. 2566–2572, 2014, doi: 10.1007/S11664-014-3112-7.
- [142] A. A. Al-Hasnawi, I. Ali, and D. Al-Hydary, “The Effect of Sintering Temperature and Soaking Time on the Transparency of Silica Glass Prepared by Gel-Casting and Sintering,” *Int. J. Appl. Eng. Res.*, vol. 12, no. 24, pp. 15257–15260, 2017.
- [143] Y. K. Ahn, D. H. Kim, H. S. Lim, and S. J. Lee, “Fabrication of transparent amorphous

- silica by controlling forming and sintering processes with spherical nano-silica powder,” *J. Korean Ceram. Soc.*, pp. 1–9, Oct. 2022, doi: 10.1007/S43207-022-00235-8.
- [144] L. L. Hench and J. K. West, “The Sol-Gel Process,” *Chem. Rev.*, vol. 90, no. 1, pp. 33–72, Jan. 1990, doi: 10.1021/CR00099A003.
- [145] D. Kundu, G. De, B. Karmakar, A. Patra, and D. Ganguli, “Sol-gel preparation of silica glass,” *Bull. Mater. Sci.*, vol. 15, no. 5, pp. 453–457, Aug. 1992, doi: 10.1007/BF02745295.
- [146] B. Gu, D. Ko, S. Ahn, D. Choon Hyun, H. K. Lee, and J. Kim, “Synthesis of high purity silica from low cost water glass via sol–gel process and soxhlet extraction,” *J. Sol-Gel Sci. Technol.*, vol. 82, no. 3, pp. 675–681, Jun. 2017, doi: 10.1007/S10971-017-4366-3.
- [147] N. Shen *et al.*, “Laser smoothing of sub-micron grooves in hydroxyl-rich fused silica,” *Appl. Surf. Sci.*, vol. 256, no. 12, pp. 4031–4037, Apr. 2010, doi: 10.1016/J.APSUSC.2010.01.073.
- [148] G. Hetherington, K. H. Jack, and J. C. Kennedy, “The viscosity of vitreous silica,” *Phys. Chem. Glas.*, vol. 123, no. 5, pp. 130–136, 1970.
- [149] J. Hostaša, F. Picelli, S. Hříbalová, and V. Nečina, “Sintering aids, their role and behaviour in the production of transparent ceramics,” *Open Ceram.*, vol. 7, p. 100137, Sep. 2021, doi: 10.1016/J.OCERAM.2021.100137.
- [150] B. O. Mysen and P. Richet, “Melt and glass structure: basic concepts,” in *Silicate Glasses and Melts - Developments in Geochemistry*, Elsevier Ltd., 2005, pp. 1–544.
- [151] M. Hegger and S. Lenzen, *Baustoff-Atlas*. 2005.
- [152] I. H. Malitson, “Interspecimen Comparison of the Refractive Index of Fused Silica,” *JOSA*, vol. 55, no. 10, pp. 1205–1209, Oct. 1965, doi: 10.1364/JOSA.55.001205.
- [153] L. W. Riker, “The Use of Rare Earths in Glass Compositions,” pp. 81–94, Sep. 1981,

doi: 10.1021/BK-1981-0164.CH004.

- [154] A. Chelouche, T. Touam, M. Tazerout, F. Boudjouan, D. Djouadi, and A. Doghmane, “Low cerium doping investigation on structural and photoluminescence properties of sol-gel ZnO thin films,” *J. Lumin.*, vol. 181, pp. 448–454, Jan. 2017, doi: 10.1016/J.JLUMIN.2016.09.061.
- [155] E. Malchukova and B. Boizot, “Tunable luminescence from Ce-doped aluminoborosilicate glasses,” *J. Rare Earths*, vol. 32, no. 3, pp. 217–220, Mar. 2014, doi: 10.1016/S1002-0721(14)60055-7.
- [156] O. C. S. Neto, T. A. Lodi, J. G. O. Neto, A. S. S. de Camargo, F. Pedrochi, and A. Steimacher, “Tunable Luminescence of Ce<sup>3+</sup>-Doped Calcium Boroaluminate Glasses for Light Emitting Devices,” *J. Electron. Mater.*, vol. 50, no. 4, pp. 2378–2388, Apr. 2021, doi: 10.1007/s11664-020-08730-6.
- [157] Z. Krstic and V. D. Krstic, “Silicon nitride: The engineering material of the future,” vol. 47, no. 2, Jan. 2012, doi: 10.1007/s10853-011-5942-5.
- [158] S. Hampshire, “Silicon nitride ceramics-review of structure, processing and properties,” *J. Achiev. Mater. Manuf. Eng.*, vol. 24, no. 1, pp. 43–50, 2007.
- [159] H. Klemm, “Silicon Nitride for High-Temperature Applications,” *J. Am. Ceram. Soc.*, vol. 93, no. 6, pp. 1501–1522, Jun. 2010, doi: 10.1111/J.1551-2916.2010.03839.X.
- [160] X. Du, S. S. Lee, G. Blugan, and S. J. Ferguson, “Silicon Nitride as a Biomedical Material: An Overview,” *Int. J. Mol. Sci.*, vol. 23, no. 12, Jun. 2022, doi: 10.3390/IJMS23126551.
- [161] W. Wijianto, “Application of Silicon Nitride (Si<sub>3</sub>N<sub>4</sub>) Ceramics in Ball Bearing,” *Media Mesin Maj. Tek. Mesin*, vol. 15, no. 1, Aug. 2016, doi: 10.23917/MESIN.V15I1.2296.
- [162] M. H. Bocanegra-Bernal and B. Matovic, “Dense and near-net-shape fabrication of

- Si<sub>3</sub>N<sub>4</sub> ceramics,” *Mater. Sci. Eng. A*, vol. 500, no. 1–2, pp. 130–149, Jan. 2009, doi: 10.1016/J.MSEA.2008.09.015.
- [163] S. Hampshire and M. J. Pomeroy, “Grain boundary glasses in silicon nitride: A review of chemistry, properties and crystallisation,” *J. Eur. Ceram. Soc.*, vol. 32, no. 9, pp. 1925–1932, Jul. 2012, doi: 10.1016/J.JEURCERAMSOC.2011.12.023.
- [164] A. Qadir, H. R. Ben Zine, P. Pinke, and J. Dusza, “Tribology of Si<sub>3</sub>N<sub>4</sub> containing in-situ grown Si<sub>2</sub>N<sub>2</sub>O processed from oxidized  $\alpha$  - Si<sub>3</sub>N<sub>4</sub> powders,” *Ceram. Int.*, vol. 47, no. 12, pp. 17417–17426, Jun. 2021, doi: 10.1016/J.CERAMINT.2021.03.058.
- [165] Y. Li *et al.*, “Microstructure and thermal conductivity of gas-pressure-sintered Si<sub>3</sub>N<sub>4</sub> ceramic: the effects of Y<sub>2</sub>O<sub>3</sub> additive content,” *J. Eur. Ceram. Soc.*, vol. 41, no. 1, pp. 274–283, Jan. 2021, doi: 10.1016/J.JEURCERAMSOC.2020.08.035.
- [166] E. Bezzel, N. P. Dalskov, and K. A. Nielsen, “Injection molding of silicon nitride,” *Key Eng. Mater.*, vol. 89–91, pp. 689–692, 1994, doi: 10.4028/WWW.SCIENTIFIC.NET/KEM.89-91.689.
- [167] H. C. Liu, S. Lee, S. Kang, C. F. Edwards, and F. B. Prinz, “RP of Si<sub>3</sub>N<sub>4</sub> burner arrays via assembly mould SDM,” *Rapid Prototyp. J.*, vol. 10, no. 4, p. 239, 2004, doi: 10.1108/13552540410551360.
- [168] X. Dong *et al.*, “Additive manufacturing of silicon nitride ceramics: A review of advances and perspectives,” *Int. J. Appl. Ceram. Technol.*, vol. 19, no. 6, pp. 2929–2949, Nov. 2022, doi: 10.1111/IJAC.14162.
- [169] H. Qi *et al.*, “Additive manufacturing of silicon nitride ceramic floatation spheres with excellent mechanical properties,” *Materials (Basel)*, vol. 12, no. 7, p. 2717, Aug. 2019, doi: 10.3390/ma12172717.
- [170] S. Yu *et al.*, “Fabrication of Si<sub>3</sub>N<sub>4</sub>–SiC/SiO<sub>2</sub> composites using 3D printing and infiltration processing,” *Ceram. Int.*, vol. 47, no. 20, pp. 28218–28225, Oct. 2021, doi:

10.1016/J.CERAMINT.2021.06.235.

- [171] S. Rangarajan, G. Qi, N. Venkataraman, A. Safari, and S. C. Danforth, “Powder Processing, Rheology, and Mechanical Properties of Feedstock for Fused Deposition of Si<sub>3</sub>N<sub>4</sub> Ceramics,” *J. Am. Ceram. Soc.*, vol. 83, no. 7, pp. 1663–1669, Jul. 2000, doi: 10.1111/J.1151-2916.2000.TB01446.X.
- [172] H. Jin, D. Jia, Z. Yang, and Y. Zhou, “Direct ink writing of Si<sub>2</sub>N<sub>2</sub>O porous ceramic strengthened by directional β-Si<sub>3</sub>N<sub>4</sub> grains,” *Ceram. Int.*, vol. 46, no. 10, pp. 15709–15713, Jul. 2020, doi: 10.1016/J.CERAMINT.2020.03.077.
- [173] X. X. Li *et al.*, “Rheology and Curability Characterization of Photosensitive Slurries for 3D Printing of Si<sub>3</sub>N<sub>4</sub> Ceramics,” *Appl. Sci.*, vol. 10, no. 18, p. 6438, Sep. 2020, doi: 10.3390/app10186438.
- [174] M. Wang *et al.*, “Polymer-derived silicon nitride ceramics by digital light processing based additive manufacturing,” *J. Am. Ceram. Soc.*, vol. 102, no. 9, pp. 5117–5126, Sep. 2019, doi: 10.1111/JACE.16389.
- [175] Y. Li *et al.*, “Research on the effects of surface modification of ceramic powder on cure performance during digital light processing (DLP),” *Ceram. Int.*, vol. 48, no. 3, pp. 3652–3658, Feb. 2022, doi: 10.1016/J.CERAMINT.2021.10.146.
- [176] Y. Liu *et al.*, “Formation mechanism of stereolithography of Si<sub>3</sub>N<sub>4</sub> slurry using silane coupling agent as modifier and dispersant,” *Ceram. Int.*, vol. 46, no. 10, pp. 14583–14590, Jul. 2020, doi: 10.1016/j.ceramint.2020.02.258.
- [177] M. S. Faria, F. J. Oliveira, C. M. Fernandes, D. Figueiredo, and S. Olhero, “Si<sub>3</sub>N<sub>4</sub> Parts Fabricated by Robocasting: Proof of Concept,” *Mater. Proc.*, vol. 8, no. 1, p. 67, Jun. 2022, doi: 10.3390/MATERPROC2022008067.
- [178] S. Diener *et al.*, “X-ray microtomography investigations on the residual pore structure in silicon nitride bars manufactured by direct ink writing using different printing patterns,”



*Open Ceram.*, vol. 5, p. 100042, Mar. 2021, doi: 10.1016/J.OCERAM.2020.100042.

- [179] Y. Liu *et al.*, “Effects of particle size and color on photocuring performance of Si<sub>3</sub>N<sub>4</sub> ceramic slurry by stereolithography,” *J. Eur. Ceram. Soc.*, vol. 41, no. 4, pp. 2386–2394, Apr. 2021, doi: 10.1016/J.JEURCERAMSOC.2020.11.032.
- [180] F. Wang, S. Zheng, and B. Wang, “Research on the Optimal Combination of Concrete Aggregates Based on Bolomey Equation,” *MATEC Web Conf.*, vol. 238, p. 02009, Nov. 2018, doi: 10.1051/MATECCONF/201823802009.
- [181] G. Ding *et al.*, “Stereolithography-based additive manufacturing of gray-colored SiC ceramic green body,” *J. Am. Ceram. Soc.*, vol. 102, no. 12, pp. 7198–7209, Dec. 2019, doi: 10.1111/JACE.16648.
- [182] W. Zou, P. Yang, L. Lin, Y. Li, and S. Wu, “Improving cure performance of Si<sub>3</sub>N<sub>4</sub> suspension with a high refractive index resin for stereolithography-based additive manufacturing,” *Ceram. Int.*, vol. 48, no. 9, pp. 12569–12577, May 2022, doi: 10.1016/J.CERAMINT.2022.01.124.
- [183] M. Shen *et al.*, “Effects of exposure time and printing angle on the curing characteristics and flexural strength of ceramic samples fabricated via digital light processing,” *Ceram. Int.*, vol. 46, no. 15, pp. 24379–24384, Oct. 2020, doi: 10.1016/J.CERAMINT.2020.06.220.
- [184] X. Li, K. Hu, and Z. Lu, “Effect of light attenuation on polymerization of ceramic suspensions for stereolithography,” *J. Eur. Ceram. Soc.*, vol. 39, no. 7, pp. 2503–2509, Jul. 2019, doi: 10.1016/J.JEURCERAMSOC.2019.01.002.
- [185] T. Chartier *et al.*, “Influence of irradiation parameters on the polymerization of ceramic reactive suspensions for stereolithography,” *J. Eur. Ceram. Soc.*, vol. 37, no. 15, pp. 4431–4436, Dec. 2017, doi: 10.1016/J.JEURCERAMSOC.2017.05.050.
- [186] F. Jiang and D. Drummer, “Curing Kinetic Analysis of Acrylate Photopolymer for

- Additive Manufacturing by Photo-DSC,” *Polymers (Basel)*., vol. 12, p. 1080, 2020, doi: 10.3390/polym12051080.
- [187] L. Del-Mazo-Barbara and M. P. Ginebra, “Rheological characterisation of ceramic inks for 3D direct ink writing: A review,” *J. Eur. Ceram. Soc.*, vol. 41, no. 16, pp. 18–33, Dec. 2021, doi: 10.1016/J.JEURCERAMSOC.2021.08.031.
- [188] C. I. Hammett, R. G. Rinaldi, and F. W. Zok, “Pyramidal lattice structures for high strength and energy absorption,” *J. Appl. Mech. Trans. ASME*, vol. 80, no. 4, Jul. 2013, doi: 10.1115/1.4007865/370762.
- [189] E. Johansson, O. Lidström, J. Johansson, O. Lyckfeldt, E. Adolfsson, and J. Stampfl, “Influence of Resin Composition on the Defect Formation in Alumina Manufactured by Stereolithography,” *Materials (Basel)*., vol. 10, p. 138, 2017, doi: 10.3390/ma10020138.
- [190] C. J. Bae and J. W. Halloran, “Influence of Residual Monomer on Cracking in Ceramics Fabricated by Stereolithography,” *Int. J. Appl. Ceram. Technol.*, vol. 8, no. 6, pp. 1289–1295, Nov. 2011, doi: 10.1111/J.1744-7402.2010.02578.X.
- [191] M. Börjesson, G. Richardson, and G. Westman, “UV radiation of cellulose fibers and acrylic acid modified cellulose fibers for improved stiffness in paper,” *Bio Resources*, vol. 10, no. 2, pp. 3056–3069, 2015, doi: 10.15376/BIORES.10.2.3056-3069.
- [192] M. B. Berger, “The importance and testing of density/porosity/permeability/pore size for refractories,” in *2010 Conference of The Southern African Institute of Mining and Metallurgy Refractories*, 2010, pp. 101–116.
- [193] H. Suematsu, M. Mitomo, T. E. Mitchell, J. J. Petrovic, O. Fukunaga, and N. Ohashi, “The  $\alpha$ - $\beta$  Transformation in Silicon Nitride Single Crystals,” *J. Am. Ceram. Soc.*, vol. 80, no. 3, pp. 615–620, Mar. 1997, doi: 10.1111/J.1151-2916.1997.TB02876.X.
- [194] Y. I. Belyi, V. V. Koleda, V. M. Svistun, O. G. Kochetkova, and L. V. Doroshenko, “Liquid-phase sintering of a silicon nitride-based ceramic,” *Glas. Ceram.*, vol. 48, no. 1,

- pp. 24–26, 1991, doi: 10.1007/bf00677727.
- [195] British Standards, *Advanced technical ceramics : mechanical properties of monolithic ceramics at room temperature. Part 1, Determination of flexural strength*. 2006, p. 24.
- [196] F. J. Griggs, “The Warren Truss,” *Structure*, pp. 44–48, 2015.
- [197] J. C. Zhou and D. F. Wu, “Materials Science and Technology Estimation of Weibull parameters with linear regression method Estimation of Weibull parameters with linear regression method,” 2013, doi: 10.1179/026708309X12459430509175.
- [198] Ö. Keleş, N. P. Barcenas, D. H. Sprys, and K. J. Bowman, “Effect of Porosity on Strength Distribution of Microcrystalline Cellulose,” *AAPS PharmSciTech*, vol. 16, no. 6, pp. 1455–1464, Dec. 2015, doi: 10.1208/S12249-015-0325-X.
- [199] D. C. Larsen, J. W. Adams, L. R. Johnson, A. P. S. Teotia, and L. G. Hill, *Ceramic materials for advanced heat engines : technical and economic evaluation*. Noyes Publications, 1985. doi: 10.1016/0267-3762(86)90018-4.
- [200] J. Mueller, K. H. Matlack, K. Shea, and C. Daraio, “Energy Absorption Properties of Periodic and Stochastic 3D Lattice Materials,” *Adv. Theory Simulations*, vol. 2, no. 10, Oct. 2019, doi: 10.1002/ADTS.201900081.
- [201] Y. Jin, J. Du, Y. He, and G. Fu, “Modeling and process planning for curved layer fused deposition,” *Int. J. Adv. Manuf. Technol.*, vol. 91, no. 1, pp. 273–285, Nov. 2016, doi: 10.1007/S00170-016-9743-5.
- [202] M. Eichenhofer, J. C. H. Wong, and P. Ermanni, “Continuous lattice fabrication of ultra-lightweight composite structures,” *Addit. Manuf.*, vol. 18, pp. 48–57, Dec. 2017, doi: 10.1016/J.ADDMA.2017.08.013.
- [203] I. Ishak and P. Larochelle, “Robot Arm Platform for Additive Manufacturing : 3 D Lattice Structures,” in *30th Florida Conference on Recent Advances in Robotics*, May

2017, pp. 11–12.

- [204] M. L. De Guevara, L. Borunda, J. Ficca, D. Byrne, and R. Krishnamurti, “Robotic free-oriented additive manufacturing technique for thermoplastic lattice and cellular structures,” *24th Int. Conf. Comput. Archit. Des. Res.*, vol. 2, pp. 333–342, 2019, doi: 10.52842/CONF.CAADRIA.2019.2.333.
- [205] Y. Huang, Y. Xue, X. Wang, and F. Han, “Mechanical behavior of three-dimensional pyramidal aluminum lattice materials,” *Mater. Sci. Eng. A*, vol. 696, pp. 520–528, Jun. 2017, doi: 10.1016/J.MSEA.2017.04.053.
- [206] K. M. M. Tam *et al.*, “Fabrication-aware structural optimisation of lattice additive-manufactured with robot-arm,” *Int. J. Rapid Manuf.*, vol. 7, no. 2/3, p. 120, 2018, doi: 10.1504/IJRAPIDM.2018.092908.
- [207] A. De Marzi, G. Giometti, J. Erler, P. Colombo, and G. Franchin, “Hybrid additive manufacturing for the fabrication of freeform transparent silica glass components,” *Addit. Manuf.*, vol. 54, no. March, p. 102727, 2022, doi: 10.1016/j.addma.2022.102727.
- [208] C. Paredes, F. J. Martínez-Vázquez, H. Elsayed, P. Colombo, A. Pajares, and P. Miranda, “Evaluation of direct light processing for the fabrication of bioactive ceramic scaffolds: Effect of pore/strut size on manufacturability and mechanical performance,” *J. Eur. Ceram. Soc.*, vol. 41, no. 1, pp. 892–900, Jan. 2021, doi: 10.1016/J.JEURCERAMSOC.2020.09.002.
- [209] P. Platek, J. Sienkiewicz, J. Janiszewski, and F. Jiang, “Investigations on mechanical properties of lattice structures with different values of relative density made from 316L by selective laser melting (SLM),” *Materials (Basel)*, vol. 13, no. 9, p. 2204, May 2020, doi: 10.3390/ma13092204.
- [210] J. C. Maxwell, “XLV. On reciprocal figures and diagrams of forces,” *London, Edinburgh, Dublin Philos. Mag. J. Sci.*, vol. 27, no. 182, pp. 250–261, Apr. 2009, doi: 10.1080/14786446408643663.

- [211] G. W. Kooistra, V. S. Deshpande, and H. N. G. Wadley, “Compressive behavior of age hardenable tetrahedral lattice truss structures made from aluminium,” *Acta Mater.*, vol. 52, no. 14, pp. 4229–4237, Aug. 2004, doi: 10.1016/J.ACTAMAT.2004.05.039.
- [212] V. V. Vasiliev and A. F. Razin, “Anisogrid composite lattice structures for spacecraft and aircraft applications,” *Compos. Struct.*, vol. 76, no. 1–2, pp. 182–189, Oct. 2006, doi: 10.1016/J.COMPSTRUCT.2006.06.025.
- [213] P. Colombo and M. Scheffler, *Cellular Ceramics*. Weinheim: WILEY-VCH Verlag GmbH & Co. KGaA, 2005. doi: 10.1002/3527606696.
- [214] R. G. Silva, C. S. Estay, G. M. Pavez, J. Z. Viñuela, and M. J. Torres, “Influence of geometric and manufacturing parameters on the compressive behavior of 3d printed polymer lattice structures,” *Materials (Basel)*, vol. 14, no. 6, p. 1462, Mar. 2021, doi: 10.3390/ma14061462.
- [215] K. Wang, “Die Swell of Complex Polymeric Systems,” *Viscoelasticity - From Theory to Biol. Appl.*, Nov. 2012, doi: 10.5772/50137.
- [216] J. Liu, J. Yan, and H. Yu, “Stress-constrained topology optimization for material extrusion polymer additive manufacturing,” *J. Comput. Des. Eng.*, vol. 8, no. 3, pp. 979–993, May 2021, doi: 10.1093/JCDE/QWAB028.
- [217] A. S. Azar, M. Reiersen, E. W. Hovig, M. M’hamdi, S. Diplas, and M. M. Pedersen, “A novel approach for enhancing the fatigue lifetime of the components processed by additive manufacturing technologies,” *Rapid Prototyp. J.*, vol. 27, no. 2, pp. 256–267, Mar. 2021, doi: 10.1108/RPJ-02-2020-0030.
- [218] G. Lubin, *Handbook of composites*. Springer Science & Business Media, 2013.
- [219] S. C. Tjong, “Structural and mechanical properties of polymer nanocomposites,” *Mater. Sci. Eng. R Reports*, vol. 53, no. 3–4, pp. 73–197, Aug. 2006, doi: 10.1016/j.mser.2006.06.001.

- [220] Z. Alomar and F. Concli, “Compressive behavior assessment of a newly developed circular cell-based lattice structure,” *Mater. Des.*, vol. 205, p. 109716, Jul. 2021, doi: 10.1016/J.MATDES.2021.109716.
- [221] O. S. Es-Said, J. Foyos, R. Noorani, M. Mendelson, R. Marloth, and B. A. Pregger, “Effect of Layer Orientation on Mechanical Properties of Rapid Prototyped Samples,” vol. 15, no. 1, pp. 107–122, 2007, doi: 10.1080/10426910008912976.
- [222] S. Yadlapati, “Influence of FDM Build Parameters on Tensile and Compression Behaviors of 3D Printed Polymer Lattice Structures,” Wright State University, 2018.
- [223] W. Liu, H. Song, Z. Wang, J. Wang, and C. Huang, “Improving mechanical performance of fused deposition modeling lattice structures by a snap-fitting method,” *Mater. Des.*, vol. 181, p. 108065, Nov. 2019, doi: 10.1016/J.MATDES.2019.108065.
- [224] M. Bottin and G. Rosati, “Trajectory Optimization of a Redundant Serial Robot Using Cartesian via Points and Kinematic Decoupling,” *Robotics*, vol. 8, no. 4, p. 101, Dec. 2019, doi: 10.3390/ROBOTICS8040101.
- [225] W. Sixel, M. Liu, G. Nellis, and B. Sarlioglu, “Ceramic 3D printed direct winding heat exchangers for improving electric machine thermal management,” *2019 IEEE Energy Convers. Congr. Expo.*, pp. 769–776, Sep. 2019, doi: 10.1109/ECCE.2019.8913234.
- [226] U. Scheithauer, E. Schwarzer, T. Moritz, and A. Michaelis, “Additive Manufacturing of Ceramic Heat Exchanger: Opportunities and Limits of the Lithography-Based Ceramic Manufacturing (LCM),” *J. Mater. Eng. Perform.*, vol. 27, no. 1, pp. 14–20, Jan. 2018, doi: 10.1007/S11665-017-2843-Z.
- [227] R. Knitter, W. Bauer, D. Göhring, and P. Risthaus, “RP process chains for ceramic microcomponents,” *Rapid Prototyp. J.*, vol. 8, no. 2, pp. 76–82, 2002, doi: 10.1108/13552540210420943.
- [228] W. Bauer and R. Knitter, “Development of a rapid prototyping process chain for the

- production of ceramic microcomponents,” *J. Mater. Sci.*, vol. 37, no. 15, pp. 3127–3140, Aug. 2002, doi: 10.1023/A:1016150126206.
- [229] S. K. Ajmera, C. Delattre, M. A. Schmidt, and K. F. Jensen, “Microfabricated cross-flow chemical reactor for catalyst testing,” *Sensors Actuators B Chem.*, vol. 82, no. 2–3, pp. 297–306, Feb. 2002, doi: 10.1016/S0925-4005(01)01012-7.
- [230] G. Behrens and A. H. Heuer, “Microstructural Characterization of Cofired Tungsten-Metallized High-Alumina Electronic Substrates,” *J. Am. Ceram. Soc.*, vol. 75, no. 10, pp. 2815–2824, Oct. 1992, doi: 10.1111/J.1151-2916.1992.TB05510.X.
- [231] E. A. Barringer, B. C. Foster, J. D. Hodge, and R. S. Lind, “Tungsten paste for co-sintering with pure alumina and method for producing same,” Patent WO06/935264, May 30, 1989
- [232] A. Zocca, P. Lima, and J. Günster, “LSD-based 3D printing of alumina ceramics,” *J. Ceram. Sci. Technol.*, vol. 8, no. 1, pp. 141–148, Mar. 2016, doi: 10.4416/JCST2016-00103.
- [233] J. Kiennemann, T. Chartier, C. Pagnoux, J. F. Baumard, M. Huger, and J. M. Laméran, “Drying mechanisms and stress development in aqueous alumina tape casting,” *J. Eur. Ceram. Soc.*, vol. 25, no. 9, pp. 1551–1564, Jun. 2005, doi: 10.1016/J.JEURCERAMSOC.2004.05.028.
- [234] M. Jabbari, R. Bulatova, A. I. Y. Tok, C. R. H. Bahl, E. Mitsoulis, and J. H. Hattel, “Ceramic tape casting: A review of current methods and trends with emphasis on rheological behaviour and flow analysis,” *Mater. Sci. Eng. B*, vol. 212, pp. 39–61, Oct. 2016, doi: 10.1016/J.MSEB.2016.07.011.
- [235] R. Moreno, “The role of slip additives in tape casting technology. II: Binders and plasticizers,” *Am. Ceram. Soc. Bull.*, vol. 71, no. 11, pp. 1647–1657, 1992.
- [236] G. Y. Onoda Jr, “The rheology of organic binder solutions,” in *Ceramic Processing*

- Before Firing*, G. Y. Onoda Jr and L. L. Hench, Eds. New York: Wiley, 1978, pp. 235–251.
- [237] L. Wang, G. Tang, and Z. K. Xu, “Comparison of Water-Based and Solvent-Based Tape Casting for Preparing Multilayer ZnO Varistors,” *J. Am. Ceram. Soc.*, vol. 91, no. 11, pp. 3742–3745, Nov. 2008, doi: 10.1111/J.1551-2916.2008.02677.X.
- [238] A. Kristoffersson, E. Roncari, and C. Galassi, “Comparison of different binders for water-based tape casting of alumina,” *J. Eur. Ceram. Soc.*, vol. 18, no. 14, pp. 2123–2131, Dec. 1998, doi: 10.1016/S0955-2219(98)00165-4.
- [239] M. B. Kirkham, “Structure and Properties of Water,” in *Principles of Soil and Plant Water Relations*, Elsevier, Ed. Academic Press, 2014, pp. 27–40. doi: 10.1016/B978-0-12-420022-7.00003-3.
- [240] T. Mori, T. Yamada, T. Tanaka, A. Katagiri, and J. Tsubaki, “Effects of slurry properties on the crack formation in ceramic green sheets during drying,” *J. Ceram. Soc. Japan*, vol. 114, no. 1334, pp. 823–828, 2006, doi: 10.2109/JCERSJ.114.823.
- [241] Q. Hou and X. Wang, “The effect of PVA foaming characteristics on foam forming,” *Cellulose*, vol. 24, no. 11, pp. 4939–4948, Nov. 2017, doi: 10.1007/S10570-017-1452-1.
- [242] G. Blugan, K. Morawa, S. Koebel, T. Graule, and J. Kuebler, “Development of a tape casting process for making thin layers of Si<sub>3</sub>N<sub>4</sub> and Si<sub>3</sub>N<sub>4</sub> + TiN,” *J. Eur. Ceram. Soc.*, vol. 27, no. 16, pp. 4789–4795, 2007, doi: 10.1016/J.JEURCERAMSOC.2007.02.211.
- [243] D. Bülischen and J. Plank, “Formation Of Colloidal Polymer Associates From Hydroxyethyl Cellulose (HEC) And Their Role To Achieve Fluid Loss Control In Oil Well Cement,” *SPE Int. Symp. Oilf. Chem.*, vol. 1, pp. 429–439, Apr. 2011, doi: 10.2118/141182-MS.
- [244] H. Xie *et al.*, “3D gel printing of alumina ceramics followed by efficient multi-step liquid



- desiccant drying,” *J. Eur. Ceram. Soc.*, vol. 41, no. 13, pp. 6634–6640, Oct. 2021, doi: 10.1016/J.JEURCERAMSOC.2021.05.034.
- [245] D. Bülischen and J. Plank, “Mechanistic study on carboxymethyl hydroxyethyl cellulose as fluid loss control additive in oil well cement,” *J. Appl. Polym. Sci.*, vol. 124, no. 3, pp. 2340–2347, May 2011, doi: 10.1002/app.35278.
- [246] S. D. Holdsworth, “Rheological models used for the prediction of the flow properties of food products: a literature review,” *Food Bioprod. Process. Trans. Inst. Chem. Eng.*, 1993.
- [247] W. H. Herschel and R. Bulkley, “Konsistenzmessungen von Gummi-Benzollösungen,” *Kolloid-Zeitschrift*, vol. 39, no. 4, pp. 291–300, Aug. 1926, doi: 10.1007/BF01432034.
- [248] E. Feilden, E. G. T. Blanca, F. Giuliani, E. Saiz, and L. Vandeperre, “Robocasting of structural ceramic parts with hydrogel inks,” *J. Eur. Ceram. Soc.*, vol. 36, no. 10, pp. 2525–2533, Aug. 2016, doi: 10.1016/J.JEURCERAMSOC.2016.03.001.
- [249] D. Pritchard, B. R. Duffy, and S. K. Wilson, “Shallow flows of generalised Newtonian fluids on an inclined plane,” *J. Eng. Math.*, vol. 94, no. 1, pp. 115–133, Oct. 2015, doi: 10.1007/S10665-014-9725-2.
- [250] R. R. Suresh *et al.*, “Fabrication of screen-printed electrodes: opportunities and challenges,” *J. Mater. Sci.*, vol. 56, no. 15, pp. 8951–9006, Feb. 2021, doi: 10.1007/S10853-020-05499-1.
- [251] A. Warren, A. Nylund, and I. Olefjord, “Oxidation of tungsten and tungsten carbide in dry and humid atmospheres,” *Int. J. Refract. Met. Hard Mater.*, vol. 14, no. 5–6, pp. 345–353, Jan. 1996, doi: 10.1016/S0263-4368(96)00027-3.

## **Publications**

### **Journal papers**

- A. De Marzi, M. Vibrante, M. Bottin, G. Franchin, Development of robot assisted hybrid additive manufacturing technology for the freeform fabrication of lattice structures, *Additive Manufacturing*, Volume 66, 2023, p. 103456, DOI: 10.1016/j.addma.2023.103456
- A. De Marzi, G. Giometti, J. Erler, P. Colombo, G. Franchin, Hybrid additive manufacturing for the fabrication of freeform transparent silica glass components, *Additive Manufacturing*, Volume 54, 2022, p. 102727, DOI: 10.1016/j.addma.2022.102727
- G. Franchin, H. Elsayed, R. Botti, K. Huang, J. Schmidt, G. Giometti, A. Zanini, A. De Marzi, M. D'Agostini, P. Scanferla, Y. Feng, P. Colombo, Additive Manufacturing of Ceramics from Liquid Feedstocks, *Chinese Journal of Mechanical Engineering: Additive Manufacturing Frontiers*, Volume 1, 2022, p. 100012, DOI: 10.1016/j.cjmeam.2022.100012

### **Patents applications**

- P. Colombo, G. Franchin, G. Giometti, J.E.M. Schmidt, A. De Marzi, Production of glass bodies from polymerisable solutions, US Patent App. 17/596,005, 2020

## **Presentations at conferences**

### **Oral presentations**

- Hybrid additive manufacturing for the fabrication of freeform ceramic components, 45th International Conference and Exposition on Advanced Ceramics conference (ICACC 2021), February 8 – 12, 2021
- Hybrid additive manufacturing for the fabrication of freeform glass components, 46th International Conference and Exposition on Advanced Ceramics conference (ICACC 2022), January 23 – 28, 2022
- Hybrid additive manufacturing for the fabrication of freeform glass components, Ceramics in Europe 2022 (ECerS 2022), July 10 – 14, 2022
- Hybrid additive manufacturing for the fabrication of freeform glass components, 2022 Young Ceramists Additive Manufacturing Forum (yCAM 2022), November 9 – 11, 2022

### **Poster presentations**

- Hybrid additive manufacturing technology applied to Si<sub>3</sub>N<sub>4</sub> freeform components fabrication, 2020 Young Ceramists Additive Manufacturing Forum (yCAM 2020), October 28 – 30, 2020
- Hybrid additive manufacturing technology applied to Si<sub>3</sub>N<sub>4</sub> freeform components fabrication, Materials Science and Technology 2020 (MS&T20), November 2 – 6, 2020 – 3<sup>rd</sup> prize at the Material Advantage Graduate Student Poster Competition

## Curriculum Vitae

### Personal data

Surname, Name: De Marzi, Anna

Date, place of Birth: 03/12/1993, Arzignano (VI), Italy

Ph.D. Course: Industrial Engineering

Cycle: XXXV

Curriculum: Materials

ORCID code: 0000-0003-2266-4273

### Educational and research

- [10/2012 – 09/2015] BSc in Materials and Chemical Engineering, University of Padova, Italy
- [10/2015 – 12/2017] MSc in Materials Engineering, University of Padova, Italy
  - [02 – 08/2017] Erasmus+ Program, Universidade de Aveiro, Portugal
- [04/2018 – 09/2019] Research assistant, University of Padova, Italy
- [10/2019 – present] Ph.D. in Industrial Engineering, University of Padova, Italy
  - [10/2021 – 03/2022] Multi-material LSD-DIW technology research work, Division 5.4 (Advanced Multi-materials Processing), Bundesanstalt für Materialforschung und-prüfung (BAM), Berlin, Germany. Supervisor: Dr Andrea Zocca

### Students thesis co-advised

- Rosario Quaranta, MSc: Direct Ink e fotoreticolazione per la realizzazione di componenti in nitruro di silicio, 2021/22
- Martina Belliato, BSc: Direct Ink Writing e fotoreticolazione di componenti porosi in nitruro di silicio per applicazioni biomedicali, 2021/22
- Giovanna Zaramella, MSc: Hybrid UV-direct ink writing of multicomponent glass, 2021/22